

# 基于离子阱平台的全可控量子计算系统

(申请清华大学理学博士学位论文)

培养单位：交叉信息研究院

学    科：物理学

研    生：路  尧

指导教师：金  奇  奂  副  教  授

二〇一九年十二月



# **Fully Controllable Quantum Computing System Based on Trapped-Ion Platform**

Dissertation Submitted to  
**Tsinghua University**  
in partial fulfillment of the requirement  
for the degree of  
**Doctor of Philosophy**  
in  
**Physics**  
by  
**Yao Lu**

Dissertation Supervisor : Associate Professor Kihwan Kim

**December, 2019**



# 关于学位论文使用授权的说明

本人完全了解清华大学有关保留、使用学位论文的规定，即：

清华大学拥有在著作权法规定范围内学位论文的使用权，其中包括：（1）已获学位的研究生必须按学校规定提交学位论文，学校可以采用影印、缩印或其他复制手段保存研究生上交的学位论文；（2）为教学和科研目的，学校可以将公开的学位论文作为资料在图书馆、资料室等场所供校内师生阅读，或在校园网上供校内师生浏览部分内容；（3）根据《中华人民共和国学位条例暂行实施办法》，向国家图书馆报送可以公开的学位论文。

本人保证遵守上述规定。

**（保密的论文在解密后应遵守此规定）**

作者签名： \_\_\_\_\_

导师签名： \_\_\_\_\_

日 期： \_\_\_\_\_

日 期： \_\_\_\_\_



## 摘要

诸多快速发展的量子技术正在引领我们步入所谓的“第二次量子革命”。量子计算机的提出为解决经典计算机无法胜任的问题开辟了全新的可能性，这一设想也有望在不久的将来成为现实。为此，大量研究人员正在所有可能的物理平台进行广泛而深入的研究，并在过去的五年中，发布了多台小型量子计算机模型。

作为最早被提出用于实现量子计算机的候选平台，离子阱目前仍是最有希望实现大规模量子计算的物理平台之一。在量子比特的相干时间、量子操作的保真度和已实现纠缠的规模等方面，离子阱的性能均优于其他大多数平台。但目前研究人员仍在探索用于构建大规模离子阱量子计算机所需的技术。本文中，我们重点研究了几种具有可扩展性的技术方法，并基于离子阱平台实现了一个小型但全可控的量子计算系统。在该系统中，我们利用射频电场囚禁数个镱离子，并将它们编码为量子比特；同时，通过开发激光独立寻址系统，我们实现了对每个量子比特的完全独立控制。因此，我们可以在任意单量子比特或者量子比特对上执行通用门集中的量子操作，而这意味着该系统具有执行任何通用量子计算任务的能力。

作为量子模拟原理的演示，我们提出了一个验证退相干环境下的量子非平衡功关系的方案。对于一个编码在单离子中的二能级系统，我们实验上实现了对其的可控退相干作用。基于此，我们探究了当系统以不同的速度驱动时，退相干作用对系统做功分布的影响。实验结果成功地验证了该开放系统中的量子非平衡功关系，而这也是该理论在孤立量子系统外的首次验证。

此外，我们通过理论计算验证了多量子比特的全局纠缠门的可扩展方案，并在实验上进行了可行性演示。作为对传统通用门集的扩充，该纠缠门可用于简化量子电路并加速其运行。实验中，利用该纠缠门，我们仅用一次全局操作便产生了多达四个量子比特的最大纠缠态。我们还演示了三自旋铁磁伊辛模型的数字化绝热演化算法，进一步展示了全局纠缠门在实践中的优势。

尽管我们仅构建了一个小规模演示系统，但该系统展现了良好的可扩展性。本文中介绍的技术也可作为未来大规模量子计算机的可扩展模块，并推动相关研究方向的进一步发展。

**关键词：**离子阱；量子计算与模拟；多体纠缠

## Abstract

Fast developing quantum technologies are leading us to step into the so-called second quantum revolution. Among these techniques, quantum computers open up the possibility of solving classically intractable problems and are expected to become a reality in the near future. Therefore, intense researches in a wide range are being carried out on various physical platforms, and during the past five years, several small-scale quantum computers are announced.

As the first candidate proposed to work as quantum computers, trapped-ion platforms are still the leading platforms to achieve large-scale quantum computation, and outperform most of the other platforms from the perspective of coherence time, operation fidelity, and entangled size. However, the arts to construct a large-scale trapped-ion quantum computer are still under exploring. In this thesis, we focus on developing several scalable methods and achieving a small-scale, but fully controllable quantum computing system based on the trapped-ion platform. In such a system, we confine several ytterbium ions, served as qubits, by radio-frequency electric fields. Meanwhile, by developing an individual laser addressing system, we realize fully independent control on each ion qubit. Overall, we can execute quantum operations belonging to a universal gate set on any single qubit or qubit pair, indicating the ability to perform any universal computation task.

As proof-of-principle on quantum simulation, we propose to verify the quantum nonequilibrium work relation in a decohering environment. We experimentally engineer a controllable decohering effect on a two-level system encoded in a single ion. The non-trivial influences of decoherence on work distributions are studied when we drive the system at different speeds to do work. Our results reveal the quantum nonequilibrium work relation established in this open system, representing the first demonstration beyond isolated quantum systems.

Moreover, beyond a conventional universal gate set, we theoretically investigate and experimentally implement a scalable scheme for realizing multi-qubit global entangling gates, which can be utilized to simplify quantum circuits and speed up their execution. With such gates, a maximally entangled state with up to four qubits is generated in a single global operation. Furthermore, we demonstrate a digitized adiabatic evolution algorithm for the three-spin ferromagnetic Ising model, showing the advantages of the



global entangling gates in practice.

Although we only built a small-scale demonstration system, it reveals favorable scalability. The techniques introduced in the thesis could serve as the scalable blocks for large-scale quantum computers, motivating further researches in the relevant directions.

**Key Words:** Trapped-ion; Quantum computation and simulation; Multipartite entanglement

## Content

List of Figures .....	VII
List of Tables .....	XI
List of Abbreviations .....	XII
Chapter 1 Introduction.....	1
1.1 Quantum computation .....	1
1.2 Trapped-ion quantum computer .....	2
1.3 Thesis structure .....	3
Chapter 2 Trapped-ion system .....	5
2.1 Classical dynamics of a single trapped ion .....	5
2.1.1 Pseudo-potential .....	5
2.1.2 Approximate solution of Mathieu equation .....	8
2.2 Collective motion of a single ion-chain.....	11
2.3 Experimental setup .....	14
Chapter 3 Qubit encoded with Ytterbium ion and single-qubit operations .....	18
3.1 Single $^{171}\text{Yb}^+$ qubit and its initialization & detection .....	19
3.1.1 Doppler cooling.....	20
3.1.2 Qubit state initialization.....	23
3.1.3 Qubit state detection.....	24
3.1.4 Alignment of lasers.....	28
3.2 Coherent operations on a single qubit .....	29
3.2.1 Microwave induced magnetic dipole transition .....	29
3.2.2 Stimulated Raman transition .....	33
3.3 Timing control in experiment .....	42
Chapter 4 Application: Quantum nonequilibrium work relation in the presence of decoherence.....	44
4.1 Theoretical background.....	44
4.2 Experimental realization.....	47
4.2.1 Model Hamiltonian and experimental sequence .....	47
4.2.2 Engineering decoherence environment .....	51

4.2.3	Adiabatic shortcuts in projective measurement .....	53
4.3	Experimental results .....	54
4.4	Conclusion .....	57
Chapter 5	Quantum control on multiple qubits.....	59
5.1	Two-qubit entangling gate .....	59
5.1.1	State-dependent force.....	60
5.1.2	Unitary evolution operator .....	61
5.1.3	Two-qubit entangling gate in a two-ion chain .....	62
5.1.4	Further discussion .....	66
5.2	Individual laser addressing on five ion qubits .....	67
5.2.1	Brief introduction to multiple qubits control .....	67
5.2.2	Design of the individual addressing system .....	68
5.3	Initialization and readout on multiple qubits .....	73
5.3.1	Multiple qubits initialization .....	74
5.3.2	Spatially resolved detection .....	75
5.4	Robust universal gate set .....	82
5.4.1	Single-qubit rotation.....	82
5.4.2	Two-qubit entangling gate.....	84
Chapter 6	Extension: Global entangling gates on arbitrary ion qubits.....	87
6.1	Entangling multiple ion qubits through multiple motional modes .....	87
6.2	Pulse optimization with phase modulation .....	90
6.2.1	Expressions of constraints under discrete phase modulation .....	90
6.2.2	Pulse Scheme Optimization .....	93
6.3	Experimental results .....	94
6.3.1	Global entangling gates on a three-ion chain.....	95
6.3.2	Global entangling gates on a four-ion chain .....	98
6.4	Algorithm demonstration: digitized adiabatic evolution.....	101
6.5	Discussion.....	104
6.5.1	Comparison of single-mode and multimode approaches .....	104
6.5.2	Conclusion .....	106
Chapter 7	Conclusion and Outlook .....	108
Reference	.....	110
Acknowledgments	.....	119

## Content

---

声 明 .....	120
Appendix A Electric multipole field .....	121
Appendix B System stabilization .....	124
个人简历、在学期间发表的学术论文与研究成果 .....	128

## List of Figures

Figure 2.1 Density plot of a two-dimensional static quadrupole potential and the pseudo-potential obtained from the corresponding oscillating potential. ....	7
Figure 2.2 Classical motion of a single ion in an RF oscillating potential. ....	10
Figure 2.3 Conventional four-rod trap. ....	10
Figure 2.4 Collective motion of a three-ion chain. ....	14
Figure 2.5 Experimental setup in practice. ....	15
Figure 2.6 Structure of blade trap. ....	16
Figure 2.7 Helical resonator with bifilar structure. ....	17
Figure 3.1 Energy structure of $^{171}\text{Yb}^+$ . ....	20
Figure 3.2 Implementation of the Doppler cooling. ....	21
Figure 3.3 Relationship between damping coefficient and values of red-detuning and saturated parameter. ....	22
Figure 3.4 Experimental results of the Doppler spectroscopy. ....	23
Figure 3.5 Implementation of qubit state initialization through optical pumping. ....	24
Figure 3.6 Implementation of qubit state detection. ....	25
Figure 3.7 Imaging system and photon statistics of different qubit states. ....	25
Figure 3.8 Brief schematic diagram of laser alignment. ....	27
Figure 3.9 State evolutions under different detunings. ....	30
Figure 3.10 Generation of microwave magnetic field. ....	31
Figure 3.11 Measurement of qubit coherence time. ....	33
Figure 3.12 $\Lambda$ -type two-photon Raman transition. ....	34
Figure 3.13 Carrier and sideband transitions. ....	36
Figure 3.14 Implementation of sideband cooling. ....	37

Figure 3.15 Rabi oscillation of carrier transition.....	38
Figure 3.16 Raman transition driven by pulsed laser. ....	40
Figure 3.17 Inside alignment of pulsed laser Mira-HP.....	41
Figure 3.18 $^{171}\text{Yb}^+$ ion qubit driven by 375 nm pulsed laser. ....	41
Figure 3.19 Qubit coherence time measured by non-copropagating Raman lasers.....	42
Figure 3.20 Timing control in experiment.....	43
Figure 4.1 Two-level system encoded in $^{171}\text{Yb}^+$ ion and experimental driving protocol.	48
Figure 4.2 Conceptual and actual experimental schematics of TMP protocol. ....	49
Figure 4.3 Density matrices of prepared effective thermal states. ....	50
Figure 4.4 Power spectral density of discrete Gaussian white noise. ....	52
Figure 4.5 Experiment results of decoherence rate $\gamma$ relation with $(\sigma\Omega_0)^2/2R_s$ . ....	53
Figure 4.6 Work distributions measured with different work protocols.....	55
Figure 4.7 Comparison of the exponential average of work for distributions to the exponential of the free energy difference. ....	57
Figure 5.1 State-dependent displacement in phase space.....	63
Figure 5.2 Construct a CNOT gate with a XX gate and several single-qubit gates.....	64
Figure 5.3 Population measurement of prepared entangled state.....	64
Figure 5.4 Correlation measurement and parity oscillation. ....	65
Figure 5.5 Alignment of Raman lasers. ....	69
Figure 5.6 Telescope system to achieve tightly focusing.....	71
Figure 5.7 Focused individual beams imaged on the EMCCD. ....	73
Figure 5.8 Simultaneous sideband cooling of multiple motional modes. ....	74
Figure 5.9 Probability distribution of the number of photons during multi-ion de- tection and their overlap. ....	76
Figure 5.10 Labview interface for detection with the EMCCD. ....	77
Figure 5.11 Probability distribution of the fitted height of the Gaussian distribution. .	78

Figure 5.12 Rabi oscillation of carrier transition on each ion. ....	80
Figure 5.13 Fidelity measurement of the prepared maximally entangled state. ....	80
Figure 5.14 Updated imaging system. ....	81
Figure 5.15 Photons collected by each PMT channel. ....	82
Figure 5.16 Application of the SK1 composite rotations to achieve intensity insensitive single-qubit rotation. ....	84
Figure 5.17 Different geometric configurations to apply sideband transitions. ....	85
Figure 5.18 Experimental realization of the phase-insensitive two-qubit entangling gate. ....	86
Figure 6.1 Efficient construction of a quantum circuit using a global gate. ....	88
Figure 6.2 Experimental setup used for the implementation of the global entangling gate. ....	89
Figure 6.3 Pulse scheme with phase and amplitude modulation. ....	95
Figure 6.4 Visualization of satisfaction of constraints for three-qubit global entangling gate. ....	96
Figure 6.5 Experimental results of the global entangling gates in three ion qubits. ....	97
Figure 6.6 Pulse scheme with phase and amplitude modulation. ....	98
Figure 6.7 Visualization of satisfaction of constraints for four-qubit global entangling gate. ....	99
Figure 6.8 GHZ states prepared by the global entangling gates. ....	100
Figure 6.9 Quantum circuit for digitized adiabatic evolution. ....	103
Figure 6.10 Ground state of the ferromagnetic Ising model. ....	104
Figure 6.11 Comparison of gate durations between single- and multiple-mode approaches. ....	106
Figure A.1 Electric multipole field. ....	121
Figure A.2 Pseudo-potential along the x-direction with $y = 0$ . ....	123
Figure B.1 Active feedback loop for repetition rate stabilization. ....	124

List of Figures

---

Figure B.2 Active feedback loop for trap frequencies stabilization. .... 126

Figure B.3 Active feedback loop for laser power stabilization. .... 126



## List of Tables

Table 5.1 Lenses of telescope system .....	72
Table 6.1 Pulse scheme for the global 3-qubit entangling gate.....	95
Table 6.2 Pulse scheme for the global 4-qubit entangling gate.....	101

## List of Abbreviations

RF	radio-frequency
DC	direct-current
COM	center-of-mass
UHV	ultrahigh vacuum
Yb	ytterbium
UV	ultraviolet
N.A.	numerical aperture
EMCCD	electron-multiplying charge-coupled device
PMT	photomultiplier tube
SHG	second-harmonic generation
AOM	acousto-optic modulator
EOM	electro-optic modulator
PBS	polarizing beam splitter
BS	beam splitter
DOE	diffractive optical element
RWA	rotating wave approximation
DDS	direct digital synthesizer
AWG	arbitrary wave generator
CW	continuous wavelength
FPGA	field-programmable gate array
TPM	two-point measurement
CNOT	controlled-NOT
ROI	region of interest
GHZ	Greenberger-Horne-Zeilinger
AQC	adiabatic quantum computation

## Chapter 1 Introduction

### 1.1 Quantum computation

"It from bit"<sup>[1]</sup> or "qubit"<sup>[2]</sup>?

The fast development of modern physics, especially the establishment of quantum physics, impacts people's understanding of reality. Numerous experimental results since the 20th century reveal quantum features of our world. Although well-developed classical computers provide us powerful tools to numerically study a system following the laws of classical physics, tremendous obstacles occur when we want to precisely simulate an extensive quantum one. Due to the feature of quantum superposition, the classical resources required to simulate a quantum system would exponentially expose as the size of the quantum system increases. Therefore, a quantum computer, which "*do exactly the same as nature*"<sup>[3]</sup>, are required.

Quantum computers are believed to be capable of solving classically intractable problems, ranging from factorization of large numbers<sup>[4]</sup> to simulation of quantum many-body systems<sup>[3,5]</sup>. The abstract concepts of quantum simulation and quantum computation were initiated by Paul Benioff during the 1970s<sup>[6]</sup>, and they have been well-known since Richard Feynman gave that famous lecture in 1981<sup>[3]</sup>. As an analog of a bit in classical computers, the minimal unit in quantum computers is known as a quantum bit (qubit), denoted as

$$|0\rangle \text{ and } |1\rangle.$$

Different from classical bits, the different states of qubits can exist simultaneously, for example,

$$|\psi\rangle = \alpha_0|0..0\rangle + \dots + \alpha_{2^N-1}|1...1\rangle,$$

which is known as the principle of quantum superposition. This feature indicates one of the powerful characteristics of quantum computers, known as quantum parallelism. We can execute operations in parallel on all possible input states,  $U|\psi\rangle$ , resulting in exponential speed-up compared with classical computers. Although for each measurement, only a single outcome can be returned due to irreversible state collapse, we can employ the schemes like adiabatic quantum computation<sup>[7]</sup> or quantum Fourier transformation<sup>[8]</sup> to

pick up the correct results of a quantum algorithm in a few samples with very high probability.

## 1.2 Trapped-ion quantum computer

To select the proper physical platforms for practical quantum computation, David DiVincenzo summarized the following criteria in 2000<sup>[9]</sup>,

1. A well-defined two-level-system to encode a qubit,
2. Long enough coherence time to perform quantum operations,
3. Near perfect initialization of qubits to a deterministic pure state,
4. Realization of a universal gate set,
5. Near perfect readout on states of qubits.

After filtering out, the remained physical platforms include such as trapped-ion systems, superconducting systems, linear optical systems, and quantum dots. Up to date, the laser-cooled trapped-ion system, which was proposed as the first candidate for quantum computation in 1995, is still one of the most promising platforms for the realization of large-scale quantum computers. Quantum information stored in a single ion qubit can keep alive over several seconds<sup>[10]</sup>, and can even exceed 10 minutes with the help of the dynamic decoupling techniques<sup>[11]</sup>, thus keeping the longest coherence time record among all physical platforms. A maximally entangled state was generated among 14 qubits in 2011<sup>[12]</sup>, and the entanglement size has been updated to 16 qubits recently. Meanwhile, the storage time of a four-qubit multipartite entangled state reaches 1.1 second<sup>[13]</sup>. The error rates of single- and two-qubit operations can be below  $10^{-5}$ <sup>[14]</sup> and  $10^{-3}$ <sup>[15]</sup>. Moreover, small programmable and controllable trapped-ion systems with tens of ion qubits have been realized in laboratories<sup>[16-17]</sup>.

However, quantum computers in the current stage are not able to perform their expected capabilities. The correct outputs of long depth quantum circuits would be overwhelmed by serious noises due to the limited lifetime of qubit coherence and the non-negligible error rates in quantum operations. The concept of fault-tolerant quantum computation<sup>[18-19]</sup> was proposed, claiming that we can achieve large-scale quantum computation by encoding a certain number of physical qubits into error-correctable logic qubits (quantum error correction, QEC) and suppress the error rates of quantum operations below certain thresholds (threshold theorem)<sup>[20]</sup>. For a full-fledged quantum computer, we might require thousands of well-controlled logical qubits, and the equivalent number

of physical qubits could reach tens of times, which is quite challenging to implement based on current techniques. Therefore, lots of researches have been conducted to develop useful near-term applications. One representative application is hybrid quantum computation by combining powerful classical computers with quantum processors to perform several optimization algorithms like variational quantum eigensolver<sup>[21]</sup> and quantum approximate optimization<sup>[22]</sup>. Another proposal, known as error mitigation, might help noisy quantum computers more practical on shallow quantum circuits by estimating the noise-free outputs through extrapolation<sup>[23]</sup> or compensating for operational errors by random circuits with quasi-probability sampling<sup>[23-24]</sup>. Now, we are stepping into the so-called "*noisy intermediate-scale quantum (NISQ) era.*"<sup>[25]</sup>

### 1.3 Thesis structure

In this thesis, we would introduce how to achieve a small-scale but fully controllable quantum computing system based on the trapped-ion platform. The details are organized as follows,

- In chapter 2, the mechanism of the ion trap would be introduced in the way of classical mechanics. The dynamics of a single charged particle confined in a radio-frequency potential would be revealed by intuitively obtaining pseudo-potentials or solving motional equations. The collective behaviors of multiple ions would be discussed, which play a crucial role in quantum computing based on trapped ions. At the end of this chapter, we would briefly introduce our experimental vacuum system.
- In chapter 3, we describe several features of ytterbium ions encoded as qubits. The methods of achieving high fidelity qubit state initialization and detection are introduced. Meanwhile, we give the derivation of single-qubit coherent manipulations by microwaves or Raman lasers. The experimental timing control is briefly introduced at the end.
- In chapter 4, we demonstrate the first quantum simulation to verify the quantum nonequilibrium work relation in the presence of decoherence. We employ a two-level system encoded in a single ion and engineer a controllable decohering effect. The influences of decoherence are studied when the system is driven at different speeds to do work. The experimental results first reveal the validity of the quantum nonequilibrium relation beyond the closed quantum system.

- In chapter 5, we first complement the schemes for implementing two-qubit entangling gates on the trapped-ion platform. To experimentally realize a fully controllable quantum computing system, we build an individual laser addressing system for fully independent control on each qubit. Meanwhile, the methods of initialization and detection are extended to the situation of multiple qubits. Finally, we introduce several schemes for achieving noise-insensitive gates.
- In chapter 6, beyond the universal gate set, we focus on the experimental realization of multi-qubit global entangling gates, which can provide speed-up in various quantum algorithms. By utilizing phase-modulated laser driving forces to precisely control the motional trajectories of multiple qubits in the phase space, we successfully implement the global entangling gates and create the maximally entangling state with up to four qubits in a single global operation. Moreover, the digitized adiabatic evolution algorithm of the ferromagnetic Ising model is demonstrated.
- In chapter 7, we give an outlook of the potential directions for future researches.

## Chapter 2 Trapped-ion system

The ion trap, specifically the Paul trap named after Wolfgang Paul (who shared the 1989 Nobel Prize in Physics with Norman Ramsey and Hans Dehmelt<sup>[26-28]</sup>), was developed initially as a mass spectrometer and a mass filter for charged particles<sup>[26]</sup>. In such a system, charged particles are injected axially, and only those particles with the proper charge-to-mass ratio could pass through the trap and be collected, while the others would hit electrodes and be lost. Meanwhile, researchers explored the possibility of dynamically stabilizing charged particles inside the trap, and called such a device as "Ionenkäfig" at the beginning, which is the prototype of the current ion trap. Compared with being a mass filter, charged particles are three-dimensionally confined in this device by adding an electrostatic potential in the axial direction. Clouds of Ba<sup>+</sup> and Mg<sup>+</sup> were observed in a Paul trap and a Penning trap in 1978<sup>[29-30]</sup>, respectively, with the help of the Doppler cooling techniques<sup>[31-32]</sup>. Two years later, a single Ba<sup>+</sup> was captured<sup>[33]</sup>, and then in 1981, a single Mg<sup>+</sup> was also caught<sup>[34]</sup>. More exciting progress happened in 1986 was that quantum jumps was observed for the first time by utilizing the trapped ions<sup>[35-37]</sup>. Soon after, in 1987, a phase transition between the crystalline phase and the gaseous phase was realized with multiple Mg<sup>+</sup> ions<sup>[38]</sup>. The next stage was surely the manipulation in the quantum level that began nearly 30 years ago and is still growing and developing<sup>[39]</sup>.

In this chapter, we will first describe the classical motion of a single ion trapped in a radio-frequency (RF) potential, giving an understanding of secular motion and micro-motion. Then the collective behaviors will be discussed when more than one ion is captured. Finally, we will make connections between above theories and experimental realizations by introducing our setup.

### 2.1 Classical dynamics of a single trapped ion

#### 2.1.1 Pseudo-potential

An intuitive way to restrict a single ion in a certain space is applying a binding force as follows,  $\vec{F} \propto -\vec{r}$ , where  $\vec{r} = \{x, y, z\}$  is the displacement from the equilibrium position of the ion. In principle, such force can be induced from a static quadratic electric potential

$\Phi$ , which can be expressed in Cartesian coordinates as,

$$\Phi(\vec{r}) = \frac{V}{2R^2} (\alpha_x x^2 + \alpha_y y^2 + \alpha_z z^2) = \sum_{m \in \{x,y,z\}} \Phi_m, \quad (2-1)$$

where all the quadratic coefficients  $\alpha_m$  should be positive. Unfortunately, the realization of the above quadratic potential is forbidden in reality due to the restriction of Maxwell's equations in free space,  $\nabla \cdot E = -\nabla^2 \Phi = 0$ , which leads to a constraint of

$$\sum_{m \in \{x,y,z\}} \alpha_m = 0. \quad (2-2)$$

This constraint conflicts with the previous requirement of  $\alpha_m > 0$ , indicating that the ion must escape in a certain direction. Therefore, the ion cannot be three-dimensionally trapped by the static electric fields, known as Earnshaw's theorem<sup>[40]</sup>.

Although the simplest method of using the static potential gives us a dead end, another option comes out that we can utilize a RF potential,  $\Phi \cos(\Omega_{\text{rf}} t)$ , to dynamically stabilize the ion. Intuitively speaking, the ion will be drawn back before escaping due to the alternating potential.

In detail, the ion with a mass of  $M$  and a charge of  $e$  suffers from a time-dependent force as follows,

$$\vec{F} = M\ddot{\vec{r}} = e\vec{E}(\vec{r}) \cos(\Omega_{\text{rf}} t), \quad (2-3)$$

where  $\vec{E}(\vec{r}) = -\nabla\Phi$ . Due to the position dependence of the electric field  $\vec{E}$ , it is almost impossible to solve Eq. (2-3) analytically. Instead, we treat the position-dependent part as a small perturbation  $\vec{E}_\epsilon$ , which can be ignored for now by approximating  $\vec{E}(\vec{r}) = \vec{E}(\vec{r}_0) + \vec{E}_\epsilon$  as  $\vec{E}(\vec{r}_0)$ . Then we can obtain the trajectory of the ion by integrating Eq. (2-3) with the initial conditions of  $\vec{r}(0) = \vec{r}_0$  and  $\dot{\vec{r}}(0) = 0$ ,

$$\vec{r} - \vec{r}_0 = \frac{e\vec{E}(\vec{r}_0)}{M\Omega_{\text{rf}}^2} (1 - \cos(\Omega_{\text{rf}} t)). \quad (2-4)$$

With Eq. (2-4), the first-order perturbation of the electric field can be estimated as,

$$\begin{aligned} \vec{E}_\epsilon^{(1)} &\approx ((\vec{r} - \vec{r}_0) \cdot \nabla) \vec{E} \\ &= \frac{e}{M\Omega_{\text{rf}}^2} (1 - \cos(\Omega_{\text{rf}} t)) (\vec{E} \cdot \nabla) \vec{E} \\ &= \frac{e}{2M\Omega_{\text{rf}}^2} (1 - \cos(\Omega_{\text{rf}} t)) \nabla |\vec{E}|^2. \end{aligned} \quad (2-5)$$



The last line is obtained due to the relations of

$$\left(\vec{E} \cdot \nabla\right) \vec{E} = \frac{1}{2} \nabla |\vec{E}|^2 - \nabla \times \left(\nabla \times \vec{E}\right), \quad (2-6)$$

$$\nabla \times \vec{E} = 0. \quad (2-7)$$

By including the perturbation of the electric field into Eq. (2-3), the net effect of the total electric field can be extracted by averaging the time-dependent force,

$$\langle \vec{F} \rangle \approx -e \left\langle \left( \vec{E}(\vec{r}_0) + \vec{E}_\varepsilon^{(1)} \right) \cos(\Omega_{\text{rf}} t) \right\rangle. \quad (2-8)$$

All the fast oscillating terms are zeroed after time averaging, and the only remained effect can be expressed as,

$$\langle \vec{F} \rangle \approx -\frac{e^2}{4M\Omega_{\text{rf}}^2} \nabla |\vec{E}|^2 = -e \nabla \Phi_p, \quad (2-9)$$

which can be treated as an effective force induced from a pseudo-potential of

$$\Phi_p = \frac{e}{4M\Omega_{\text{rf}}^2} \nabla |\vec{E}|^2. \quad (2-10)$$

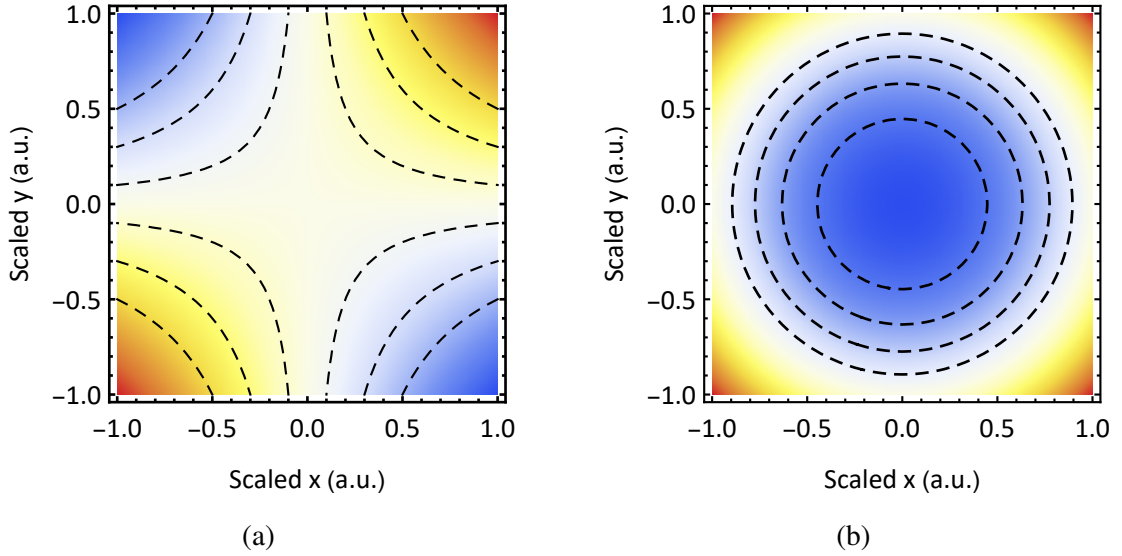


Figure 2.1 Density plot of a two-dimensional static quadrupole potential and the pseudo-potential obtained from the corresponding oscillating potential.

Assuming that the time-independent part of the electric potential,  $\Phi$ , has the form of the Eq. (2-1), we can obtain the pseudo-potential in the following form,

$$\Phi_p = \frac{eV^2}{4MR^4\Omega_{\text{rf}}^2} \sum_m \alpha_m^2 r_m^2. \quad (2-11)$$

The result has positive quadratic coefficients for all the directions, as shown in Fig. 2.1 (b), and reveals the capability of capturing the charged ion. Meanwhile, we can obtain the effective trap frequencies of  $\nu_m = eV\alpha_m/\sqrt{2}MR^2\Omega_{\text{rf}}$  for each direction.

### 2.1.2 Approximate solution of Mathieu equation

After getting an intuitive explanation of dynamically trapping a single ion with the oscillating field, we have to carefully revisit the high-frequency motion of the ion that is smoothed due to time averaging. For this purpose, we have to mathematically find the solution of the differential equation of Eq. (2-3). To simplify the problem, we only focus on the equation of the motion in one direction, for example, the x-direction here,

$$\ddot{x} + \frac{eV\alpha_x}{MR^2}x \cos(\Omega_{\text{rf}}t) = 0. \quad (2-12)$$

Note that, the above equation is equivalent to Mathieu equation<sup>[41]</sup>,

$$\frac{d^2x}{d\tau^2} + (a_x + 2q_x \cos(2\tau))x = 0, \quad (2-13)$$

with  $\tau = \Omega_{\text{rf}}t/2$ ,  $a_x = 0$  and  $q_x = 2qV\alpha_x/(MR^2\Omega_{\text{rf}}^2)$ . Instead of obtaining the exact solution of Eq. (2-13), let us approximate it to be

$$\begin{aligned} x(\tau) &\approx x^{(0)}(\tau) + x^{(1)}(\tau) \\ &= A_0 \cos(\beta_x \tau) + A_1 \cos((\beta_x + 2)\tau) + A_{-1} \cos((\beta_x - 2)\tau). \end{aligned} \quad (2-14)$$

Here, the 0th order,  $x^{(0)}(\tau)$ , should correspond to the oscillation at the frequency of the pseudo-potential  $\nu_x$ , and  $x^{(1)}(\tau)$  includes the first-order high-frequency oscillations. All the other high-order terms are ignored due to  $q_x \ll 1$  in practice.  $\beta_x$  and  $A_{0,1,-1}$  are the undetermined coefficients. By inserting Eq. (2-14) into Eq. (2-13), the equation can be organized to be the form of

$$\begin{aligned} &(A_1 q_x + A_{-1} q_x - A_0 \beta_x^2) \cos(\beta_x \tau) + \\ &(A_0 q_x - A_1 (\beta_x + 2)^2) \cos((\beta_x + 2)\tau) + \\ &(A_0 q_x - A_{-1} (\beta_x - 2)^2) \cos((\beta_x - 2)\tau) = 0, \end{aligned} \quad (2-15)$$

where the terms of  $\cos((\beta_x \pm 4)\tau)$  are ignored. Because Eq. (2-15) should be established for arbitrary  $\tau$ , the coefficients of all the cos term should be zero, yielding an equation of

$\beta_x$ ,

$$q_x^2 \frac{2\beta_x^2 + 8}{(\beta_x^2 - 4)^2} = \beta_x^2. \quad (2-16)$$

Apparently under the assumption of  $q_x \ll 1$ , Eq. (2-16) has a solution of

$$\beta_x \approx \frac{q_x}{\sqrt{2}}. \quad (2-17)$$

By inserting the solution of  $\beta_x$  back to the Eq. (2-15) and Eq. (2-14), we obtain the approximated trajectory of the ion in the x-direction,

$$x(\tau) \approx A_0 \cos\left(\frac{q_x}{\sqrt{2}}\tau\right) \left(1 + \frac{q_x}{2} \cos(2\tau)\right), \quad (2-18)$$

or

$$x(t) \approx A_0 \cos(\nu_x t) \left(1 + \frac{q_x}{2} \cos(\Omega_{\text{rf}} t)\right). \quad (2-19)$$

Here  $A_0$  can be determined by the initial condition. The oscillation with the frequency of  $\nu_x = qV\alpha_x/\sqrt{2}MR^2\Omega_{\text{rf}}$ , called as secular motion, is consistent with the result we obtained from the pseudo-potential. Meanwhile, we have an additional oscillation with a much higher frequency of  $\Omega_{\text{rf}}$ . This fast modulation superimposed on the secular motion is directly related to the oscillation of the electric potential, called micro-motion, or intrinsic micro-motion, as shown in Fig. 2.2. Since the value of  $q_x$  is quite small, the effect of the intrinsic micro-motion can be ignored in principle.

However, if an extra direct-current (DC) electric field of  $E_{\text{DC}}$  exists in space, it would shift the equilibrium position of the ion, and we should modify the trajectory of Eq. (2-19) to be

$$x(t) \approx (x_{\text{DC}} + A_0 \cos(\nu_x t)) \left(1 + \frac{q_x}{2} \cos(\Omega_{\text{rf}} t)\right), \quad (2-20)$$

where  $x_{\text{DC}} = qE_{\text{DC}}/M\nu_x^2$ . This excess micro-motion, which can be estimated as  $x_{\text{DC}}q_x \cos(\Omega_{\text{rf}} t)/2$ , can be huge depending on the amplitude of the DC field, and then destroy coherent manipulations of the ion. Therefore, in practice, additional DC electrodes are required to compensate for the unwanted DC electric field and minimizing the excess micro-motion<sup>[42]</sup>. Note that the equilibrium position without the extra electric field is called "RF null" because the RF field has a zero amplitude but a finite gradient here.

In the experimental realization, the RF field is typically applied in only two directions, labeled as x and y. A conventional apparatus to generate such a field is four-cylinder

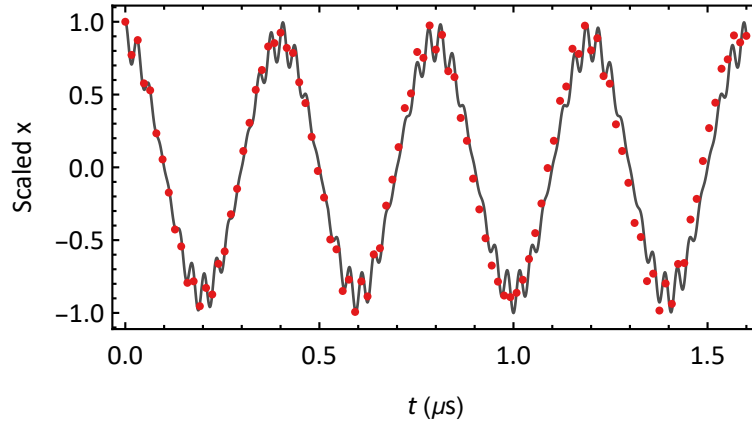


Figure 2.2 Classical motion of a single ion in an RF oscillating potential. Here, we assume the frequency of the oscillating potential is  $\Omega_{\text{rf}} = 2\pi \times 32$  MHz, and the frequency of the secular motion is  $\nu_x \approx 2\pi \times 2.5$  MHz. From the trajectory in the  $x$ -direction, we can distinguish the secular motion and the micro-motion. The black line refers to the approximated solution according to Eq. (2-19), while the red dots are obtained by numerically solving Eq. (2-12). Because  $q_x \approx 0.22$  here is a quite large value, the numerical results deviate slightly from the approximated solution.

electrodes that are parallel to each other in the  $z$ -direction<sup>[26]</sup>, as shown in Fig. 2.3. By alternatively applying the RF and the DC field to each rod, an oscillating electric quadrupole field is created in the central region surrounded by the four rods due to the geometric symmetry. In principle, we can generate a multipole field by increasing the number of rods, which has additional advantages in some applications and see further discussion in the App. A. The confinement in the rest  $z$ -direction is achieved by adding extra needles at both ends in the  $z$ -direction. By applying proper DC voltages to the needles, a DC potential can be generated along the  $z$ -direction.

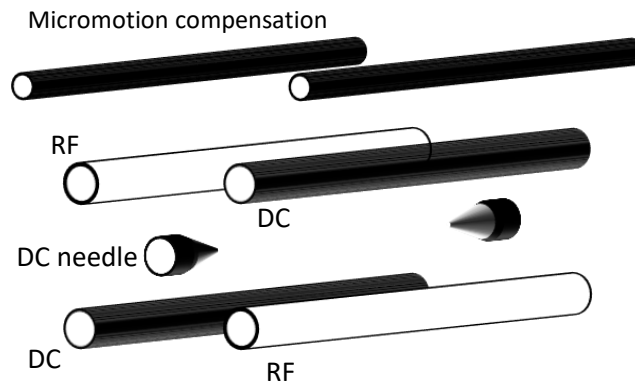


Figure 2.3 Conventional four-rod trap. DC voltages are applied to the rods shown in black, while RF voltages are applied to the white rods. Above two rods are used to compensate for the extra electric field in space and then minimize the excess micro-motion.

## 2.2 Collective motion of a single ion-chain

Now we move to the situation with more than one ion, where an ion-chain is approximated as being confined in a three-dimensional harmonic potential, with trap frequencies of  $\nu_x$ ,  $\nu_y$ , and  $\nu_z$  in each direction, respectively. When multiple ions are captured, the confinements from the harmonic potential pull the ions together into the center of the trap, while the Coulomb force pushes them apart. The competition between the attractive and the repulsive interactions re-balances the equilibrium positions of all the ions, resulting in a Coulomb crystal. Typically because the effective frequencies of the pseudo-potential in the x-y plane are much larger than that of the z-direction ( $\nu_x, \nu_y \gg \nu_z$ ), the ions are distributed along the z-direction and form a one-dimensional ion-chain.

In the experiment, we first care about equilibrium positions of all the ions for the reason of precise laser alignment. For the ion chain consisting of  $N$  ions, the total potential energy can be expressed as,

$$V(\{\vec{r}_i\}) = \sum_{i,k} \frac{1}{2} M \nu_k^2 r_{i,k}^2 + \frac{e^2}{4\pi\epsilon_0} \sum_{i<j} \left[ \sum_k (r_{i,k} - r_{j,k})^2 \right]^{-1/2} = V_1 + V_2, \quad (2-21)$$

where  $\vec{r}_i = \{r_{i,1}, r_{i,2}, r_{i,3}\} = \{x_i, y_i, z_i\}$  are the coordinates of the  $i$ -th ion.  $V_1$  and  $V_2$  originate from the three-dimensional harmonic potential and the Coulomb interaction, respectively. According to the classical mechanics, the net force on each ion should be zero when the whole system reaches equilibrium, indicating that,

$$F_{i,k} = -\frac{\partial V}{\partial r_{i,k}} = 0, \quad (2-22)$$

should be established for any  $\{i, k\}$ . From the above  $3N$  equations, we can obtain the equilibrium positions  $\{r_{i,k}^{\text{eq}}\}$  for all the ions. Moreover, based on the assumption of  $\nu_x, \nu_y \gg \nu_z$ , we would directly have the solutions of  $r_{i,1}^{\text{eq}} = r_{i,2}^{\text{eq}} = 0$  for all  $i$ . From another aspect, the energy of the ion-chain should reach a minimum when all the ions are in their equilibrium positions, which indicates that we can also obtain the equilibrium positions by searching the minimum of the objective function  $V(\{\vec{r}_i\})$ .

Now we investigate the motion of the ions. For a single ion, it would vibrate harmonically at the frequencies of  $\nu_m$  in the  $m$ -direction. However, for the multi-ion case, an individual ion, which vibrates near its equilibrium position, would also excite the vibrations of the rest ions, due to the Coulomb interaction. Mathematically, we can approximate the harmonic vibration of each ion by expanding the total potential energy

to the second-order near the equilibrium positions,

$$V(\{\vec{r}_i\}) = V(\{\vec{r}_i^{\text{eq}}\}) + \frac{1}{2} \sum_{i,j,k,l} \frac{\partial^2 V}{\partial r_{i,k} \partial r_{j,l}} \Big|_{r_{i,k}^{\text{eq}}, r_{j,l}^{\text{eq}}} \delta r_{i,k} \delta r_{j,l}, \quad (2-23)$$

where  $\delta r_{i,k} = r_{i,k} - r_{i,k}^{\text{eq}}$  is the local displacement from the equilibrium position. The first-order of the expansion vanishes due to the requirement of Eq. (2-22). Note that, due to  $\partial^2 V / \partial r_{i,k} \partial r_{j,l} = 0$  if  $k \neq l$ , we can fully separate Eq. (2-23) into three independent parts and focus on one of the directions,

$$V_k(\{r_{i,k}\}) = \sum_{i,j} \gamma_{i,j}^{(k)} \delta r_{i,k} \delta r_{j,k}. \quad (2-24)$$

Here the constant part of the total energy is ignored and the coefficients  $\{\gamma_{i,j}^{(k)}\}$  can be written in the following form,

$$\gamma_{i,j}^{(k)} = \begin{cases} M v_k^2 + \frac{1}{2} \frac{\partial^2 V_2}{\partial r_{i,k}^2} \Big|_{r_{i,k}^{\text{eq}}} = M(v_k + \Delta v_k)^2 & i = j \\ \frac{1}{2} \frac{\partial^2 V_2}{\partial r_{i,k} \partial r_{j,k}} \Big|_{r_{i,k}^{\text{eq}}, r_{j,k}^{\text{eq}}} & i \neq j \end{cases}. \quad (2-25)$$

The above coefficients reveal two effects induced by the Coulomb interaction, (a) the frequencies shift of the local vibrations ( $\gamma_{i,i}$ ) and (b) the couplings of different local vibrations ( $\gamma_{i,j}$ ). Therefore, the local vibration of each ion would be pretty complicated. However, the quadratic form of Eq. (2-24) indicates that we can find linear combinations,

$$\delta r_{i,k} \rightarrow \delta R_{i,k} = \sum_j b_{i,j}^{(k)} \delta r_{j,k}, \quad (2-26)$$

to reduce Eq. (2-24) to the diagonal form of,

$$V_k = \sum_i \lambda_i^{(k)} \delta R_{i,k}^2 = \frac{1}{2} M \sum_i v_{i,k}^2 \delta R_{i,k}^2. \quad (2-27)$$

Here  $\lambda_i^{(k)}$  and  $\{b_{i,j}^{(k)}\}$  is the  $i$ -th eigenvalue and eigenvector of the matrix  $\{\{\gamma_{i,j}^{(k)}\}\}$ , respectively. This result reveals the collective motion of the multiple ions, known as the normal modes. If we perform a Fourier transform on the motion of the ions, we could observe  $N$  vibration modes for each direction in the frequency domain, with the frequencies of,

$$v_{i,k} = \sqrt{2\lambda_i^{(k)} / M}. \quad (2-28)$$

for each mode.  $v_{i,k}$  is called as the frequency of the  $i$ -th normal mode in the  $k$ -direction. Meanwhile, the relative oscillating amplitude and phase of the  $j$ -th ion in the  $i$ -th mode is

given by the value of  $b_{i,j}$ . The matrix consisting of all the eigenvectors,  $\mathbf{B}^{(k)} = \{\{b_{i,j}^{(k)}\}\}$ , is called as the normal mode transformation matrix<sup>[43]</sup>.

Here we use a three-ion chain as an example to illustrate the properties of the collective motion. In this case, the equilibrium positions can be analytically solved from the equations of Eq. (2-22), which can be written as,

$$\begin{aligned}
 \text{ion 1} & \quad \left( 0, 0, -\sqrt{\frac{3e^2}{8\pi\epsilon_0 M v_z^2}} \right), \\
 \text{ion 2} & \quad (0, 0, 0), \\
 \text{ion 3} & \quad \left( 0, 0, \sqrt{\frac{3e^2}{8\pi\epsilon_0 M v_z^2}} \right).
 \end{aligned} \tag{2-29}$$

The transformation matrices in all the three directions are identical and given by,

$$\mathbf{B} = \begin{pmatrix} 1/\sqrt{3} & 1/\sqrt{3} & 1/\sqrt{3} \\ 1/\sqrt{2} & 0 & -1/\sqrt{2} \\ -1/\sqrt{6} & 2/\sqrt{6} & -1/\sqrt{6} \end{pmatrix}. \tag{2-30}$$

For the normal mode determined by the first row, all the ions oscillate uniformly, called center-of-mass (COM) mode, as shown in Fig. 2.4. Apparently, the frequency of the COM mode should be consistent with the trap frequency in each direction,  $\nu_{k,\text{COM}} = \nu_k$ . Moreover, the components of the eigenvector for the COM mode can be generalized to be  $1/\sqrt{N}$  for the  $N$ -ion case.

The behaviors of the motional spectrum are different between the axial and the transverse directions, as shown in Fig. 2.4. For the  $z$ -direction, or usually called as the axial direction, the COM mode has the lowest mode frequency. For the other mode in the  $z$ -direction, for example, the second "breathing" mode or the last "zigzag" mode, the ions move towards each other, leading to a rapid increase of the total energy of the system. Therefore, compared with the COM mode, the rest of the modes always have higher mode frequencies. On the contrary, for the  $x$ -direction and  $y$ -direction (transverse directions), the COM mode has the highest frequency, because the motion of the ions is perpendicular to the  $z$ -direction; the ions tend to stay away from each other except the COM mode.

Note that, for a harmonic potential in the axial direction, the nearby ion-spacing would be non-uniform when the number of ions is larger than three. Several efforts have been pushed to achieve the equal-spacing by applying an anharmonic axial potential. The details are discussed in Ref. [44-46].

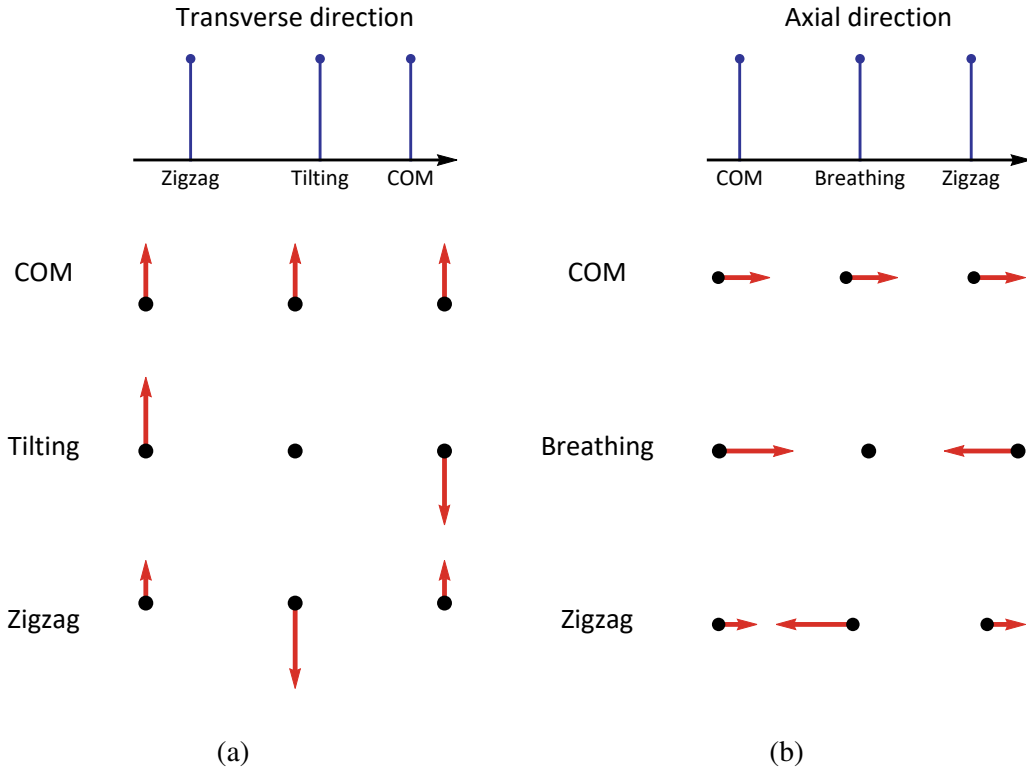


Figure 2.4 Collective motion of a three-ion chain. In each sub-figure, we present the pattern of each normal mode and show the order of their frequencies in the frequency domain. (a) and (b) refer to the transverse and axial directions, respectively.

### 2.3 Experimental setup

In this section, we would briefly describe our experimental setup in practice. For the detailed discussion of vacuum system and its assembling, please check previous theses of our group (Ye Wang<sup>[47]</sup>, Shuoming An<sup>[48]</sup>). As shown in Fig. 2.5, this is the ion-trap device in our lab. To stably confine ions in the trapping potential, we should minimize the effects of background collisions from the particles in the air. Therefore, we seal the whole ion trap in an ultrahigh vacuum (UHV) system, where the air pressure of less than  $10^{-11}$  Torr is maintained by a continuously running ion pump. The titanium sublimation pump here is used to regularly improve the system vacuum further. Under this situation, the lifetime of a single trapped ion can reach several days.

The trap itself is held inside a vacuum chamber, which has eight optical viewports for optical access, as shown in Fig. 2.5. In our current setup, instead of using the conventional four-rod trap shown in Fig. 2.3, we have already updated to a new version of blade trap, which is initially designed by the ion-trap group in the University of Maryland<sup>[49]</sup>. In this design, all the cylinder electrodes are replaced by the much thinner electrodes in a



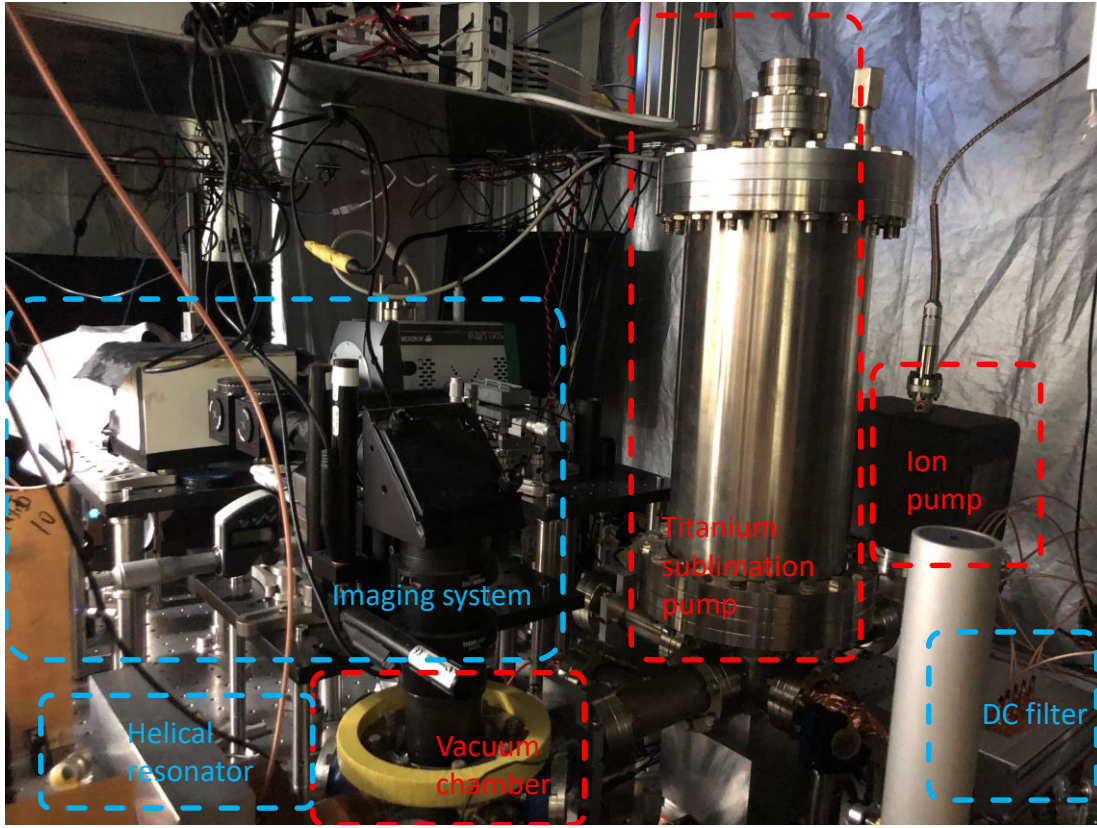


Figure 2.5 Experimental setup in practice. The whole vacuum system is separately shown in several red dashed boxes, while the other main parts are marked in the blue dashed boxes.

blade shape, as illustrated in Fig. 2.6. Here, both DC electrodes are separated into five segments, which is achieved by the conventional laser cutting, and the applied voltage on each DC segment can be independently controlled. Although the RF electrodes are also segmented to guarantee the geometric symmetry of the whole trap structure, the segments in each RF blade are electrically connected. In Fig. 2.6 (d), we show the estimated size of our trap used in the experiment.

Compared with the four-rod trap, this segmented blade trap has several advantages. In Fig. 2.6 (a), it is evident that the DC needles are not required here, and the confinement in the axial direction is generated by the high voltages applied to the edge DC segments (for example, DC1 and DC5 in Fig. 2.6 (c)). By varying the voltages from around 40 V to 90 V, the axial trap frequency can be tuned from  $2\pi \times 0.3$  MHz to  $2\pi \times 0.6$  MHz. Moreover, by carefully adjusting the voltages applied to the center three segments (DC2, DC3, DC4), an anharmonic potential along the axial direction can be achieved, to make a few ions equally spaced. For now, we apply the same voltage, which is much lower than that of the edge segment, to the central three DC segments ( $U_{DC1}/U_{DC3} > 10$ ); therefore, the axial

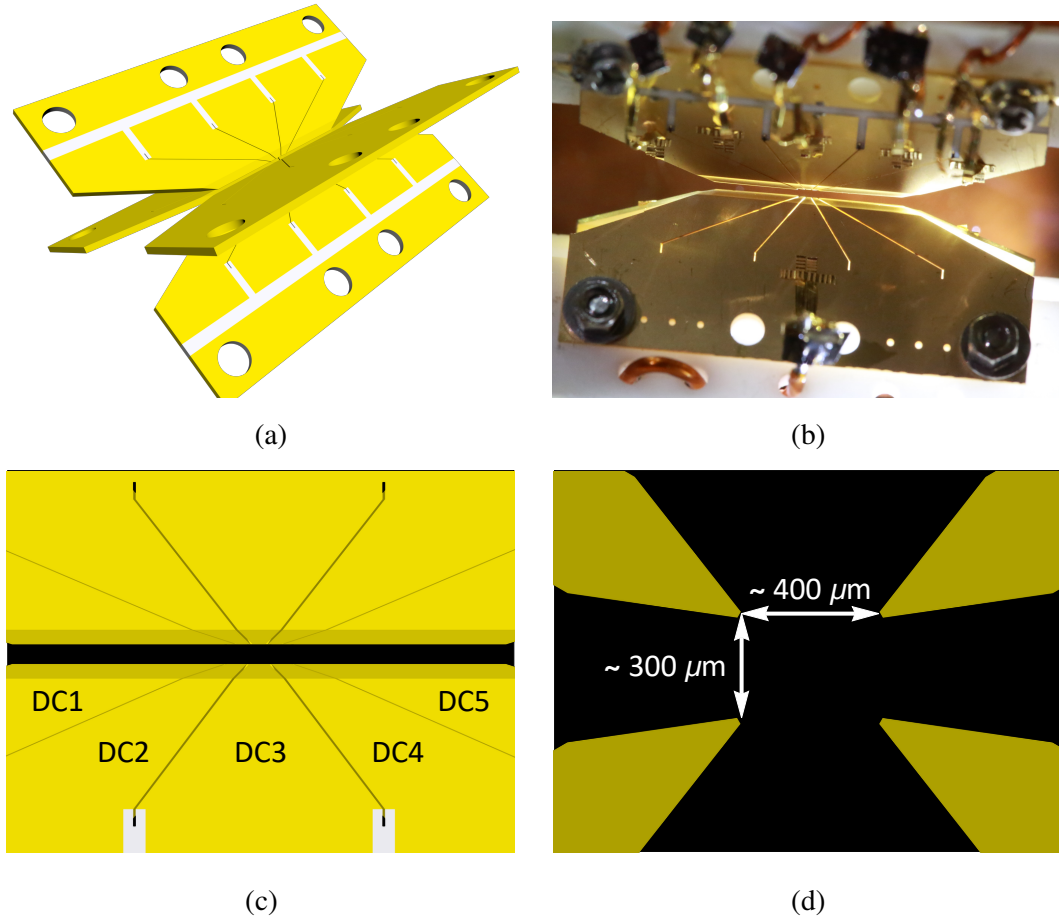


Figure 2.6 Structure of blade trap. (a) 3D modeling of the blade trap. Except for the different shapes of the electrodes, it is similar to the conventional four-rod trap shown in Fig. 2.3. (b) Blade trap used in the experiment. (c) Top view of the blade trap. The segmented electrodes can be observed. There are five segments in each DC electrode which can be independently controlled. The RF electrodes are segmented as well but electrically connected by coating the whole blade with gold. (d) Side view of the blade trap. We intentionally assemble the four blades into a rectangular shape, with the ion-electrode distance of  $\sim 250 \mu\text{m}$ .

potential can be well approximated as a harmonic potential. All the DC voltages pass the DC filters with a cut-frequency of around 1.5 kHz (shown in Fig. 2.5) before connected to the blades, to filter out most of electric noises.

The RF signal is delivered to the RF blades through a helical resonator (HR) with a quality factor of  $Q \sim 200$ , which works as the voltage amplifier and narrow bandpass filter<sup>[50]</sup>. The frequency of the RF field is chosen to be  $\sim 2\pi \times 20$  MHz, and increased to  $\sim 2\pi \times 32$  MHz later, to reduce the value of  $q_x$  which discussed in Sec. 2.1. The amplitude of the RF field is partially picked up from a capacitor-circuit inside the HR and then utilized to achieve the stabilization of the radial trap frequencies<sup>[51]</sup>, see in App. B. Note that we should employ a bifilar-type HR, which has two coils to connect to two RF blades, respectively, as shown in Fig. 2.7. We can apply different DC offsets to each RF field to achieve the micro-motion compensation. The two coils inside the HR are connected by a capacitor to balance the phases of the two RF fields.

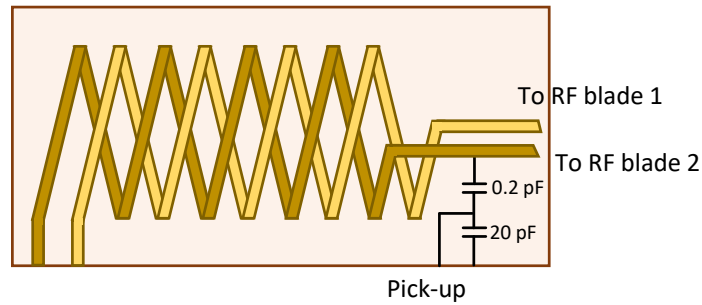


Figure 2.7 Helical resonator with bifilar structure. The inside capacitors are used to pick up a part of the RF signal (around 1%) for the feedback.

## Chapter 3 Qubit encoded with Ytterbium ion and single-qubit operations

At the current stage, all potential atomic ions for quantum computation can be categorized as hydrogen-like ions, for example,  $\text{Be}^+$  (NIST<sup>[52-53]</sup>),  $\text{Mg}^+$  (NIST<sup>[54-55]</sup>),  $\text{Ca}^+$  (University of Innsbruck<sup>[56-57]</sup>, University of Oxford<sup>[58-59]</sup>),  $\text{Ba}^+$  (Washington University<sup>[60-61]</sup>, UCLA<sup>[62]</sup>),  $\text{Yb}^+$  (University of Maryland<sup>[16,63]</sup>, University of Sussex<sup>[64-65]</sup>). The hydrogen-like ions have the simplest energy structure and a closed-cycle optical transition between the states  $^2S_{1/2}$  and  $^2P_{1/2}$ , while the latter facilitates high-efficiency laser cooling, high-fidelity initialization and readout of quantum states of the ion qubits<sup>[14,63,66-67]</sup>. Other parameters such as the mass of the ion, the wavelength of the cycle transition, the value of the nuclear spin, and the lifetime of the metastable  $^2D$  level would be taken into consideration when choosing the species of ion<sup>[68]</sup>.

A qubit, or specifically a two-level system, is encoded in energy levels of a single ion. One of the encoding options is utilizing hyperfine levels belong to the ground manifold  $^2S_{1/2}$  for the isotopes with a non-zero nuclear spin<sup>[63]</sup>. The relaxation time ( $T_1$ ) of the hyperfine qubit can be longer than the age of universe. Meanwhile, the "clock state" in the ground manifold with  $m_F = m_{F'} = 0$  is insensitive to magnetic field fluctuations due to the vanishing of the first order Zeeman shift at zero magnetic field, resulting in the longest coherence time ( $T_2$ ) compared with other platforms<sup>[11]</sup>. The energy gap of the hyperfine qubit is typically around several GHz. Another popular encoding scheme is utilizing optical levels belong to the ground manifold  $^2S_{1/2}$  and the metastable manifold  $^2D$  separately, and the energy gap of such a qubit falls into the optical region ( $\sim 10^2$  THz). Such kind of optical qubit has the advantage of ultra-high quality readout with near unit fidelity, but suffers from the limited  $T_1$  time and the narrow linewidth ( $\sim 1$  Hz) laser for qubit manipulation. state<sup>[69-70]</sup>.

In our system, we choose ytterbium (Yb), specifically  $^{171}\text{Yb}^+$ , to encode our ion qubit. In this chapter, we first detail the energy structure of  $^{171}\text{Yb}^+$ . Then we will show how to achieve laser cooling, qubit initialization, and state readout through the cyclic transition. Finally, for quantum computing, we discuss coherent manipulations on a single ion qubit.

### 3.1 Single $^{171}\text{Yb}^+$ qubit and its initialization & detection

The nuclear spin of  $^{171}\text{Yb}^+$  is  $1/2$ , leading to an energy structure shown in Fig. 3.1<sup>[63]</sup>. The physical qubit is encoded in the hyperfine levels belong to  $^2S_{1/2}$ , denoted as  $|1\rangle = |F = 1, m_F = 0\rangle$  and  $|0\rangle = |F = 0, m_F = 0\rangle$ , with a bare energy gap of 12.642812118466 GHz at  $B = 0$ <sup>[71]</sup>. An external static magnetic field of 6 Gauss induces a second-order Zeeman shift of  $\sim 11$  kHz in the qubit splitting. The wavelength of the cycle transition is near 369.526 nm, which can be generated from commercial laser systems and is still friendly to fiber transitions. Note that this cycle transition is not fully closed because of the decay channel from  $^2P_{1/2}$  to  $^2D_{3/2}$  with a branching ratio of 0.5%<sup>[63]</sup>. Therefore, an additional 935 nm laser with a 3.07 GHz sideband is applied all the time to bring the leaking state back to the cycle. Meanwhile, background collisions may transfer the state of ion to the  $^2F_{7/2}$  manifold and make the ion "dark", which can be recovered by a laser of 638 nm. Moreover, to repump the leakage in the  $^2F_{7/2}$  manifold, except 638 nm we mentioned, and 760 nm<sup>[72]</sup> and 355 nm<sup>[73]</sup> lasers used in some groups, we found that a laser of 375 nm can work as well. The most probable transition is from the  $^2F_{7/2}$  level to the  $^3F [1/2]_{3/2}$  level, which is resonant at the wavelength of 375.856 nm<sup>[74]</sup>.

The Yb ions are loaded by ionizing neutral atoms. The first ionization energy of Yb atom is 6.25416 eV<sup>[75]</sup>, which is equivalent to a photon with the wavelength of 198.242 nm. To avoid using such deep ultraviolet (UV) laser, we take a two-step ionization method<sup>[63,76]</sup>. A photon with the wavelength of 398.911 nm first excites the neutral Yb atom from the  $^1S_0$  level to the  $^1P_1$  level. Then the wavelength of the second photon should be less than 394.088 nm in order to excite the outermost electron into the continuum region. Note that, the 369.526 nm laser satisfies the requirement for the second step excitation, or in some cases 355 nm or 375 nm laser is utilized. In practice, an oven filled with the neutral Yb source is placed inside the vacuum chamber and heated by applying a constant current. The atoms are thermally ejected from the oven, with a small portion passing through the center of the trap. The laser beams of 398.911 nm and 369.525 nm are aligned to overlap with the ejected atoms at the trap center. Therefore, the atoms in this region can be ionized, and captured after efficient cooling. Due to the isotope shift, we can selectively ionize different isotopes by finely tuning the wavelength of 398.911 nm laser, and the path of lasers is preferably perpendicular to the atomic flow to suppress Doppler shifts.

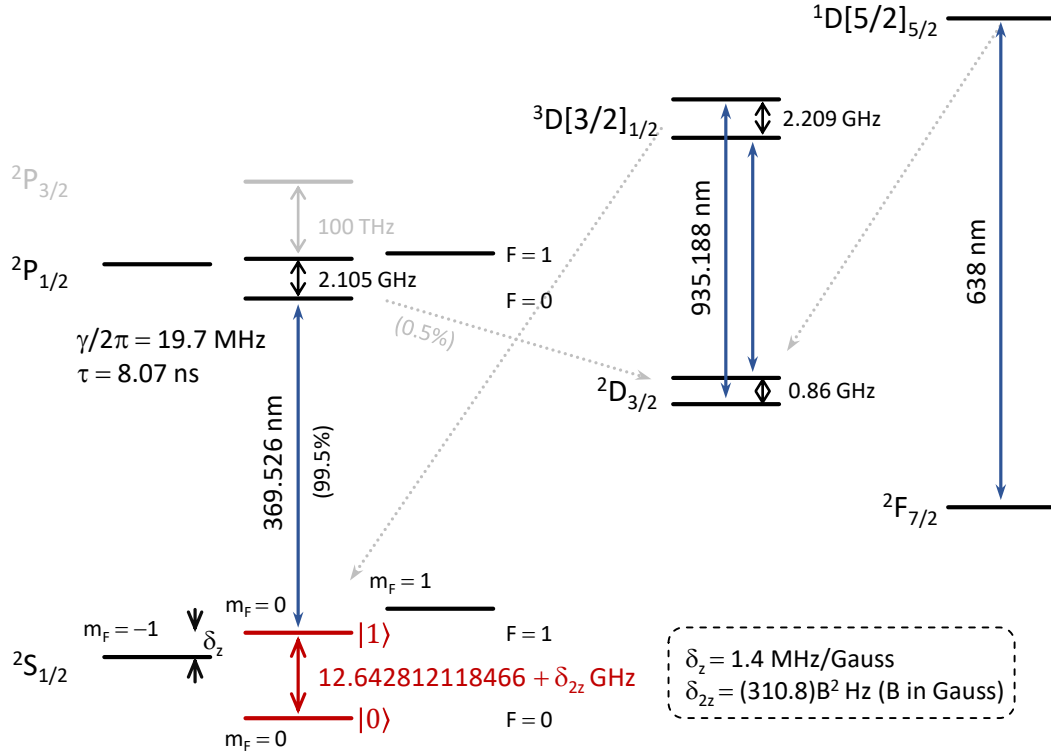


Figure 3.1 Energy structure of  $^{171}\text{Yb}^+$ . The qubit is encoded in the hyperfine levels belonging to the ground manifold  $^2S_{1/2}$ , shown in red color. Due to the non-zero external static magnetic field ( $\sim 6$  Gauss), the derivative of the qubit energy gap  $\omega_q$  with magnetic field ( $\partial\omega_q/\partial B$ ) is around 3.7 kHz/Gauss. The main optical transitions are shown in the blue lines, and the related decay channels are shown in the gray-dotted lines. With the help of repumping lasers, the cycle transition  $^2S_{1/2} \leftrightarrow ^2P_{1/2}$  is effectively closed.

### 3.1.1 Doppler cooling

After the ionization, the average speed of the Yb ions can be over hundred meters per second according to Maxwell velocity distribution (the melting point at the standard pressure is 824 °C), and such "hot" ions are easy to escape from the trap potential and hard to crystallize. Therefore, a cooling process is necessary. The ions can be laser cooled by applying a laser beam which wavelength is red-detuned from the cycle transition, known as Doppler cooling<sup>[31-32]</sup>, as shown in Fig. 3.2. The ion would lose (obtain)  $\hbar\vec{k}$  momentum during the absorption process when ion move opposite to (away from) the laser beam, where  $|\vec{k}| = 2\pi/\lambda$  is the momentum of a single photon. Due to the Doppler effect, the wavelength of incident photons shifts by a value of  $-\vec{k} \cdot \vec{v}$  in the ion-frame. Therefore, when the ion moves oppositely to the beam, it absorbs more photons than when it moves away because, in the latter case, the wavelength is more detuned from the resonance. The spontaneous emission after absorption is homogeneous, and the average momentum-

changing turns out to be zero. Overall the ion tends to lose momentum and be slowed down.

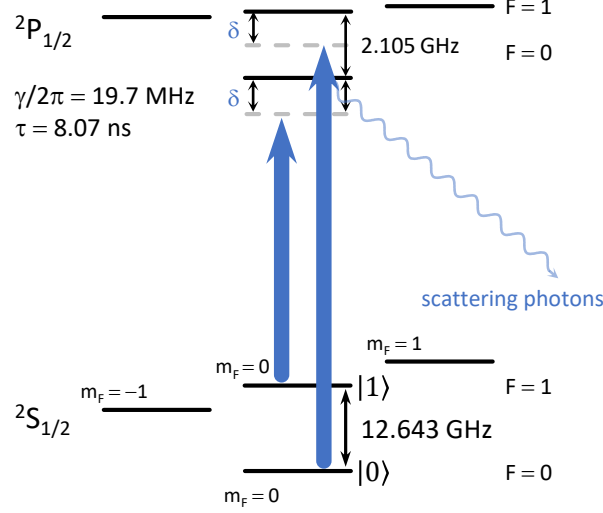


Figure 3.2 Implementation of the Doppler cooling. Two cycle transitions,  ${}^2S_{1/2} |F = 1\rangle \leftrightarrow {}^2P_{1/2} |F = 0\rangle$  and  ${}^2S_{1/2} |F = 0\rangle \leftrightarrow {}^2P_{1/2} |F = 1\rangle$ , are driven simultaneously to cover all hyperfine structures and avoid dark states. Here, we do not show the polarizations of the cooling laser. For an efficient cooling process, all the polarizations are required.

To find the optimal values for red-detuning and laser intensity, we first ignore the hyperfine structures in the  ${}^2S_{1/2}$  and  ${}^2P_{1/2}$  manifold and treat them as a two-level system (different from the two-level system of the qubit). The damping force  $\vec{F}$  induced by the cooling laser can be modeled as<sup>[77]</sup>,

$$\vec{F}(\vec{v}) = \hbar \vec{k} R_{\text{scatt}} = \hbar \vec{k} \frac{s_0 \gamma / 2}{1 + s_0 + 4(\delta - \vec{k} \cdot \vec{v})^2 / \gamma^2}. \quad (3-1)$$

Here  $R_{\text{scatt}}$  is the scattering rate of the upper  ${}^2P_{1/2}$  level,  $\delta$  is the value of the red-detuning, and  $s_0 = I/I_{\text{sat}}$  is the ratio between the incident laser intensity and the saturated intensity, where  $I_{\text{sat}} = 2\pi^2 \hbar c \gamma / 3\lambda^3$ . We can expand the damping force near  $\vec{v} = \vec{0}$  and only keeping the first order,

$$\vec{F}(\vec{v}) \approx \vec{F}(0) - \beta \vec{v}, \quad (3-2)$$

where the value of  $\vec{F}(0)$  is much smaller than the binding force and can be neglected. Here, we obtain the damping coefficient of  $\beta$  in the following form,

$$\beta = \frac{4\hbar |\vec{k}|^2 s_0 \delta / \gamma}{[1 + s_0 + 4\delta^2 / \gamma^2]^2}. \quad (3-3)$$

To achieve the highest cooling rate we need to maximize  $\beta$ . We treat the damping coefficient as a function of detuning  $\delta$  and saturated parameter  $s_0$ ,  $\beta = \beta(\delta, s_0)$ , while other parameters are determined by the features of ion species. We numerically calculate the damping coefficient with different values of  $\delta$  and  $s_0$ , and the results are shown in Fig. 3.4. Obviously, the value of  $\beta$  reaches to its maximum when  $\delta = \gamma/2$  and  $s_0 = 1$ . Therefore, for  $^{171}\text{Yb}^+$ , the optimal parameters for Doppler cooling are  $\delta = 2\pi \times 9.85$  MHz and  $I = I_{\text{sat}} = 51$  mW/cm<sup>2</sup>.

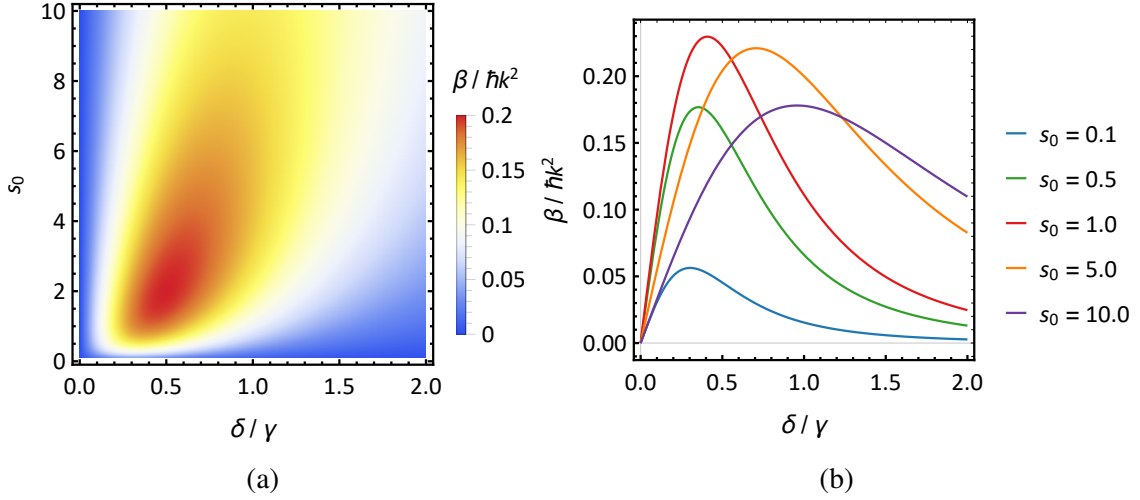


Figure 3.3 Relationship between damping coefficient and values of red-detuning and saturated parameter. When the absorption of the upper  $^2P_{1/2}$  level is not saturated ( $s_0 < 1$ ), the scattering rate  $R_{\text{scatt}}$  increases as the incident laser power increases. However, when the incident power is much larger than the saturated value ( $s_0 > 1$ ), the optimal detuning is further redshifted, and the peak value of the damping coefficient drops due to the power broadening.

Due to fluctuations in the processes of absorption and spontaneous emission, Doppler cooling process can not completely freeze the ion, only cool to a specific minimum temperature, known as the Doppler cooling limit with the form of<sup>[77]</sup>,

$$k_B T_D = \frac{\hbar \gamma}{2}. \quad (3-4)$$

In the case of  $^{171}\text{Yb}^+$ , this limitation is around 473  $\mu\text{K}$ . Several sub-Doppler cooling methods are developed to break this limitation, such as Sisyphus cooling<sup>[78]</sup>, electromagnetically induced transparency (EIT) cooling<sup>[79-81]</sup>, and resolved sideband cooling<sup>[82-83]</sup>. The last one will be introduced later.

In practice we mainly drive the cycle transition of  $^2S_{1/2} |F = 1, m_F = 0, \pm 1\rangle \leftrightarrow ^2P_{1/2} |F = 0\rangle$  for the laser cooling. To cover all the Zeeman levels, the polarization of



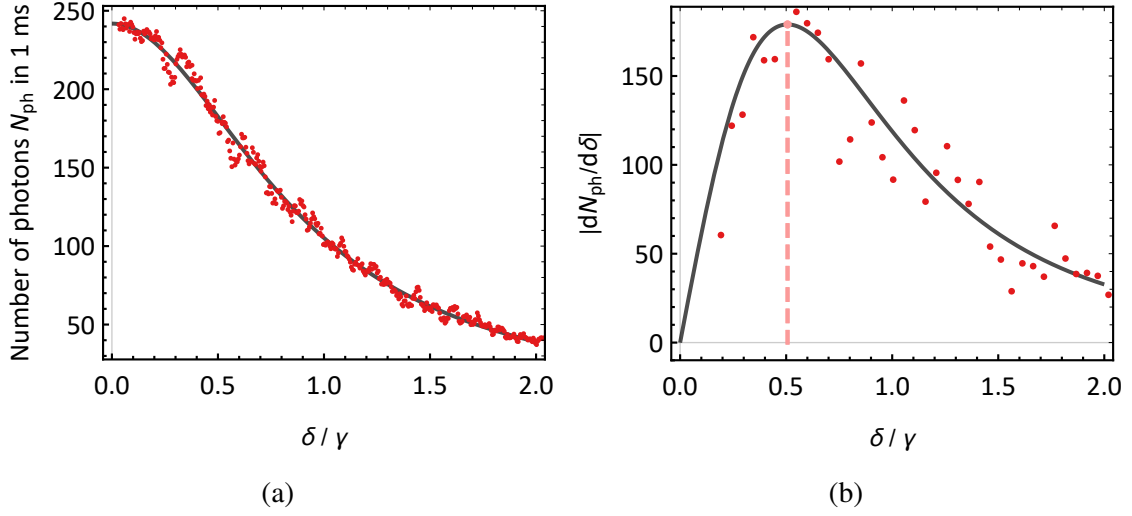


Figure 3.4 Experimental results of the Doppler spectroscopy. (a) The number of the scattering photons  $N_{\text{ph}}$  varies with the value of the detuning  $\delta$ , following the Lorentz line-shape. The red dots are the experimental results, while the solid black line refers to the fitting result. (b) The derivation of the results in (a). The red dots are obtained by numerically calculating the derivation of the smoothed experimental data, and the solid black line is the derivation of the fitting line in (a). For the optimal parameters of the Doppler cooling, the number of the scattering photons is most sensitive to the value of the detuning.

the incident cooling laser should be adjust to contain all the  $\pi$  and  $\sigma^\pm$  components after the quantized axis is determined by the external static magnetic field. Meanwhile, the off-resonate coupling of the cooling laser to the  ${}^2P_{1/2} |F = 1\rangle$  level may lead the ion trapped in the  ${}^2S_{1/2} |F = 0, m_F = 0\rangle$  state, which would stop the cooling process. To solve this problem, an additional 14.7 GHz sideband on the cooling laser is required to cover the cycle transition of  ${}^2S_{1/2} |F = 0, m_F = 0\rangle \leftrightarrow {}^2P_{1/2} |F = 1\rangle$ <sup>[63]</sup>.

### 3.1.2 Qubit state initialization

For any quantum computation or simulation task, the qubit should be deterministically initialized to a pure state. In the trapped-ion platform, this process is achieved through the method of optical pumping.

As shown in Fig. 3.5, the transition from  ${}^2S_{1/2} |F = 1\rangle$  to  ${}^2P_{1/2} |F = 1\rangle$  is driven. The state of the ion has a high probability of decaying to the  $|0\rangle$  state, and then the ion would not get involved in further excitation due to a 12.6 GHz detuning. This fast process can reach at least 99.8% fidelity of initialization within  $5 \mu\text{s}$  for a single ion. In Ref. [14], the error in state initialization is proved to be less than  $10^{-4}$ .

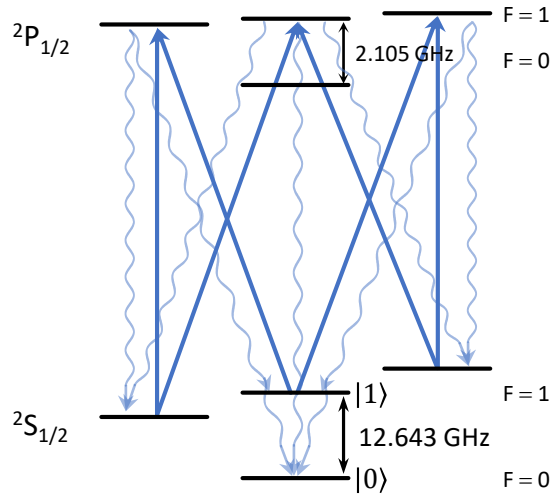


Figure 3.5 Implementation of qubit state initialization through optical pumping.

### 3.1.3 Qubit state detection

The detection process is crucial to obtain the results of quantum tasks or apply quantum error correction. Here, the techniques of state-dependent fluorescence detection is employed for high-fidelity readout<sup>[84]</sup>, as shown in Fig. 3.6. By driving the resonant cycle transition of  ${}^2S_{1/2}|F=1\rangle \leftrightarrow {}^2P_{1/2}|F=0\rangle$ , the ion can scatter many photons when the  $|1\rangle$  state is projected. On the contrary, if the projected state is  $|0\rangle$ , almost no photon would scatter due to a 14.7 GHz detuning for the nearest transition of  ${}^2S_{1/2}|F=0\rangle \leftrightarrow {}^2P_{1/2}|F=1\rangle$  (the transition of  ${}^2S_{1/2}|F=0\rangle \leftrightarrow {}^2P_{1/2}|F=0\rangle$  is dipole-forbidden). Therefore, we could distinguish the projected state by counting the number of scattering photons.

In our system, around 7% of the scattering photons during the detection process is collected by an objective lens with a numerical aperture (N.A.) of 0.61 (Photon Gear)<sup>[67,85]</sup>. The ion is imaged to either an electron-multiplying charge-coupled device (EMCCD) (Andor iXon Ultra 897) or a photomultiplier tube (PMT) (Hamamatsu H10682-210) through a two-step imaging system, as shown in Fig. 3.7. Due to the better performance on the quantum efficiency and the signal-to-noise ratio (SNR), we prefer to use the PMT as the device to count the number of incident photons. For a single ion, to quantify the fidelity of qubit state detection, we prepare the qubit to either the  $|0\rangle$  state or the  $|1\rangle$  state, and then apply the detection laser beam lasting 40  $\mu\text{s}$  and count the collected photons simultaneously. The sequence for each state is repeated 2000 times to obtain a statistical distribution. The histograms of the collected photons for both states are shown in Fig. 3.7.

The statistics of the number of incident photons almost follow the Poisson distribution, with the average photons of 0.05 and 9.58 for the  $|0\rangle$  and  $|1\rangle$  state, respectively. The

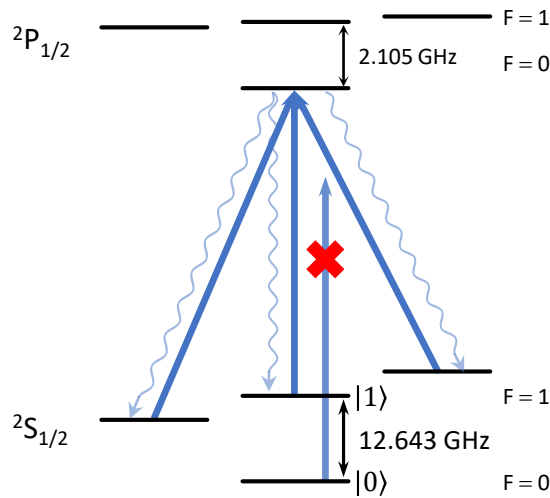


Figure 3.6 Implementation of qubit state detection. If the ion is projected to the  $|1\rangle$  state, the ion would keep scattering photons because it would decay to the  ${}^2S_{1/2}|F = 1\rangle$  levels and then be excited again. On the contrary, once the  $|0\rangle$  state is projected, the ion would be transparent to the detection laser due to the 14.7 GHz detuning to the nearest resonant transition. Therefore, this process results in a high signal-to-noise ratio.

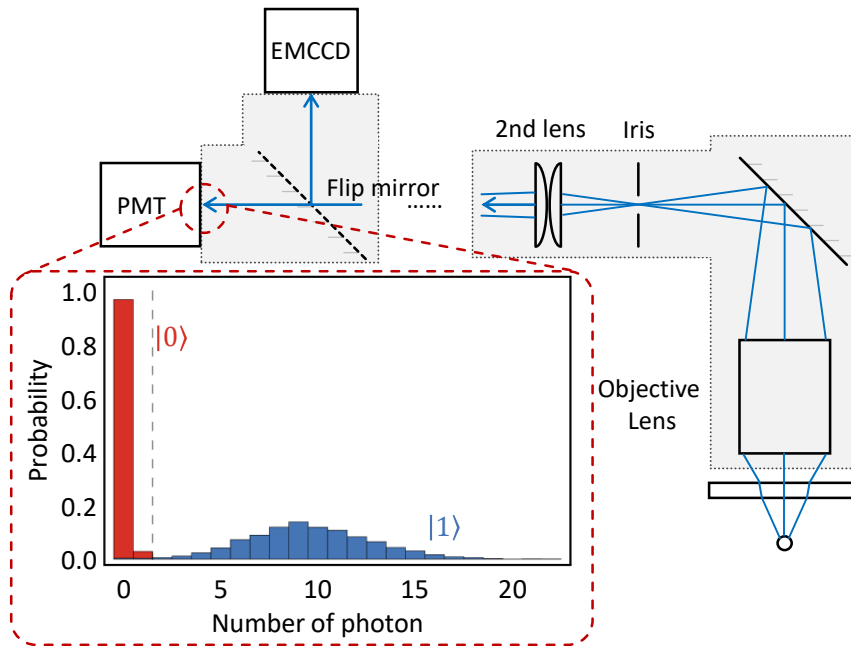


Figure 3.7 Imaging system and photon statistics of different qubit states. The magnification of the whole imaging system is around 91 ( $7\times 13$  for the first objective lens and the second lens, respectively.). The pinhole at the imaging position of the first objective lens serves as a spatial filter. We can control the flip mirror to determine which device would be used. The blue and red histograms in the inset figure shows the statistics of the collected photons for the  $|1\rangle$  and  $|0\rangle$  states, respectively.

well-separated distributions allow us to distinguish the projected state by a fixed threshold. For a single-time measurement (single-shot), we category the projected state to be the  $|1\rangle$  state if the number of collected photons is larger than one. Otherwise, the projected state is treated like the  $|0\rangle$  state. The error rate for a single-time measurement is estimated to be  $2 \times 10^{-3}$  and  $7 \times 10^{-3}$  for the state of  $|0\rangle$  and  $|1\rangle$ , respectively.

One critical error source for detection is the off-resonant coupling to the  ${}^2P_{1/2}|F=1\rangle$  state during the detection process. For the initial  $|1\rangle$  state, this off-resonant coupling can pump the ion to the  $|0\rangle$  state, at a rate of<sup>[67]</sup>,

$$R_{1 \rightarrow 0} \approx \frac{s_0 \gamma}{9} \left( \frac{\gamma}{2 \times 2\pi \times 2.105 \text{ GHz}} \right)^2 \approx (3 \times 10^{-4}) s_0 \mu\text{s}^{-1}. \quad (3-5)$$

Here  $s_0$  is the saturated parameter of the detection beam, and  $2\pi \times 2.105 \text{ GHz}$  is the hyperfine splitting of the  ${}^2P_{1/2}$  manifold. The number of collected photons in a single-time measurement would significantly decrease once the  $|1\rangle$  state is pumped into the  $|0\rangle$  state. The evidence is that in Fig. 3.7, for the initial  $|1\rangle$  state, the probabilities of collecting no photon and single-photon are  $4 \times 10^{-3}$  and  $3 \times 10^{-3}$ , which are much larger than the probabilities of  $7 \times 10^{-5}$  and  $7 \times 10^{-4}$  in the Poisson distribution, respectively. On the contrary, the  $|0\rangle$  state also has a chance to be pumped into the  $|1\rangle$  state, at a rate of<sup>[67]</sup>,

$$R_{0 \rightarrow 1} = \frac{s_0 \gamma}{3} \left( \frac{\gamma}{2 \times 2\pi \times 14.7 \text{ GHz}} \right)^2 \approx (2 \times 10^{-5}) s_0 \mu\text{s}^{-1}, \quad (3-6)$$

which is much smaller than the inverse process due to a much larger detuning.

To suppress errors due to the off-resonant coupling, we should reduce the duration of the detection process while keeping the number of incident photons. The key is to increase the scattering and collecting rate of photons. For the scattering rate, we should optimize the gaps of the Zeeman splittings in  ${}^2S_{1/2}$  state, as well as the power and polarization of the detection laser to destabilize coherent dark states<sup>[86]</sup>. For the collecting rate, we have already used the 0.61 N.A. objective lens to replace the previous 0.21 N.A. one, which increases the solid angle of photon collection by a factor of 10 in theory (a factor of 7 in practice due to the uncompensated optical aberrations). For other options, we can tag the collected photons with their arriving time and utilize timing information to help distinguish the projected state<sup>[67,87]</sup>, and the classical machine learning techniques also have advantages in classifying compared with the fixed threshold method<sup>[87-88]</sup>.

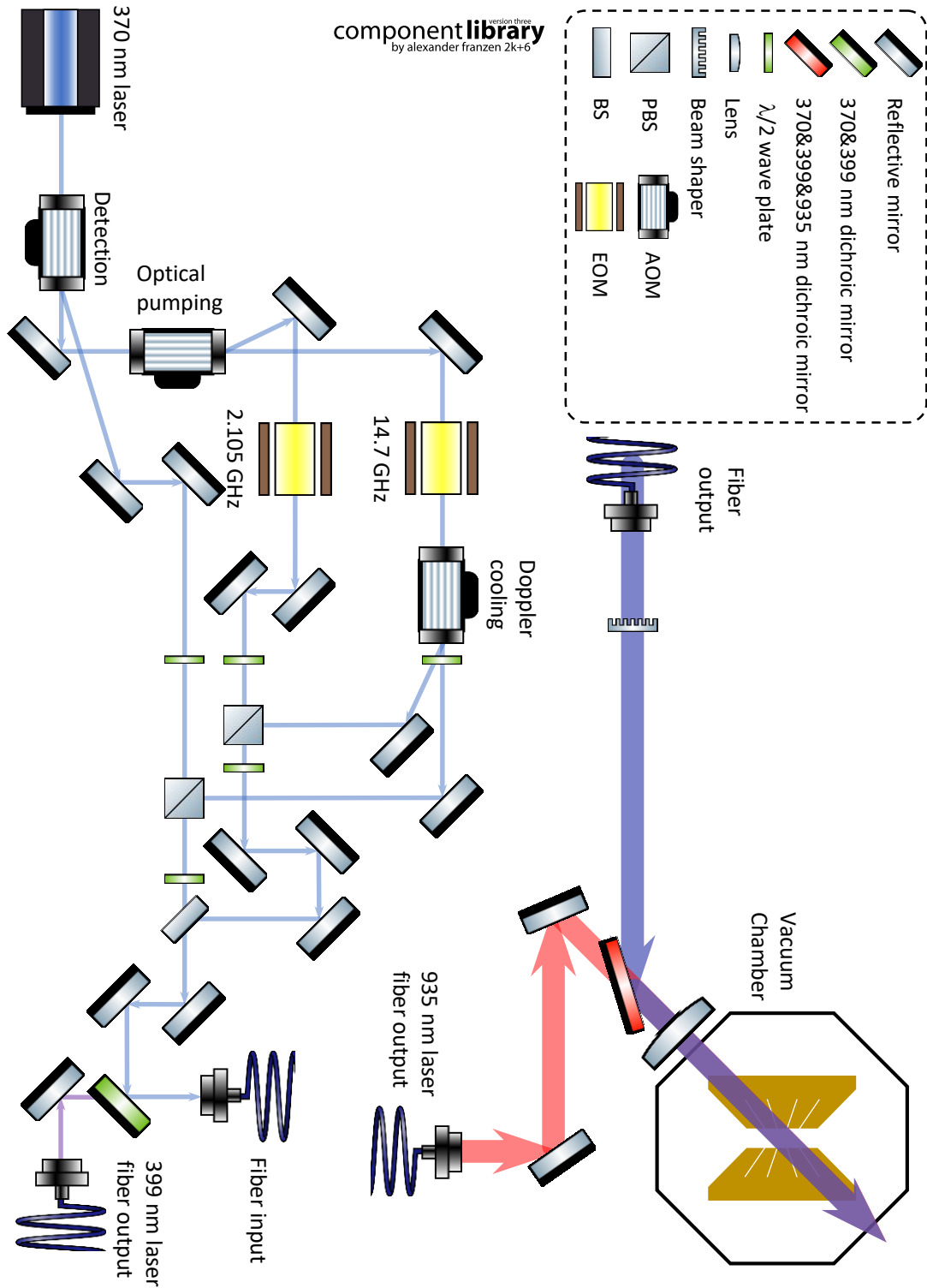


Figure 3.8 Brief schematic diagram of laser alignment. Part of the optical elements are not shown in the figure.

### 3.1.4 Alignment of lasers

In Fig. 3.8, we briefly summarize the alignment of the 369.526, 398.911 and 935.188 nm lasers. The 369.526 nm laser is generated by a 739.052 nm laser diode through the second-harmonic generation (SHG) (Toptica TA-SHG pro). Therefore, we indirectly stabilize the frequency of the 369.526 nm laser by locking the frequency of the 739.052 nm laser to a homemade optical cavity and the saturated absorption spectra of the iodine molecules<sup>[63]</sup>. The 369.526 nm laser beam first passes an acousto-optic modulator (AOM) (Brimrose QZF-210-40), resulting in a 220 MHz frequency shift in the +1st order diffractive beam which resonates to the transition  $^2S_{1/2}|F = 1\rangle \leftrightarrow ^2P_{1/2}|F = 0\rangle$  and works as the detection beam. The 0th order beam goes through the second AOM (Brimrose QZF-210-40), which also provides a 220 MHz frequency shift in the +1st order. This +1st order beam continues to pass an electro-optic modulator (EOM) (New focus 4431) then obtain a 2.105 GHz sideband. One of the sideband-frequencies resonates to the transition of  $^2S_{1/2}|F = 1\rangle \leftrightarrow ^2P_{1/2}|F = 1\rangle$ , working for the optical pumping process. Finally, the remained 0th order sequentially passes an EOM (Qubig EO-WG14.7M2, which has 75% transmission rate and can reach 1% strength on the 14.7 GHz sidebands with only 1 W input power) and an AOM (Brimrose QZF-200-100), which are driven at the frequencies of 14.7 GHz and 210 MHz, respectively. The +1st order diffractive beam of the last AOM is 10 MHz red-detuned from the transition of  $^2S_{1/2}|F = 1\rangle \leftrightarrow ^2P_{1/2}|F = 0\rangle$  and has the 14.7 GHz sideband, working for the optimal Doppler cooling. The 0th order beam of the last AOM is used for the ionization process and is also capable of cooling the ions with higher speed, called the "strong beam". Note that the AOMs here are not only utilized as the frequency shifters but also work as the fast optical switches.

After separating the 369 nm laser into several beams for detection, optical pumping, Doppler cooling and ionization, they are combined again through two polarizing beam splitters (PBS) and one beam splitter (BS). All the 369 nm beams are coupled to a single-mode fiber (Thorlabs P3-305A-FC) to modularize the previous laser path. The 398.911 nm laser beam (Toptica DL pro) also goes into the fiber with the help of a customized dichroic mirror. After the fiber, the combined beams pass a diffractive optical element (DOE) (HOLO/OR). The 935.188 nm laser beam (Toptica DL pro), after gains a 3.105 GHz sideband through a fiber-EOM (EOspace), would be combined through another dichroic mirror, and then all the beams are focused at the trap center with a proper lens. The DOE here modulates the phase of the 369 nm beams which would form a  $60 \mu\text{m} \times 180 \mu\text{m}$

rectangular shape at the ion-position after focused by the final lens.

## 3.2 Coherent operations on a single qubit

After initializing the qubit to the  $|0\rangle$  state, coherent operations are required to perform any quantum algorithm or quantum simulation. To drive the hyperfine qubit with a 12.6 GHz energy splitting, we can utilize either magnetic fields oscillating at the resonant microwave frequency<sup>[63]</sup> or two-photon stimulated Raman transitions<sup>[89]</sup>. Both methods are introduced as follows.

### 3.2.1 Microwave induced magnetic dipole transition

#### **Hamiltonian in dressed-state picture**

Generally speaking, the Hamiltonian of the ion qubit driven by a microwave magnetic field can be written as ( $\hbar = 1$  always),

$$H = \frac{\omega_q}{2}\sigma_z + \Omega \cos(\vec{k} \cdot \vec{r} - \omega t + \phi)\sigma_x. \quad (3-7)$$

The first term describes the reduced Hilbert space of the qubit system with an energy splitting of  $\omega_q$ , while the second term originates from the magnetic dipole interaction, where the magnetic field oscillates at a frequency  $\omega$  with an initial phase  $\phi$ . The Rabi frequency of  $\Omega$  quantifies the strength of dipole interaction. The notations of  $\sigma_i$  here refer to the Pauli matrices defined in the qubit system. The spatial term,  $\vec{k} \cdot \vec{r}$ , can be neglected due to a small value of  $|\vec{k}| \approx 3 \times 10^{-4} \mu\text{m}^{-1}$  when  $\omega$  is around 12.6 GHz. By choosing the free Hamiltonian of  $H_0 = \omega\sigma_z/2$ , we transfer the free-frame Hamiltonian into the dressed-state picture,

$$\begin{aligned} H_I &= e^{iH_0 t}(H - H_0)e^{-iH_0 t} \\ &= -\frac{\mu}{2}\sigma_z + \frac{\Omega}{2}(\sigma_+ e^{i\omega t} + \sigma_- e^{-i\omega t})(e^{i(\omega t - \phi_0)} + e^{-i(\omega t - \phi_0)}) \\ &\approx -\frac{\mu}{2}\sigma_z + \frac{\Omega}{2}(\sigma_+ e^{i\phi} + \sigma_- e^{-i\phi}) \\ &= -\frac{\mu}{2}\sigma_z + \frac{\Omega \cos \phi}{2}\sigma_x + \frac{\Omega \sin \phi}{2}\sigma_y, \end{aligned} \quad (3-8)$$

where  $\mu = \omega - \omega_q$  is the energy difference between the qubit and a single microwave photon, and the last line is obtained after the rotating wave approximation (RWA) by neglecting the terms oscillating at the frequency of  $2\omega$ . The advantage of the dressed-

state picture is that the final Hamiltonian can be time-independent, and the amplitude along each Pauli matrix is fully determined by the parameters of the applied microwave.

For an initial state of  $|\psi(0)\rangle = c_0(0)|0\rangle + c_1(0)|1\rangle$  where  $|c_0(0)|^2 + |c_1(0)|^2 = 1$ , its time evolution is governed by the evolution operator  $U(t)$ ,

$$|\psi(t)\rangle = U(t)|\psi(0)\rangle = \exp(-iH_1 t) |\psi(0)\rangle. \quad (3-9)$$

This evolution can be analytically solved, and the complex amplitudes are given as follows if we set  $|\psi(0)\rangle = |0\rangle$  for convenience,

$$c_1(t) = -i \frac{\Omega}{\Omega_{\text{eff}}} e^{i\phi} \sin \frac{\Omega_{\text{eff}} t}{2}, \quad (3-10)$$

$$c_0(t) = \cos \frac{\Omega_{\text{eff}} t}{2} - i \frac{\mu}{\Omega_{\text{eff}}} \sin \frac{\Omega_{\text{eff}} t}{2}, \quad (3-11)$$

where  $\Omega_{\text{eff}} = \sqrt{\Omega^2 + \mu^2}$  is the effective Rabi frequency<sup>[77]</sup>. The population occupied in the  $|1\rangle$  state,  $p_1(t) = |c_1(t)|^2$ , reaches its maximum value  $\Omega^2/(\Omega^2 + \mu^2)$  for the first time at  $t = \pi/\Omega_{\text{eff}}$ . The Rabi oscillations with different detunings  $\mu$  are shown in Fig. 3.9.

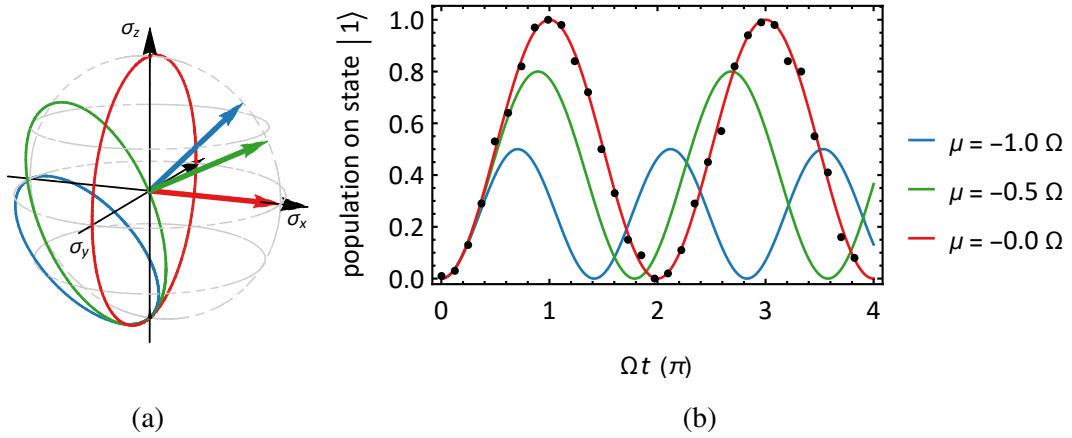


Figure 3.9 State evolutions under different detunings. (a) Representation of the state evolutions on the Bloch sphere. According to the optical Bloch equation of the two-level system,  $\dot{\vec{r}} = \vec{r} \times \vec{Q}$ , the state vector  $\vec{r} = \{2\text{Re}[c_1 c_0^*], 2\text{Im}[c_1 c_0^*], |c_1|^2 - |c_0|^2\}$ , precesses along the effective field  $\vec{Q} = \{\Omega \cos \phi, \Omega \sin \phi, -\mu\}$ . The normalized effective fields for different detunings of  $\mu$  are shown in colored arrows, while circles with the same color on the Bloch sphere represent the corresponding state evolutions. (b) Rabi oscillations. As the detuning increases, the oscillation becomes faster while the contrast keeps dropping. The black dots indicate the experimental results under the resonant condition.

For quantum computation, we always set  $\mu \approx 0$  to realize arbitrary single-qubit

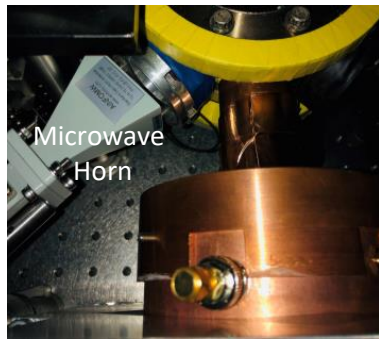


rotations,

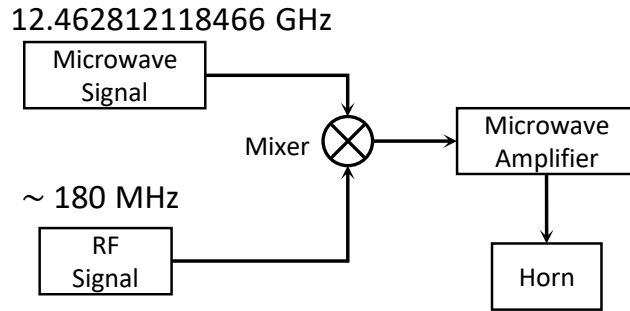
$$R_\phi(\theta) = U\left(\frac{\theta}{\Omega}, \phi\right) = \exp\left[-i\frac{\theta}{2}\sigma_\phi\right], \quad (3-12)$$

where  $\sigma_\phi = \sigma_x \cos \phi + \sigma_y \sin \phi$ . For the initial  $|0\rangle$  ( $|1\rangle$ ) state, the population can be fully transferred to the  $|1\rangle$  ( $|0\rangle$ ) state at  $\theta = \pi$  or equivalently  $t = \pi/\Omega$ . This kind of operation  $R_\phi(\pi)$ , which called as the  $\pi$ -rotation along the  $\phi$  axis, is similar to the NOT gate in classical computation. Moreover, we can define the  $\pi/2$ -rotation along the  $\phi$  axis,  $R_\phi(\pi/2)$ , by setting  $\theta$  to be  $\pi/2$ , which can be utilized to prepare the superposition state of the  $|0\rangle$  and  $|1\rangle$  states with equal populations.

In the experimental realization, the microwave magnetic field is emitted from a microwave horn near a viewport of the vacuum chamber, as shown in Fig. 3.10 (a). The injected microwave signal to the horn is generated by mixing a 12.462812118466 GHz microwave signal (generated from ROHDE&SCHWARZ SMB 100A) and a RF signal around 180 MHz, as illustrated in Fig. 3.10 (b). This RF signal can be produced by either a direct digital synthesizer (DDS) (Analog AD9910) or an arbitrary wave generator (AWG) (SPECTRUM DN2.662-08), depending on applications. By tuning the frequency, amplitude, and phase of the RF signal, the parameters of the microwave magnetic field can be well controlled.



(a)



(b)

Figure 3.10 Generation of microwave magnetic field. (a) Microwave horn used in the experiment. (b) Generation of the microwave signal. The 12.6 GHz microwave signal is generated by mixing a 12.4 GHz signal with a 180 MHz signal and then amplified. Compared with the signal in the microwave range, the RF signal can be controlled more precisely.

### Coherence measurement

Now we can utilize coherent operations driven by the microwave magnetic fields to characterize our ion qubit. One of the most important parameters is the coherence time of the qubit, which can be extracted through a Ramsey-type method. In the experiment, after qubit state initialization, we first apply a  $\pi/2$ -rotation  $R_\phi(\pi/2)$  to prepare the equal-populated superposition state  $(|0\rangle + e^{-i\phi}|1\rangle)/\sqrt{2}$ . After that, we wait for a duration of  $\tau$ , and then apply the second  $\pi/2$ -rotation  $R_{\phi+\pi\tau/\tau_0}(\pi/2)$  to recover the state, as shown in Fig. 3.11 (a). Here  $\tau_0$  is a preset constant. Ideally, the probability of projecting the final state to the  $|1\rangle$  state should oscillate with the delay time  $\tau$ ,

$$p_1(\tau) = \frac{1}{2} \left( 1 + \cos \left[ \left( \mu + \frac{\pi}{\tau_0} \right) \tau \right] \right), \quad (3-13)$$

where the constant  $\tau_0$  determines the oscillating period. The value of  $\mu$  should be small because we tend to drive the transition resonantly, but can not be ignored when  $\tau$  is long. However, due to noisy environments, decoherence is inevitable, causing the pure state to decay into a mixed state. Mathematically, decoherence can be quantified as the decay in off-diagonal terms if we describe the quantum state in its density matrix form,

$$\begin{aligned} \rho &= |0\rangle\langle 0| + |1\rangle\langle 1| + e^{i\phi}|0\rangle\langle 1| + e^{-i\phi}|1\rangle\langle 0| \\ &\rightarrow |0\rangle\langle 0| + |1\rangle\langle 1| + e^{i\phi}f(\tau)|0\rangle\langle 1| + e^{-i\phi}f(\tau)|1\rangle\langle 0|, \end{aligned} \quad (3-14)$$

where  $f(\tau)$  is the decay profile. Therefore, Eq. (3-13) should be modified to include decoherence, which turns out to be,

$$p_1(\tau) = \frac{1}{2} \left( 1 + f(\tau) \cos \left[ \left( \mu + \frac{\pi}{\tau_0} \right) \tau \right] \right). \quad (3-15)$$

In the experiment, the decay profile can be exponential form  $f(\tau) = e^{-\tau/\tau_c}$  or Gaussian form  $f(\tau) = e^{-\tau^2/\tau_c^2}$ , depending on the feature of the noise spectrum. The coherence time  $\tau_c$  is defined as the time when the oscillating contrast drops to  $e^{-1} \approx 0.37$ . The experimental decay of the Ramsey oscillation measured by using the microwave is shown in Fig. 3.11. Note that the stability of the relative phase between the two  $\pi/2$ -rotations would also affect the final state. Therefore, the coherence time of the qubit can not be properly characterized when it exceeds the phase-correlated time of the microwave magnetic field.

Although the microwave method has the advantages of high-stability and simple-controllability, it lacks scalability due to the long wavelength, which is much larger than

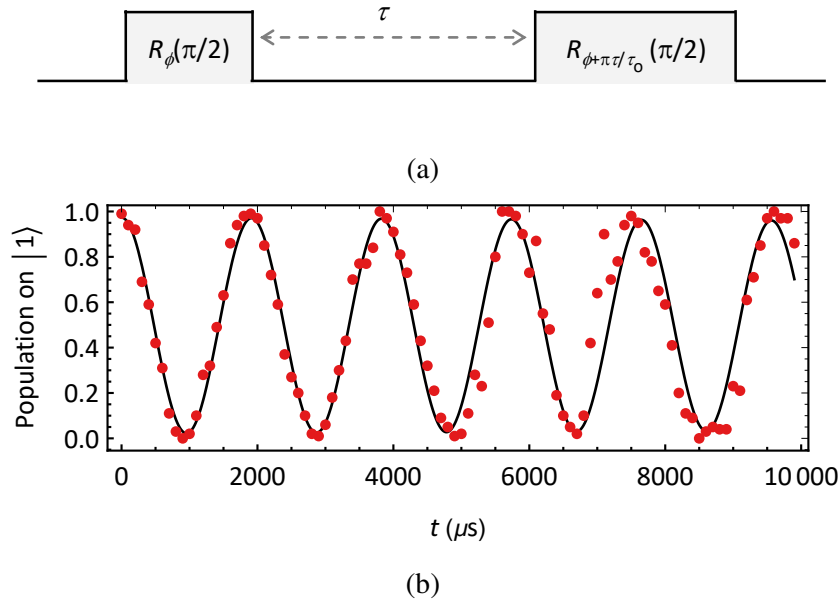


Figure 3.11 Measurement of qubit coherence time. (a) Ramsey-type method. The decay of coherence during the delay  $\tau$  can be characterized by being sandwiched by two  $\pi/2$ -rotations with a proper phase difference. Here we assume that the duration of rotations can be ignored. (b) Coherence time measured in the experiment by using the microwave magnetic field. No significant decay of the Ramsey oscillation is observed after 10 ms.

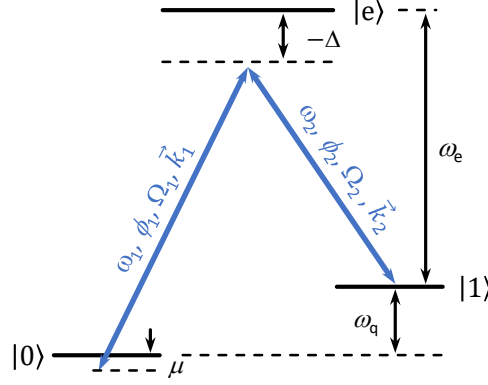
the length of a ion-chain. We can only globally manipulate all the qubits without individual controllability. In principle, we can additionally introduce a gradient on the external static magnetic field<sup>[65]</sup>, or use the gradient of a near-field microwave<sup>[90]</sup>. However, the previous method discards the homogeneity between different ion qubits, while the latter one has extreme complexity in designing large-scale microwave circuits. Despite these shortages, the microwave is still the most convenient tool to troubleshoot fundamental problems of the experimental system.

### 3.2.2 Stimulated Raman transition

#### Effective Hamiltonian

Compared with the microwave magnetic field, the optical laser can be spatially focused due to a much shorter wavelength. To drive the hyperfine qubit with a microwave frequency splitting, we employ the two-photon stimulated Raman transition, and a schematic diagram is illustrated in Fig. 3.12.

By simultaneously driving the electric dipole transitions from the  $|0\rangle$  and  $|1\rangle$  states


 Figure 3.12  $\Lambda$ -type two-photon Raman transition.

to an intermediate level  $|e\rangle$ , as shown in Fig. 3.12, the Hamiltonian of the whole system in the free frame can be written as,

$$\begin{aligned}
 H = & \frac{\omega_q}{2}\sigma_z + \left(\omega_e + \frac{\omega_q}{2}\right)|e\rangle\langle e| \\
 & + \frac{\Omega_1}{2}(|e\rangle\langle 0| + |e\rangle\langle 1| + \text{h.c.})(e^{i(\vec{k}_1 \cdot \vec{r} - \omega_1 t + \phi_1)} + \text{h.c.}) \\
 & + \frac{\Omega_2}{2}(|e\rangle\langle 0| + |e\rangle\langle 1| + \text{h.c.})(e^{i(\vec{k}_2 \cdot \vec{r} - \omega_2 t + \phi_2)} + \text{h.c.}), \quad (3-16)
 \end{aligned}$$

where  $\Omega_i$ ,  $\vec{k}_i$  and  $\phi_i$  are the dipole coupling strength, wave vector and optical phase of the  $i$ -th Raman laser, respectively, and h.c. represents Hermitian conjugation. By choosing the rotating frame with respect to  $H_0 = \omega_q\sigma_z/2 + (\omega_e + \omega_q/2)|e\rangle\langle e|$ , the interaction Hamiltonian turns out to be,

$$\begin{aligned}
 H = & \left( \frac{\Omega_1}{2} e^{i(-\Delta - \mu)t} e^{i(\vec{k}_1 \cdot \vec{r} + \phi_1)} + \frac{\Omega_2}{2} e^{i(-\Delta + \omega_q)t} e^{i(\vec{k}_2 \cdot \vec{r} + \phi_2)} \right) |e\rangle\langle 0| \\
 & \left( \frac{\Omega_1}{2} e^{i(-\Delta - \mu - \omega_q)t} e^{i(\vec{k}_1 \cdot \vec{r} + \phi_1)} + \frac{\Omega_2}{2} e^{i(-\Delta)t} e^{i(\vec{k}_2 \cdot \vec{r} + \phi_2)} \right) |e\rangle\langle 1| + \text{h.c.}, \quad (3-17)
 \end{aligned}$$

where the detunings  $-\Delta$  and  $\mu$  are shown in Fig. 3.12. Here, we use the relations of  $\omega_1 = \omega_e + \omega_q + \mu - (-\Delta)$  and  $\omega_2 = \omega_e - (-\Delta)$  to simplify Fig. 3-17. Under the assumption of  $|\Delta| \gg \Omega_1, \Omega_2$  and  $|\Delta| \gg \omega_q \gg \mu$ , the intermediate level  $|e\rangle$  can be adiabatically eliminated, yielding an effective Hamiltonian in the qubit system<sup>[91]</sup>,

$$H_{\text{eff}} = \frac{\delta_{\text{diff}}}{2}\sigma_z + \frac{\Omega}{2} \left( \sigma_+ e^{i(\vec{k} \cdot \vec{r} - \mu t + \phi)} + \sigma_- e^{-i(\vec{k} \cdot \vec{r} - \mu t + \phi)} \right), \quad (3-18)$$

where  $\Omega = \Omega_1\Omega_2/(2\Delta)$ ,  $\vec{k} = \vec{k}_1 - \vec{k}_2$  and  $\phi = \phi_1 - \phi_2$  are the effective Rabi frequency, effective wave vector and relative optical phase, respectively.  $\delta_{\text{diff}}$  in the above equation

has a form of,

$$\begin{aligned}\delta_{\text{diff}} &= -\left(\frac{\Omega_1^2}{4(-\Delta - \mu - \omega_q)} + \frac{\Omega_2^2}{4(-\Delta)}\right) + \left(\frac{\Omega_1^2}{4(-\Delta + \mu)} + \frac{\Omega_2^2}{4(-\Delta + \omega_q)}\right) \\ &\approx -\frac{\Omega_1^2 + \Omega_2^2}{4\Delta} \frac{\omega_q}{\Delta},\end{aligned}\quad (3-19)$$

which is the differential light shift in the energy levels of the qubit and is pretty small due to  $\omega_q/|\Delta| \sim 10^{-3} \ll 1$  in our setup. This term can be absorbed by changing the frequency of the rotating frame from  $\omega_q\sigma_z$  to  $(\omega_q + \delta_{\text{diff}})\sigma_z$ , which is ignored in the latter discussion. The effective Hamiltonian here has no difference from the resonant case of Eq. (3-8) if we take  $\vec{k}_1 = \vec{k}_2$  and  $\mu = \delta_{\text{diff}} \approx 0$ . Therefore, we can also utilize the two-photon Raman transition to achieve the arbitrary single-qubit rotations.

### Single-qubit rotation and qubit-motion coupling

However, the value of the effective wave vector  $|\vec{k}|$  can vary from 0 (co-propagating) to  $4\pi/\lambda$  (counter-propagating) by changing the angle of the propagating Raman beams. The maximum value of  $|\vec{k}|$  can reach around  $10 \mu\text{m}^{-1}$  because  $\lambda$  falls into the range of optical wavelength, which provides a probability of ion-motion coupling. By treating the ion as a quantized harmonic oscillator which vibrates at the frequency of  $\nu$ , the Hamiltonian in Eq. (3-18) should be revised as,

$$H_{\text{eff}} = \nu a^\dagger a + \frac{\Omega}{2} \left( \sigma_+ e^{i(\eta(a+a^\dagger) - \mu t + \phi)} + \text{h.c.} \right). \quad (3-20)$$

Here we simplify the problem by only considering one dimensional motion ( $\vec{r} = x$ ). Therefore,  $a$  and  $a^\dagger$  are the creation and annihilation operators, respectively, and  $k \cdot x$  is equal to  $k\Delta x(a + a^\dagger) = \eta(a + a^\dagger)$  where  $\Delta x = \sqrt{\hbar/2M\nu}$  is the size of the ground state wave function and  $\eta = k\Delta x$  is known as the Lamb-Dicke parameter. By choosing a new rotation frame with respect to  $H_0 = \nu a^\dagger a$  and then expanding  $\exp(i\vec{k} \cdot \vec{r})$  to the first order, we obtain the approximated interaction Hamiltonian,

$$H_1 \approx \frac{\Omega}{2} \left[ \sigma_+ (1 + i\eta a e^{-i\nu t} + i\eta a^\dagger e^{i\nu t}) e^{-i\mu t + i\phi} + \text{h.c.} \right]. \quad (3-21)$$

This approximation only establishes when  $\eta\sqrt{\langle (a + a^\dagger)^2 \rangle} \ll 1$ , known as the Lamb-Dicke approximation, where  $\langle \cdot \rangle$  denotes the averaging over the quantum state. In the experiment, we always require  $\eta \ll 1$ ; otherwise, high order transitions would appear. By tuning the

value of  $\mu$  to be around 0,  $-\nu$ , and  $\nu$ , we can obtain three types of transitions,

$$H_{\text{car}} = \frac{\Omega}{2}(\sigma_+ e^{i\phi} + \text{h.c.}), \quad (3-22)$$

$$H_{\text{rsb}} = \frac{i\eta\Omega}{2}(\sigma_+ a e^{i\phi} - \text{h.c.}), \quad (3-23)$$

$$H_{\text{bsb}} = \frac{i\eta\Omega}{2}(\sigma_+ a^\dagger e^{i\phi} - \text{h.c.}), \quad (3-24)$$

known as carrier, red-sideband and blue-sideband transitions, respectively, as shown in Fig. 3.13. Similarly, the carrier transition described in Eq. (3-22) can be utilized to implement the arbitrary single-qubit rotations of  $R_\phi(\theta)$ . The Hamiltonian of the red or blue sideband transition, known as the Jaynes-Cummings or anti-Jaynes-Cummings model respectively, couples the qubit to its external quantized motion, which is crucial in entangling multiple ion qubits.

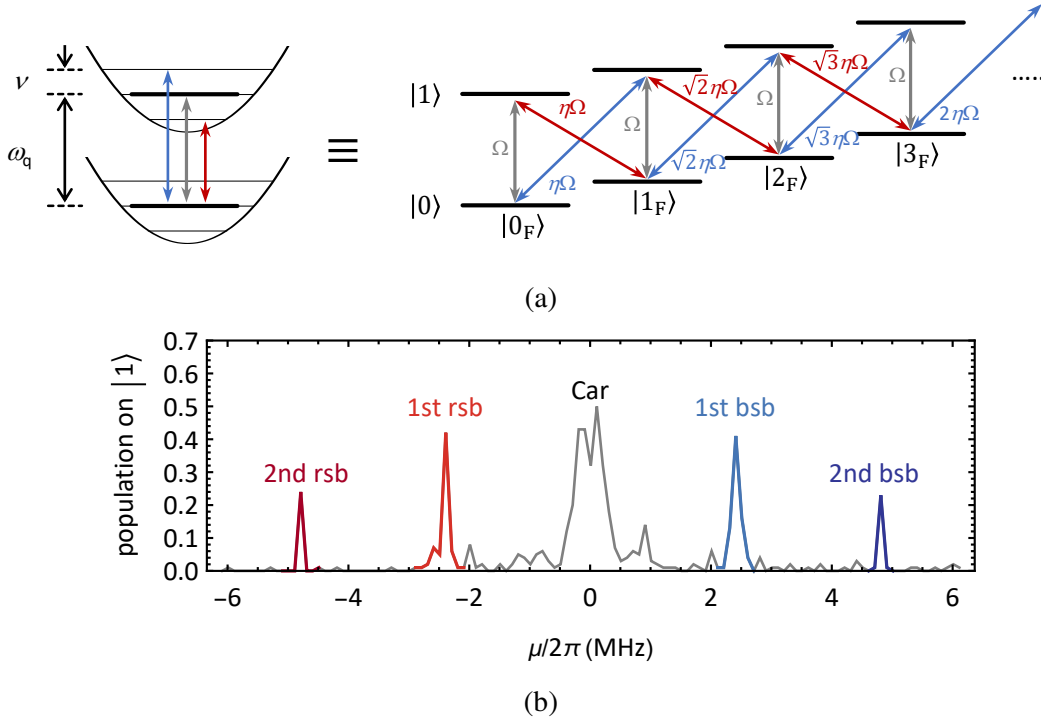


Figure 3.13 Carrier and sideband transitions. (a) Hilbert space including the qubit and its quantized harmonic oscillation.  $|n_F\rangle$  represents the Fock-state basis of the harmonic oscillator. Gray arrows refer to the carrier transition ( $|0\rangle |n_F\rangle \leftrightarrow |1\rangle |n_F\rangle$ ), while red and blue arrows refer to the red sideband ( $|0\rangle |n_F\rangle \leftrightarrow |1\rangle |n_F - 1\rangle$ ) and the blue sideband ( $|0\rangle |n_F\rangle \leftrightarrow |1\rangle |n_F + 1\rangle$ ), respectively. The Rabi frequency of the sideband transitions has a factor of  $\sqrt{n_F}$  for the different  $|n_F\rangle$  states. (b) Raman spectrum measured in the experiment. Note that the second order sideband transitions occur due to a large average phonon number of  $\bar{n}_F = \langle a^\dagger a \rangle$  after Doppler cooling.

### Sideband cooling

The sideband transitions enable us to manipulate a much vaster Hilbert space. One crucial function is that we can combine the red-sideband transition together with the optical pumping process to further cool the ion to its motional ground state, called sideband cooling. The brief principle of sideband cooling is shown in Fig. 3.14. Here we alternately apply the  $\pi$ -rotation of the red-sideband transition ( $\eta\Omega t \approx \pi$ ) and the optical pumping, and then all the population would be accumulated in the  $|0\rangle|0_F\rangle$  state finally. The cooling rate is almost determined by the coupling strength of the red-sideband transition ( $\eta\Omega$ ), because the duration of optical pumping can be neglected compared with that of the sideband transition. Typically, the cooling rate can achieve around  $10^2 \sim 10^3$  phonons/ms, and the final temperature can reach hundreds of nK. The limitation in the final temperature is due to the heating effect from the detuned blue sideband transition and electric noises in the surrounding environment.

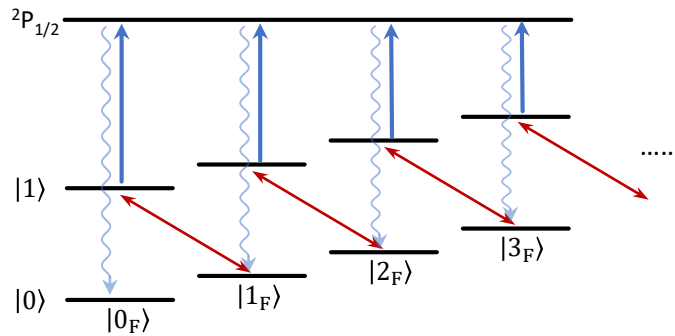


Figure 3.14 Implementation of sideband cooling. The  $|0\rangle|0_F\rangle$  is a dark state for the red sideband transition and the optical pumping, and finally, most of the state population would be transferred to this state.

### Raman transition driven by pulsed laser

In the above sections, we consider using two beams with continuous wavelength (CW) to drive the stimulated Raman transition. However, it is challenging in the experiment since the phases of the two beams must be strictly correlated. To achieve this requirement, we can separate two Raman beams from the same laser, and then shift a frequency by 12.6 GHz on one of the beams. However, either AOMs or EOMs have pretty low efficiency of shifting such a considerable frequency.

Instead, we employ a pulsed laser to drive the Raman transitions, because it naturally

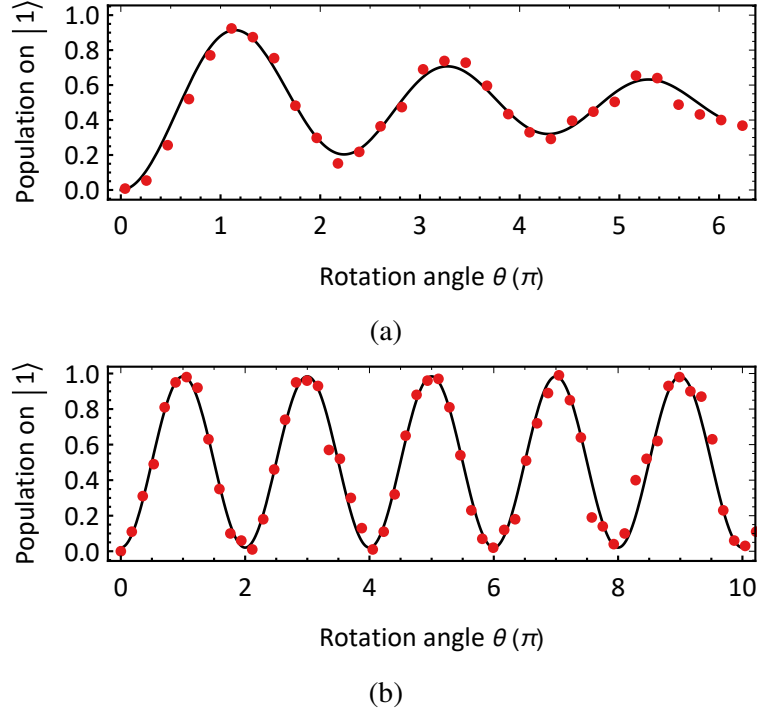


Figure 3.15 Rabi oscillation of carrier transition. (a) The average phonon number  $\bar{n}$  is around 5 after Doppler cooling, and then the high-order transitions which neglected in the Lamb-Dicke approximation would significantly modify the Rabi frequency of the carrier and make it depend on the phonon state<sup>[41]</sup>. This effect results in a fast decay in the Rabi oscillation. (b) After sideband cooling, the average phonon number drops to around 0.02, and the Lamb-Dicke approximation is well established. The Rabi oscillation with a full contrast can be observed.

has discrete combs in the frequency domain<sup>[92]</sup>. Mathematically, when the duration of the laser-ion interaction is much longer than the inverse of the repetition rate  $\omega_{\text{rep}}^{-1}$ , the laser pulses can be decomposed into multi-frequency electric fields oscillating in phase,

$$\vec{E}(t) = \sum_l \vec{E}_l \exp \left[ i \left( \vec{k}_c \cdot \vec{r} - (\omega_c + l\omega_{\text{rep}})t + \phi \right) \right]. \quad (3-25)$$

Here  $\vec{k}_n \approx \vec{k}_c = 2\pi\omega_c/c$  which ignore the tiny difference in the values of wave vectors,  $\omega_c$  is the center frequency, and  $\phi$  is the common phase. To get a non-zero effective wave vector, we separate the pulsed laser into two beams and then hit the ion in different directions. Additionally, we use two AOMs to shift each beam by frequencies of  $\omega_{\text{AOM}}^{(1)}$  and  $\omega_{\text{AOM}}^{(2)}$ , respectively. In this case, we revise the interaction Hamiltonian in Eq. (3-17)



to include the multiple frequency combs,

$$H_I = \sum_{j=1}^2 \sum_{l=-\infty}^{\infty} \frac{g_l^{(j)}}{2} \left[ |e\rangle\langle 0| e^{i(-\Delta + \omega_q - \omega_{\text{AOM}}^{(j)} - l\omega_{\text{rep}})t} + |e\rangle\langle 1| e^{i(-\Delta - \omega_{\text{AOM}}^{(j)} - l\omega_{\text{rep}})t} \right] e^{i(\vec{k}_c^{(j)} \cdot \vec{r} + \phi_i)} + \text{h.c.}, \quad (3-26)$$

where  $g_l^{(j)}$  is the coupling strength of the  $l$ -th frequency comb in the  $j$ -th beam, and we assume that  $\omega_c + (-\Delta) = \omega_e$ . To realize the resonant Raman transition, we should make sure that the frequency difference of the two combs from two Raman beams matches the energy gap of the qubit, as shown in Fig. 3.16, indicating that one of the following equations should be satisfied,

$$-\Delta + \omega_q - \omega_{\text{AOM}}^{(1)} - l_1\omega_{\text{rep}} = -\Delta - \omega_{\text{AOM}}^{(2)} - l_2\omega_{\text{rep}}, \quad (3-27)$$

$$-\Delta + \omega_q - \omega_{\text{AOM}}^{(2)} - l_2\omega_{\text{rep}} = -\Delta - \omega_{\text{AOM}}^{(1)} - l_1\omega_{\text{rep}}, \quad (3-28)$$

where  $l_1$  and  $l_2$  is the  $l_1$ -th and  $l_2$ -th comb from the first and second Raman beams, respectively. By simplifying the above equations, the values of  $\omega_q$ ,  $\omega_{\text{AOM}}^{(j)}$  and  $\omega_{\text{rep}}$  should satisfy,

$$\omega_q - (\omega_{\text{AOM},r}^{(1)} - \omega_{\text{AOM},r}^{(2)}) = (l_1 - l_2)\omega_{\text{rep}}, \quad (3-29)$$

or

$$\omega_q + (\omega_{\text{AOM},r}^{(1)} - \omega_{\text{AOM},r}^{(2)}) = (l_2 - l_1)\omega_{\text{rep}}. \quad (3-30)$$

Here  $\omega_{\text{AOM},r}^{(j)}$  is the value of  $\omega_{\text{AOM}}^{(j)}$  which satisfies the resonant conditions.

Without loss of generality, we first assume that  $\Delta_{\text{AOM}} = \omega_{\text{AOM},r}^{(1)} - \omega_{\text{AOM},r}^{(2)} > 0$  and the condition of Eq. (3-30) is satisfied, as shown in Fig. 3.16. In practice, we always set  $\omega_{\text{AOM}}^{(2)} = \omega_{\text{AOM},r}^{(2)}$ , while  $\omega_{\text{AOM}}^{(1)} = \omega_{\text{AOM},r}^{(1)} + \mu$  is slightly detuned from the resonant condition ( $\mu \ll \omega_{\text{rep}}$ ). Note that all the comb-pairs with the same difference of  $\Delta l = (\omega_q + \Delta_{\text{AOM}})/\omega_{\text{rep}}$  can coherently drive the Raman transition; therefore, the final effective Hamiltonian turns out to be,

$$H_{\text{eff}} = \frac{\Omega}{2} \left( \sigma_- e^{i\mu t} e^{-i(\vec{k} \cdot \vec{r} + \phi)} + \text{h.c.} \right), \quad (3-31)$$

where  $\Omega = \sum_{l_2} g_{l_2+\Delta l}^{(1)} g_{l_2}^{(2)} / (2\Delta)$ ,  $\vec{k} = \vec{k}_c^{(1)} - \vec{k}_c^{(2)}$  and  $\phi = \phi_1 - \phi_2$  are the effective Rabi frequency, effective wave vector and relative optical phase, respectively. The differential

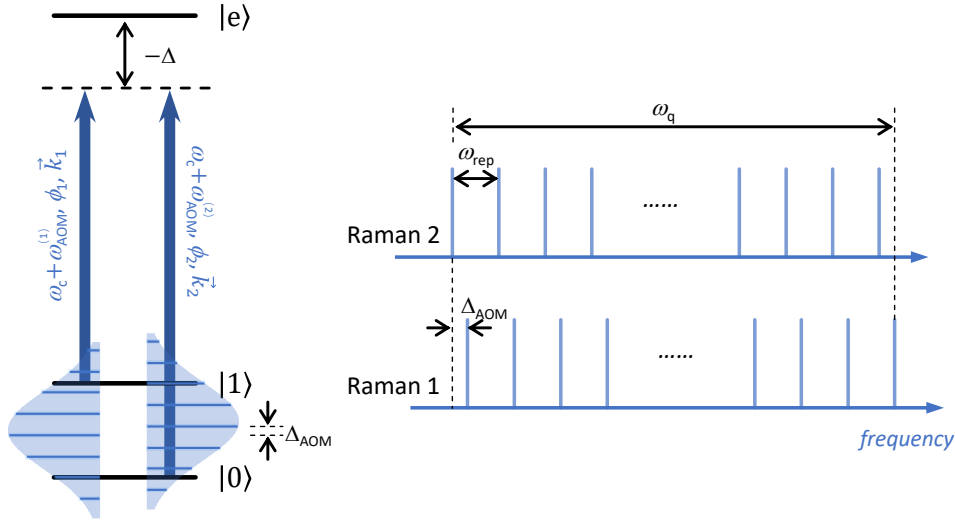


Figure 3.16 Raman transition driven by pulsed laser. The right part clearly shows the frequency combs of the two Raman beams. By tuning the repetition rate or the difference of the two Raman AOMs, we can make sure that the frequency difference of the two combs from two Raman beams matches the energy gap of the qubit.

light shift, which is neglected in the effective Hamiltonian, can be estimated as,

$$\delta_{\text{diff}} \approx -\frac{\sum_{l_1} (g_{l_1}^{(1)})^2 + \sum_{l_2} (g_{l_2}^{(2)})^2}{4\Delta} \frac{\omega_q}{\Delta}. \quad (3-32)$$

By tuning the value of  $\mu$  to near 0,  $\nu$  and  $-\nu$ , we can selectively excite the carrier, red-sideband and blue-sideband transitions, respectively. Therefore, the method of utilizing the pulsed laser is equivalent to that of using the CW laser.

### $^{171}\text{Yb}^+$ driven by 375 nm pulsed laser

In our system, the pulsed laser is produced by a laser of Model Mira-HP (Coherent Laser Group). It is a mode-locked pico-second laser (pulse width  $\sim 4$  ps), utilizing a titanium: sapphire as the gain medium (pumped by a 532 nm laser generated from Verdi-G18) to generate the laser which wavelength can vary from 700 nm to 1000 nm. The center wavelength is set at around 750 nm by rotating the birefringent filter, and then around 500 mW 375 nm pulsed laser is obtained by frequency doubling. The inner structure of the Mira-HP is shown in Fig. 3.17. The length of the laser cavity leads to a repetition rate around 76 MHz. Note that we additionally install a motorized actuator to one of the end mirrors of the cavity; therefore, we can change the repetition frequency by around 0.5 MHz. The repetition rate is directly stabilized by feeding back to the fast response mirror controlled by the piezo. The details of the stabilization system are discussed in App. B.

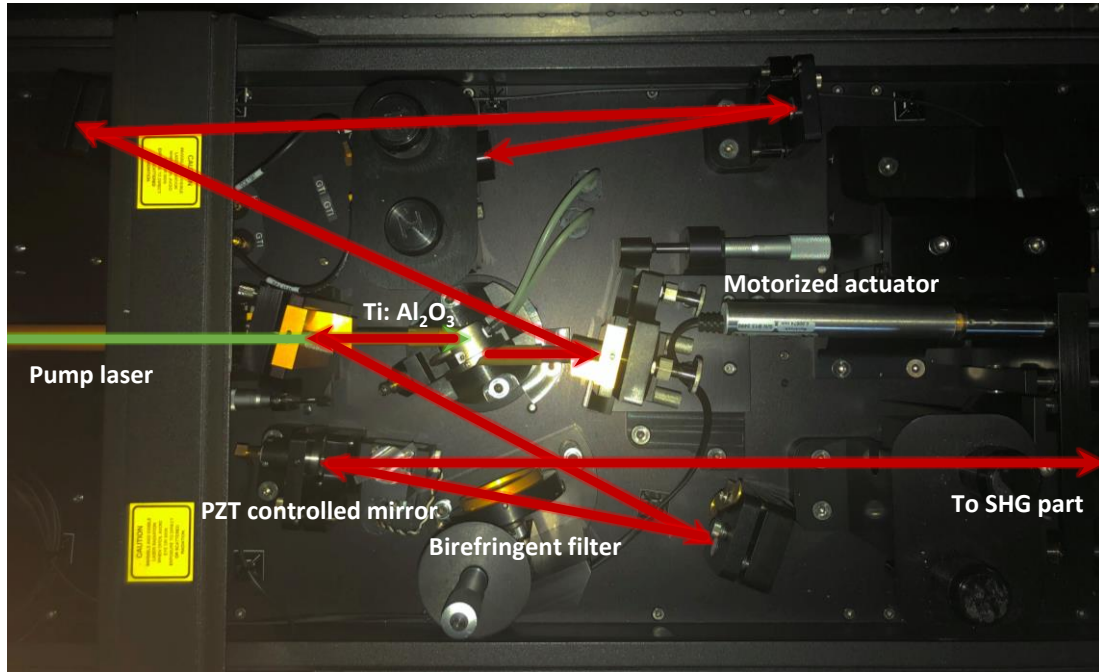


Figure 3.17 Inside alignment of pulsed laser Mira-HP. In this figure, we do not include two parts of the pump laser (Verdi G-18) and the cavity for the second harmonic generation (SHG).

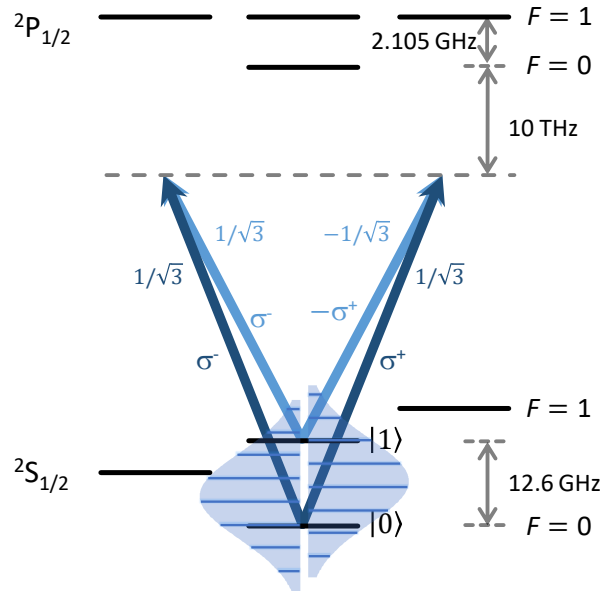


Figure 3.18  $^{171}\text{Yb}^+$  ion qubit driven by 375 nm pulsed laser. Because the transitions of  $|1\rangle \leftrightarrow {}^2P_{1/2} |F = 1, m_F = 0\rangle$  and  $|0\rangle \leftrightarrow {}^2P_{1/2} |F = 0, m_F = 0\rangle$  are dipole-forbidden, we can only use the  ${}^2P_{1/2} |F = 1, m_F = \pm 1\rangle$  as the intermediate levels. A large detuning of 10 THz makes sure that the ion has an extremely small probability to be excited to the  ${}^2P_{1/2}$  levels, which minimizes operational errors caused by Raman scattering.

A  $^{171}\text{Yb}^+$  driven by the 375 nm pulsed laser is shown in Fig. 3.18. In this specific energy structure, we can choose either  $^2P_{1/2}|F = 1, m_F = -1\rangle$  or  $^2P_{1/2}|F = 1, m_F = 1\rangle$  or both as the intermediate level(s) to realize the Raman transitions. These two paths can be coherently added together, and the contribution of each path depends on the polarization of the incident Raman beams and the quantized axis determined by the external magnetic field. Note that the polarization of the Raman beams can not be parallel at the ion's position if they are both linearly polarized. Otherwise, the effective Rabi frequency from each path would coherently cancel each other due to the minus sign in the Clebsch–Gordan coefficients (shown in Fig. 3.18). Moreover, the fourth-order light shift from single Raman beams can be minimized simultaneously if we choose above polarizations<sup>[93]</sup>.

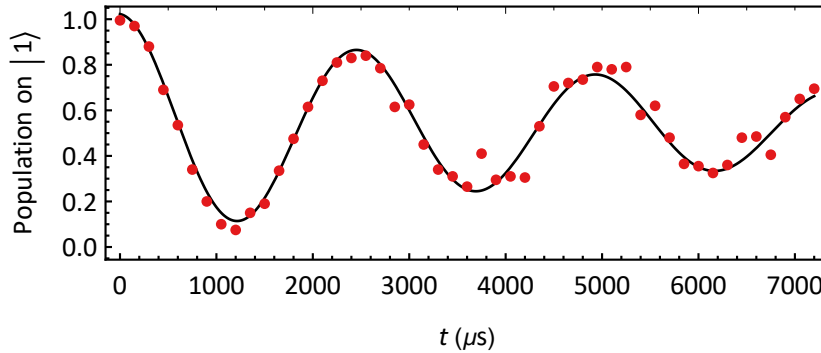


Figure 3.19 Qubit coherence time measured by non-copropagating Raman lasers. Due to the phase instability, the measured coherence time for a single qubit is limited to 6.5 ms.

Compared with the method of utilizing microwave magnetic fields, the way of driving stimulation Raman transitions provides more controllability and feasibility in manipulating the ion qubit and its quantized motion. However, from the aspect of stability, especially the phase stability, a laser system is worse than a microwave horn. The coherence time measured by the non-copropagating Raman beams ( $\vec{k} \neq 0$ ) drops to around 6.5 ms, while more than 20 ms coherence time can be reached if we apply the co-propagating beams ( $\vec{k} = 0$ ). This evidence indicates the noise on the phase difference of the two Raman beams. Currently, we attribute this noise to the jittering of the laser paths. Further passive or active stabilization methods are under exploring.

### 3.3 Timing control in experiment

Up to now, we have introduced initialization, coherent manipulation, and readout of a single  $^{171}\text{Yb}^+$  qubit. Currently, for most demonstrations of quantum computation and

simulation tasks, experimental sequences can be organized in the following steps,

1. Qubit initialization (both qubit and motion),
  - (a) Doppler cooling
  - (b) Sideband cooling
  - (c) Optical pumping
2. Qubit manipulation (either microwave or laser),
3. Qubit readout.

The duration and order of each step should be precisely controlled. Therefore, we utilize timing signals generated by a field-programmable gate array (FPGA) to control the switch-on/off of each device, as shown in Fig. 3.20. Details of our controlling system please check in the thesis of Junhua Zhang<sup>[94]</sup>. Because the qubit state would collapse once being measured, we have to repeat the experimental sequence many times (typically 100 times) to obtain the statistical population on each output state.

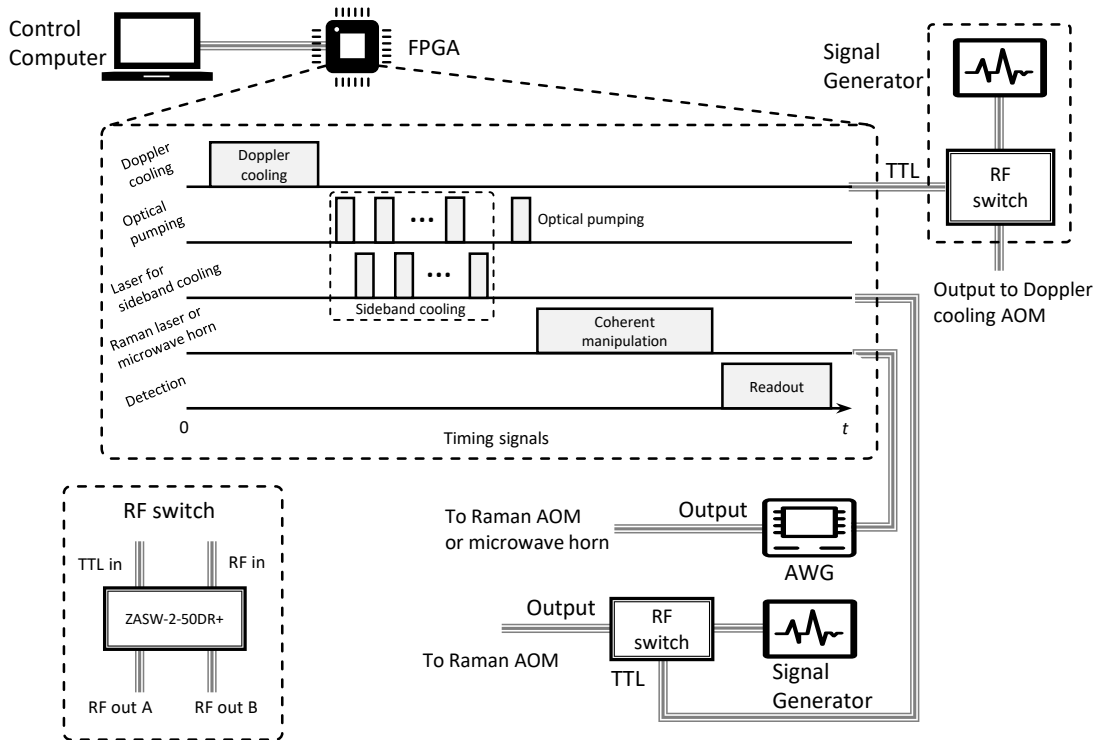


Figure 3.20 Timing control in experiment. The FPGA chip receives a experimental sequence from the computer, and then generates and sends TTL signals to TTL-controlled RF switches. Therefore, we can control the on/off of each operation by controlling the on/off of the RF signal (including all the diffractive beams from the AOMs and the microwave). Typical switching time of the RF switch (Minicircuits ZASW-2-50DR+) is 10 ns, while that of the AOM is around 10-20 ns.

## Chapter 4 Application: Quantum nonequilibrium work relation in the presence of decoherence

The trapped-ion system is extremely attractive for quantum simulation, due to the huge Hilbert space, including the internal electron levels and the quantized harmonic oscillation. Even with just a single ion, the experiments such as the Majorana dynamics<sup>[95]</sup>, the quantum Rabi model<sup>[96]</sup>, the molecular vibronic spectroscopy<sup>[97]</sup> have been successfully demonstrated by our group.

Thanks to the feature of well-isolation, it is feasible to study quantum thermodynamics by utilizing the trapped-ion system. One of the most important researches in the regime of quantum thermodynamics and the statistical mechanics is the fluctuation theorems, which gives a fresh insight to study the nonequilibrium process. Although nonequilibrium work and fluctuation relations have been studied in detail within classical statistical physics, and been explored in the closed quantum system and experimentally studied, extending these results to open quantum systems has proven to be conceptually difficult. The main obstruction is that the definitions of work and heat are not fully settled, hindering experimental verification.

In this chapter, the work relation is studied for a specific example of an open quantum system – namely, a system solely undergoes decoherence as a result of contacting with its environment<sup>[98]</sup>. Based on the trapped-ion system, we experimentally engineer a controllable decohering effect and study its non-trivial influence on work distributions when we do work to a quantum system. Our experimental results reveal the work relation's validity over a variety of driving speeds, decoherence rates, and effective temperatures and represent the first confirmation of the work relation for evolution described by a non-unitary master equation.

### 4.1 Theoretical background

Statements of the second law of thermodynamics are generally expressed as inequalities. For instance, the work performed on a system during an isothermal process must not exceed the net change in its free energy,

$$W \geq \Delta F. \tag{4-1}$$

When statistical fluctuations are appropriately included these inequalities can be reformulated as equalities, such as the nonequilibrium work relation (Jarzynski equality)<sup>[99]</sup>,

$$\langle e^{-\beta W} \rangle = e^{-\beta \Delta F}, \quad (4-2)$$

where  $\beta$  is an inverse temperature and angular brackets denote an average over repetitions of the process. For classical systems, this prediction and related fluctuation theorems have been extensively studied both theoretically<sup>[100]</sup> and experimentally<sup>[101-103]</sup>, and have been applied to the numerical estimation of free energy differences<sup>[104]</sup>.

The last decade has seen growing interest in extending these results to quantum systems<sup>[105]</sup>. This pursuit is made challenging both by the fact that classical work is defined in terms of trajectories – a notion that is typically absent in the quantum setting – and by the lack of a quantum "work operator"<sup>[106]</sup>. To avoid these difficulties, many studies have focused on closed quantum systems, which evolve unitarily. In the absence of a heat bath there is no heat transfer to or from the system and the first law of thermodynamics reads,

$$W = \Delta U \equiv E_f - E_i. \quad (4-3)$$

Here the classical work depends only on a system's initial and final configuration and can be determined from two measurements. This idea is easily lifted to the quantum regime through the two-point measurement (TPM) protocol<sup>[107]</sup>, according to which the work performed during a single experimental run is the difference between energy values  $E_i$  and  $E_f$  resulting from initial and final projective measurements.

If a system is prepared in equilibrium at inverse temperature  $\beta$  with initial Hamiltonian  $H(0) = \sum \epsilon_n |n\rangle\langle n|$ , then evolves unitarily as the Hamiltonian is varied from  $H(0)$  at  $t = 0$  to  $H(\tau) = \sum \bar{\epsilon}_m |\bar{m}\rangle\langle \bar{m}|$  at  $t = \tau$ , the TPM work distribution is given by

$$p(W) = \sum_{n,m} p_n p_{\bar{m}|n} \delta[W - (\bar{\epsilon}_m - \epsilon_n)]. \quad (4-4)$$

Here  $p_n = Z_0^{-1} e^{-\beta \epsilon_n}$  is the probability to obtain the value  $E_i = \epsilon_n$  during the initial energy measurement,  $p_{\bar{m}|n}$  is the conditional probability to obtain the final energy value  $E_f = \bar{\epsilon}_m$ , given the initial value  $\epsilon_n$ , and  $Z_0$  is the partition function for the initial equilibrium state. To date, both proposed<sup>[108-111]</sup> and implemented experimental tests<sup>[112-113]</sup> of the quantum work relation Eq. (4-2) have focused on evaluating equation Eq. (4-4) for a closed system.

A number of authors have proposed definitions of work and derived fluctuation theo-

rems for quantum systems in contact with general thermal environments<sup>[114-116]</sup>. Generally speaking, when a quantum system is coupled to a thermal environment, there arise two distinct departures from unitary dynamics: dissipation, that is the exchange of energy, and decoherence, the leakage of the system's quantum coherences into the environment<sup>[117]</sup>. In this project, we consider situations in which dissipation is negligible over experimentally relevant time scales, but decoherence is substantial. The state evolution under this situation follows the Lindblad master equation,

$$\frac{d\rho}{dt} = -i[H(t), \rho] - \sum_{i \neq j} \gamma_{ij} \rho_{ij} |i\rangle\langle j|, \quad (4-5)$$

which describes both unitary evolution under  $H(t)$  and the decohering effects of the environment. Here  $\gamma_{ij} \geq 0$  are decay rates for the coherences  $\rho_{ij} \equiv \langle i | \rho | j \rangle$ , in the instantaneous eigenbasis of  $H(t)$ . Let

$$\Lambda_\tau : \rho_0 \rightarrow \rho_\tau, \quad (4-6)$$

denotes the quantum evolution that maps an initial density matrix to a final density matrix, under the dynamics of Eq. (4-5). This mapping here is known as the unital evolution, which satisfies the relation,

$$\Lambda_\tau(\mathbb{I}) = \mathbb{I}, \quad (4-7)$$

where  $\mathbb{I}$  is the identity matrix. Under such conditions the environment is a decohering (or dephasing) environment: it suppresses coherences but does not exchange energy.

Consider a system in contact with a decohering environment. At  $t = 0$ , following a projective energy measurement, the system begins in an energy eigenstate  $|\epsilon_n\rangle$ , then it evolves as its Hamiltonian is varied with time. At  $t = \tau$  its energy is again measured, yielding  $\bar{\epsilon}_m$ . By assumption, no energy is exchanged with the environment, therefore we claim that it is natural to identify work to be the difference between the initial and final energies,  $W = \bar{\epsilon}_m - \epsilon_n$ , just as for a closed quantum system. If we accept this as a plausible definition of work in the presence of a decohering environment, then the left hand of Eq. (4-2) can be calculated as follows<sup>[118]</sup>

$$\begin{aligned} \langle e^{-\beta W} \rangle &= \sum_{n,m} p_n p_{\bar{m}|n} e^{-\beta(\bar{\epsilon}_m - \epsilon_n)} \\ &= \sum_{n,m} \frac{e^{-\beta \epsilon_n}}{Z_0} \langle \bar{m} | \Lambda_\tau(|n\rangle\langle n|) | \bar{m} \rangle e^{-\beta(\bar{\epsilon}_m - \epsilon_n)} \end{aligned}$$



$$= \frac{1}{Z_0} \sum_m e^{-\beta \bar{\epsilon}_m} \langle \bar{m} | \Lambda_\tau(\mathbb{I}) | \bar{m} \rangle = \frac{Z_\tau}{Z_0} = e^{-\beta \Delta F}. \quad (4-8)$$

Therefore, the nonequilibrium work relation Eq. (4-2) remains valid even the system undergoes in a decohering environment. The details of a phenomenological approach to derive Eq. (4-2) please check in Ref. [98]

## 4.2 Experimental realization

### 4.2.1 Model Hamiltonian and experimental sequence

To test Eq. (4-2) experimentally, we employ a two-level system engineered from a  $^{171}\text{Yb}^+$  ion. Different from the conventional choice to encode the qubit, in this chapter we use the energy levels  $|F = 0, m_F = 0\rangle \equiv |\downarrow\rangle$  and  $|F = 1, m_F = -1\rangle \equiv |\uparrow\rangle$  in the  $^2S_{1/2}$  manifold as our two-level system, as shown in Fig. 4.1 (a). By applying microwave pulses resonant to our states' energy difference  $\omega_{zq} \equiv \omega_q - \delta_z$ , where  $\delta_z = (2\pi) 13.586\text{MHz}$ , the system can be driven according to the Hamiltonian

$$H(t) = \frac{\Omega(t)}{2} [\sigma_x \cos \Phi(t) + \sigma_y \sin \Phi(t)] = \frac{\Omega(t)}{2} \sigma_{\Phi(t)}. \quad (4-9)$$

Here  $\sigma_{x,y}$  are the standard Pauli matrices defined in the  $\{|\uparrow\rangle, |\downarrow\rangle\}$  basis while  $\Omega$  and  $\Phi$  are parameters controlled through the amplitude and phase of the microwave pulses. In our experiment, we use the driving protocols,

$$\Omega(t) = \Omega_0 \left(1 - \frac{t}{2\tau}\right), \quad (4-10)$$

$$\Phi(t) = \frac{\pi t}{2\tau}, \quad (4-11)$$

where  $\Omega_0$  is the initial Rabi frequency of the magnetic dipole transition, which can also be treated as the effective energy gap of the two-level system in the dressed state picture, and  $\tau$  is the duration of the process. Together equations Eq. (4-9) and Eq. (4-10) represent the Hamiltonian portion of our system's dynamics, or the protocol of applying the work to the system. Our Hamiltonian has the form  $H(t) = \mathbf{B}(t) \cdot \boldsymbol{\sigma}$ , where the effective field  $\mathbf{B}(t)$  undergoes rotation by  $90^\circ$  in the  $xy$ -plane, as shown in Fig. 4.1 (b). By varying the value of  $\tau$ , a different amount of work can be done to the system. The controllable decohering rate  $\gamma = \gamma_{\downarrow\uparrow} = \gamma_{\uparrow\downarrow}$  in Eq. (4-5) is engineered by adding an intensity noise to the Rabi frequency of the magnetic dipole interaction<sup>[119-121]</sup>, which will be discussed in the later section in detail.

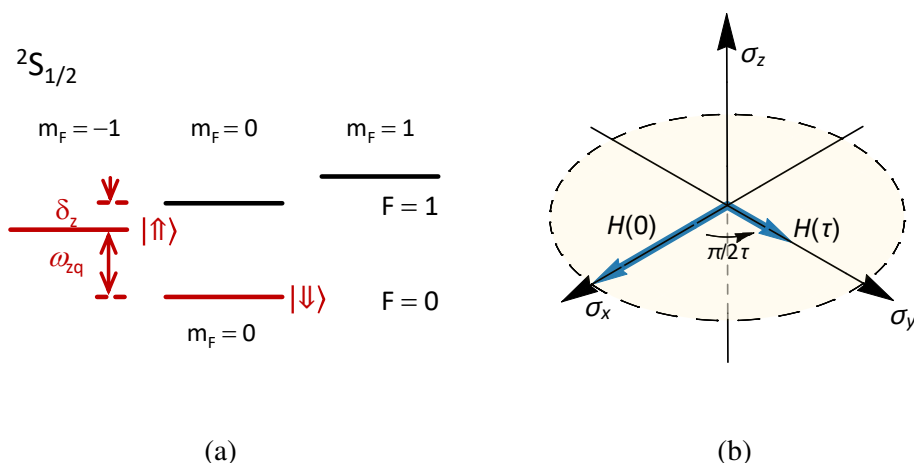


Figure 4.1 Two-level system encoded in  $^{171}\text{Yb}^+$  ion and experimental driving protocol. (a) In this project, the Zeeman levels is employed as our two-level system, which is convenient to prepare the initial effective thermal state by utilizing its short coherence time. (b) In this experiment, the driving protocol is designed to rotate the effective field by 90 degree while reducing the strength to half.

Given this system, the procedure for measuring the work applied during a single experimental trial involves four steps,

1. thermal state preparation,
2. initial energy measurement,
3. application of the driving protocol,
4. final energy measurement,

as shown in Fig. 4.2. Here we introduce every step in detail as follows.

**Thermal state preparation.** For technical reasons, the initial thermalization is prepared in the  $\sigma_z$  basis. We create the initial thermal state using the following procedure. First we prepare the pure state  $|\psi\rangle = c_\uparrow|\uparrow\rangle + c_\downarrow|\downarrow\rangle$  by applying the single-qubit rotation  $R_\phi(\theta)$  with a proper  $\theta$  (the rotation axis  $\phi$  can be arbitrary). After waiting more than 10 times the coherence time ( $\tau_c$  is around  $140 \mu\text{s}$  for our Zeeman qubit during this project), the state becomes a mixed-state described by the density operator  $\rho_{\text{ini}} = |c_\uparrow|^2|\uparrow\rangle\langle\uparrow| + |c_\downarrow|^2|\downarrow\rangle\langle\downarrow|$ , which is identical to thermal equilibrium state  $\exp(-H(0)/k_B T)$  with an effective temperature

$$T = \frac{\hbar\Omega_0}{k_B \ln(|c_\downarrow|^2/|c_\uparrow|^2)}, \quad (4-12)$$

For our experiment,  $\Omega_0 = 2\pi \times 50 \text{ kHz}$  while  $|c_\downarrow|^2$  took values of  $0.804 \pm 0.034$  and  $0.605 \pm 0.041$ , corresponding to effective initial state temperatures of  $T_1 = 5.63 \mu\text{K}$  and

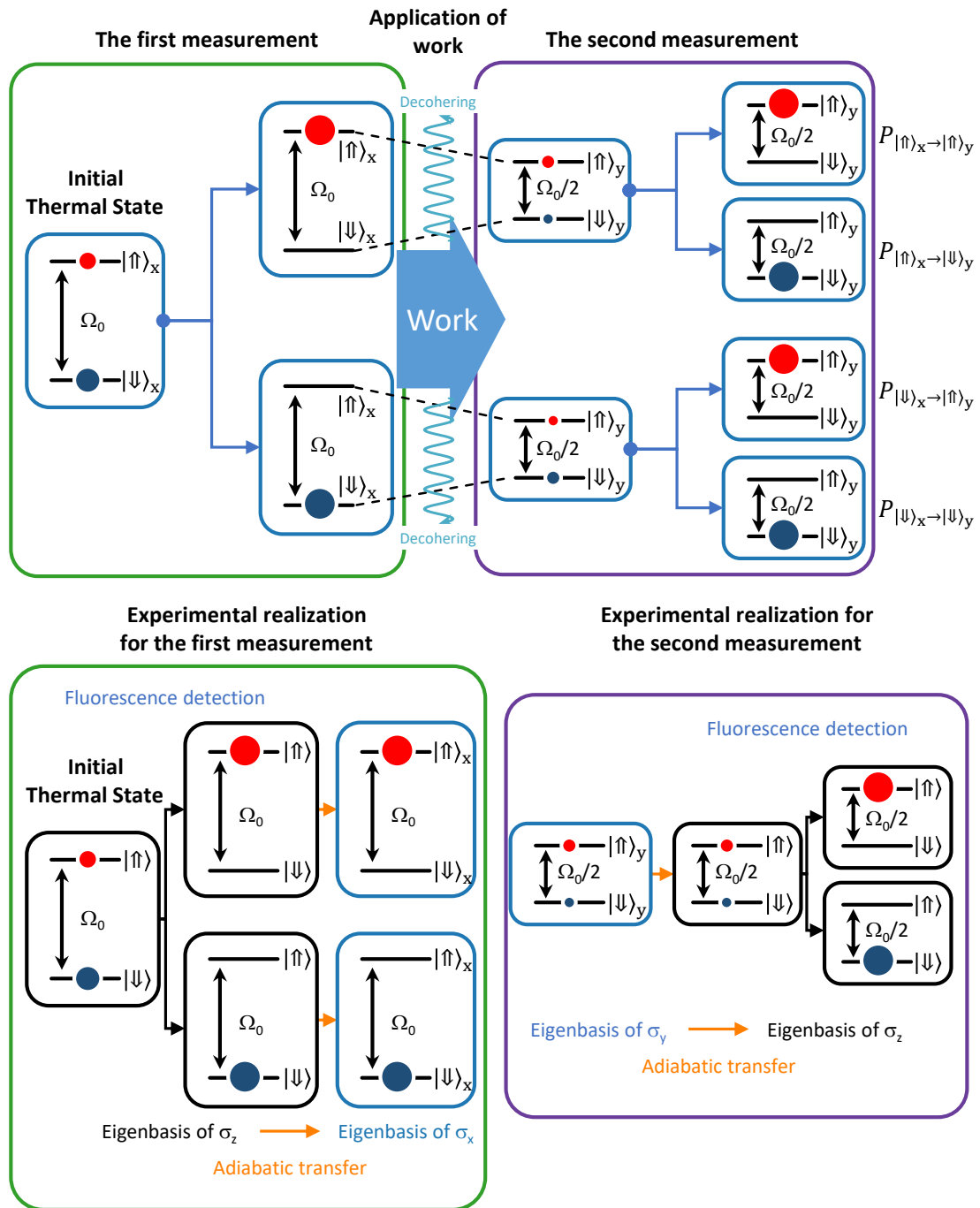


Figure 4.2 Conceptual and actual experimental schematics of TMP protocol. In the experiment, thermal state preparation and initial energy measurement occur in the  $\sigma_z$  eigenbasis before being transferred to the basis of  $\sigma_x$  with the aid of an adiabatic shortcut. Similarly, the system is again rotated, this time from the  $\sigma_y$  to  $\sigma_z$  basis, proceeding the second fluorescence measurement.

$T_2 = 1.70 \mu\text{K}$ , respectively. The density matrices for both effective thermal state obtain through the state tomography are shown in Fig. 4.3.

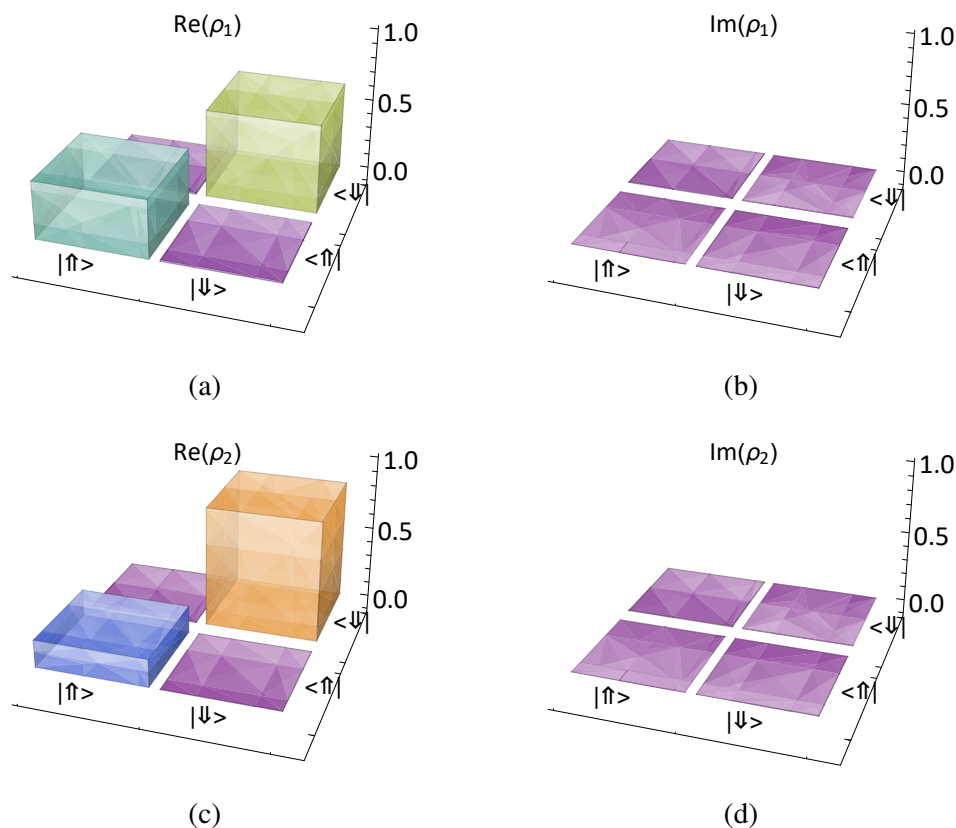


Figure 4.3 Density matrices after preparing effective thermal states, which are equivalent to (a-b)  $T_1 = 5.63 \mu\text{K}$  and (c-d)  $T_2 = 1.70 \mu\text{K}$ .

**Initial energy measurement.** Following initial state preparation, the energy of the system is measured in  $\sigma_z$  basis. When the ground state  $|\downarrow\rangle$  (dark state) is measured, the system remains unchanged during the detection sequence and we simply continue to the next step of the experiment. If the excited state  $|\uparrow\rangle$  (bright state) is detected, the system is left in a mixture of the three levels of  $F = 1$  in  $^2S_{1/2}$  manifold. Therefore, we re-prepare the  $|\uparrow\rangle$  state using the optical pumping and a  $\pi$ -rotation before continuing the experiment. As noted above, the actual measurements are performed with respect to the Hamiltonian  $\sigma_z$  which is then switched to  $\sigma_x$  using an adiabatic shortcut, which will be introduced in the latter section.

**Application of driving with decohering.** At this point the noisy microwave pulses are applied to the system resulting in evolution according to the Hamiltonian in Eq. (4-9) with the protocols in Eq. (4-10). To verify the nonequilibrium equation, we should vary

the ratio between the duration  $\tau$  and the inverse energy gap  $\Omega_0^{-1}$  from  $\tau/\Omega_0^{-1} > 1$  to  $\tau/\Omega_0^{-1} < 1$  to cover the near adiabatic, intermediate, and far-from-equilibrium protocols. The amplitude of the noise on the Rabi frequency is controlled to achieve different decoherence rate.

**The final energy measurement.** Prior to the final energy measurement, another adiabatic shortcut is used to switch the system's Hamiltonian—this time from  $\sigma_y$  to  $\sigma_z$ . Following this transfer, the energy of the system is once again measured. By calculating the difference between the initial and final energy measurements, a work value for the experimental trial is obtained.

The work distribution is obtained by repeating the sequence with the same effective temperature, the duration of the process and the decohering rate for over 2000 times.

#### 4.2.2 Engineering decoherence environment

In the experiment, the decohering environment is induced or simulated by adding an extra noise to the amplitude of the microwave magnetic field. The noisy version of the driving Hamiltonian Eq. (4-9) can be written as,

$$H_N(t) = \frac{\Omega(t) + \Omega_0 \xi(t)}{2} \sigma_{\Phi(t)} = H(t) + \xi(t) H_{\xi}(t). \quad (4-13)$$

Here  $\xi(t)$  is a Gaussian white noise which satisfies the conditions of  $\langle \xi(t) \rangle = 0$  and  $\langle \xi(t) \xi(t') \rangle = \alpha^2 \delta(t - t')$ , where  $\langle \cdot \rangle$  denotes the ensemble averaging over all the possible noise and  $\delta(t - t')$  is the standard delta function. For convenience, we define the Wiener process,

$$W(t) = \int_0^t \xi(s) ds, \quad (4-14)$$

$$dW(t) = W(t + dt) - W(t), \quad (4-15)$$

$$\langle dW(t) \rangle = 0, \quad (4-16)$$

$$\langle dW(t) dW(t) \rangle = \alpha^2 dt. \quad (4-17)$$

The state evolution governed by the Hamiltonian in Eq. (4-13) follow the stochastic Schrödinger equation<sup>[122]</sup>,

$$d|\psi\rangle = -iH(t)|\psi\rangle dt - \frac{\alpha^2}{2} H_{\xi}(t) H_{\xi}(t) |\psi\rangle dt - iH_{\xi}(t) |\psi\rangle dW, \quad (4-18)$$

or in the form of density matrix,

$$d\rho = -i[H(t), \rho]dt - \frac{\alpha^2}{2}\{H_\xi(t)H_\xi(t), \rho\}dt + \alpha^2 H_\xi(t)\rho H_\xi(t)dt - i[H_\xi(t), \rho]dW, \quad (4-19)$$

where  $[\cdot]$  and  $\{\cdot\}$  denote the commutator and the anti-commutator, respectively. By averaging over all the possible noise, the evolution of the ensemble state,  $\bar{\rho} = \langle \rho \rangle$ , follows,

$$\frac{d\bar{\rho}}{dt} = -i[H(t), \bar{\rho}] + \alpha^2 \left\{ H_\xi(t)\bar{\rho}H_\xi(t) - \frac{1}{2}\{H_\xi(t)H_\xi(t), \bar{\rho}\} \right\}. \quad (4-20)$$

Given  $H_\xi$  in Eq. (4-13), the above equation can be further simplified to be,

$$\frac{d\bar{\rho}}{dt} = -i[H(t), \bar{\rho}] - \frac{\alpha^2 \Omega_0^2}{2} (\rho_{\uparrow\Phi\downarrow\Phi} |\uparrow\Phi\rangle\langle\downarrow\Phi| + \rho_{\downarrow\Phi\uparrow\Phi} |\downarrow\Phi\rangle\langle\uparrow\Phi|), \quad (4-21)$$

where  $|\uparrow\Phi\rangle$  and  $|\downarrow\Phi\rangle$  are the instantaneous eigenbasis of  $H(t)$ . Eq. (4-21) is the exactly same to Eq. (4-5) with

$$\gamma = \frac{\alpha^2 \Omega_0^2}{2}. \quad (4-22)$$

Therefore, the decohering rate of  $\gamma$  can be controlled in the experiment by varying the deviation of  $\alpha$  of the white noise.

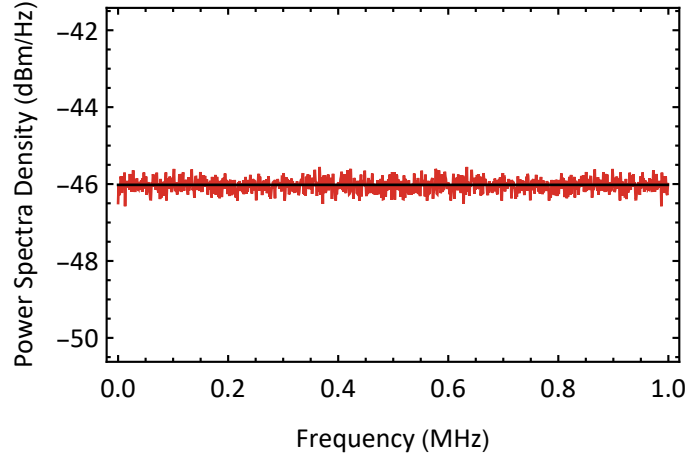


Figure 4.4 Power spectral density of discrete Gaussian white noise with standard deviation  $\alpha = 1$  and sampling rate 1 MHz

In practice, we can only apply discrete noise with a sampling rate of  $R_s$  instead of ideal continuous-Gaussian white noise. When  $R_s^{-1}/2$  is much less than the duration of the operation, the digital noise can be approximated as a ideal Gaussian white noise,

which has a finite bandwidth due to the discrete sampling, as shown in Fig. 4.4. And the auto-correlation function is modified to be  $\langle \xi(t)\xi(t') \rangle = \alpha^2 R_s^{-1} \delta(t - t')$ . Therefore, the decohering rate should be revised as

$$\gamma = \frac{\alpha^2 \Omega_0^2}{2R_s}. \quad (4-23)$$

In our experiment, the noise sampling rate is set to 1 MHz. Therefore, the decoherence rate is given by  $\gamma_{\text{exp}} = (\alpha\Omega_0)^2/2$  MHz when  $\Omega_0$  is measured in MHz. And Fig. 4.5 clearly shows this linear relation between the decoherence rate and the effective auto-correlation amplitude of the applied discrete Gaussian white noise.

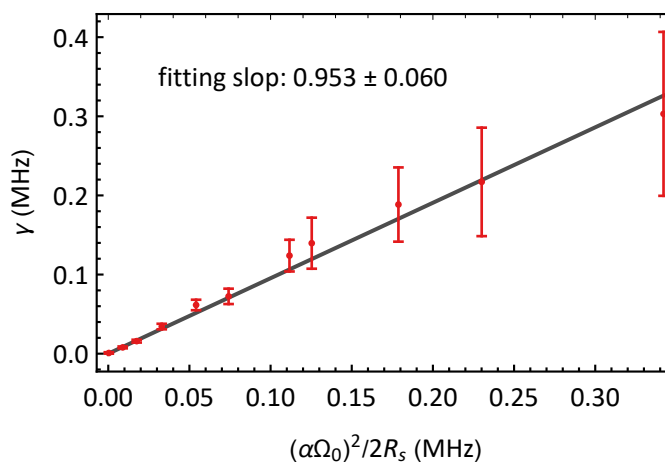


Figure 4.5 Experiment results of decoherence rate  $\gamma$  relation with  $(\sigma\Omega_0)^2/2R_s$ . Here sampling rate is set as 1 MHz. The slope of the fitting result is  $0.953 \pm 0.060$ , with respect to the theoretical value of 1.

### 4.2.3 Adiabatic shortcuts in projective measurement

For our setup, the initial and final energy measurements are performed in the  $\sigma_z$  basis. Between the measurement sequences and the driving protocol, the state of the system must be transferred between the z-axis and x-y plane of the Bloch sphere. To accomplish this task, we use adiabatic shortcuts – a protocol that has the same effect as an adiabatic switching of the Hamiltonian but occurs in finite time<sup>[123-124]</sup>. Specifically, we apply an additional counterdiabatic term to our Hamiltonian during the switching process to achieve the adiabatic shortcut.

Here we take the first projective measurement as an example. In detail, the basis rotation is achieved by rotating the effective field from the  $\sigma_z$  direction to the  $\sigma_x$  direction.

The Hamiltonian of this process can be written as,

$$H_{1\text{st}}(t) = \frac{\Omega_0}{2} \left[ \sigma_z \cos\left(\frac{\pi t}{2\tau_{1\text{st}}}\right) + \sigma_x \sin\left(\frac{\pi t}{2\tau_{1\text{st}}}\right) \right], \quad (4-24)$$

where  $t$  varies from 0 to  $\tau_{1\text{st}}$ , and  $\tau_{1\text{st}}$  should be much longer than  $\Omega_0$  to satisfy the adiabatic approximation. However, due to the limited coherence time of the two-level system encoded in the Zeeman levels, the adiabatic transition would result in serious errors in the stage of the basis rotation. To realize a fast and robust basis rotation, we apply an adiabatic shortcut by adding an additional counterdiabatic term<sup>[124]</sup>,

$$H_{c,1\text{st}} = i \sum_{m \neq n} \frac{|m\rangle\langle m| \partial_t H_{1\text{st}} |n\rangle\langle n|}{E_n - E_m}. \quad (4-25)$$

Here  $|m\rangle$  and  $|n\rangle$  should be the instantaneous eigenbasis of  $H_{1\text{st}}(t)$ , and  $E_m$  and  $E_n$  are the corresponding eigen-energies. By inserting Eq. (4-24) into Eq. (4-25), the counterdiabatic Hamiltonian turns out to be,

$$H_{c,1\text{st}} = \frac{\Omega_0}{2} \sigma_y. \quad (4-26)$$

The term proportional to  $\sigma_y$  suppresses non-adiabatic excitation. In the experiment, we choose  $\tau_{1\text{st}} = 5 \mu\text{s}$ , which is much shorter than the conventional adiabatic rotation. Similarly, the Hamiltonian for the basis rotation in the second projective measurement is,

$$H_{2\text{nd}}(t) = \frac{\Omega_0}{4} \left[ \sigma_y \cos\left(\frac{\pi t}{2\tau_{2\text{nd}}}\right) + \sigma_z \sin\left(\frac{\pi t}{2\tau_{2\text{nd}}}\right) \right] + \frac{\Omega_0}{4} \sigma_x, \quad (4-27)$$

where  $\tau_{2\text{nd}}$  is chosen to be  $10 \mu\text{s}$ , and the counterdiabatic term is proportional to  $\sigma_x$ .

### 4.3 Experimental results

In the experiment, we start from the effective thermal state with two different temperatures of  $T_1 = 5.63 \mu\text{K}$  and  $T_2 = 1.70 \mu\text{K}$ , as we mentioned before. The duration of applying work is chosen to be  $\tau = 50, 10$  and  $5 \mu\text{s}$ , corresponding to the near adiabatic, intermediate and far-from-equilibrium process, respectively. The decohering rate  $\gamma$  is set to 0, 448 or 1340 kHz which corresponds to the cases of no, intermediate, or the large decohering strength, respectively. Fig. 4.6 shows the work distributions resulting from experiments conducted with twelve different combinations of effective temperature  $T$ , driving time  $\tau$ , and decoherence rate  $\gamma$ . From the data, it is clear that decoherence non-trivially affects the work distribution for a given process – for instance compare (a.4)



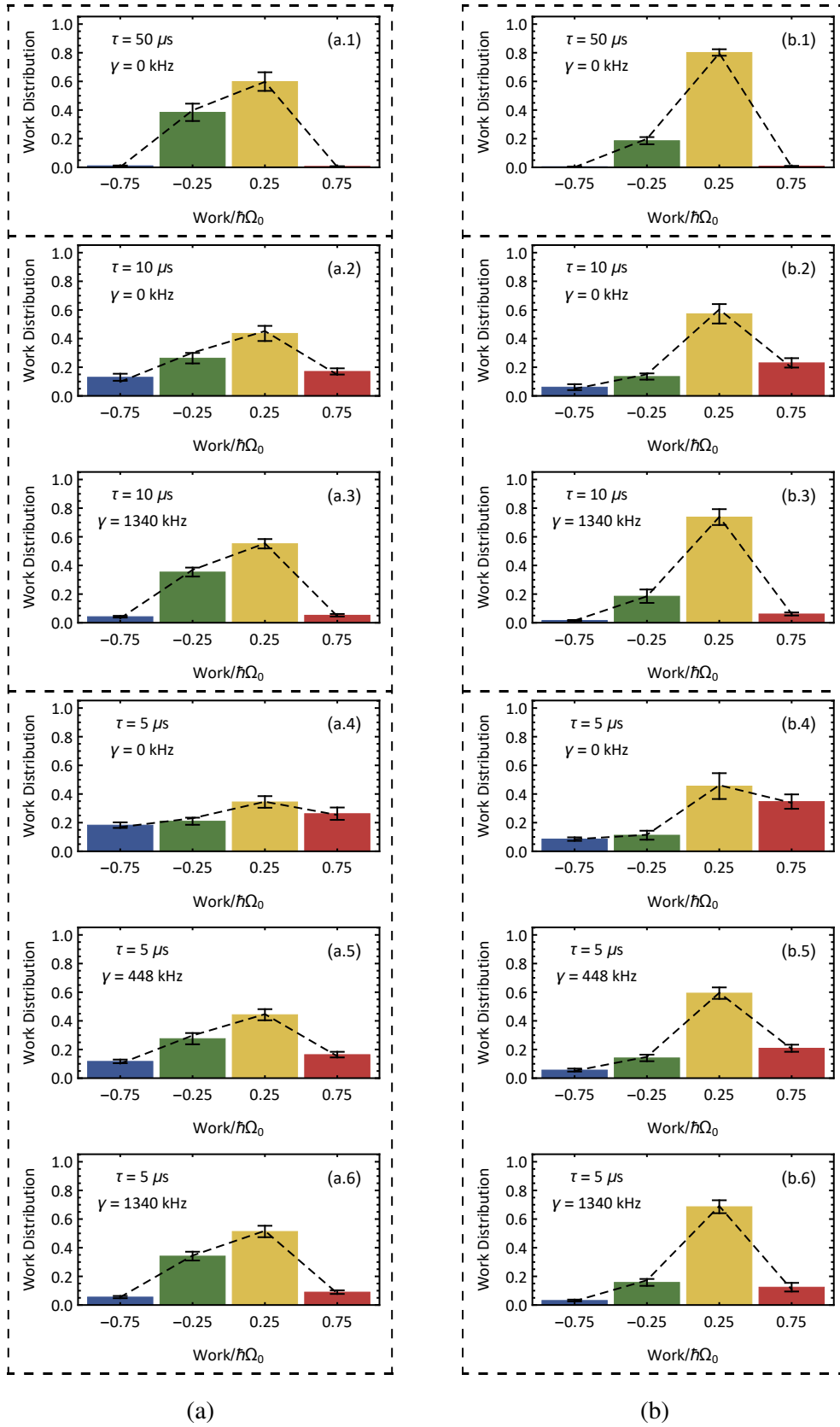


Figure 4.6 Work distributions measured with different work protocols. The distributions (a.1)-(a.6) correspond to an initial temperature of  $T_1 = 5.63 \mu\text{K}$  while (b.1)-(b.6) have  $T_2 = 1.70 \mu\text{K}$ .

- (a.6) (or (b.4) - (b.6)) in figure 4.6. A more careful inspection reveals that the qualitative behavior of the work distribution is governed by a competition between driving speed and decoherence.

For near-adiabatic driving, the work distribution is peaked at values  $W = \bar{\epsilon}_i - \epsilon_i$  corresponding to the measurement of two energies with the same quantum number. Increasing driving speed (decreasing  $\tau$ ) tends to induce transitions among energy states with different quantum numbers, thereby broadening the work distribution. This effect is exemplified in figure 4.6 by distributions (a.1), (a.2), and (a.4). With above work distributions in the decoherence-free condition, we can estimate the changing of the free energy,  $\Delta F$ , utilizing either

$$\Delta F^J = -\frac{1}{\beta} \ln [\langle e^{-\beta W} \rangle], \quad (4-28)$$

or

$$\Delta F^{\text{Ad}} = \langle W \rangle, \quad (4-29)$$

while the exact value of  $\Delta F$  can be calculated by

$$\Delta F = \frac{1}{\beta} \ln \left[ \frac{\text{Tr} [e^{-\beta H(0)}]}{\text{Tr} [e^{-\beta H(\tau)}]} \right]. \quad (4-30)$$

Note that, Eq. (4-29) should be established only when the driving process is near adiabatic. According to the work distribution shown in (a.1), Eq. (4-28) and Eq. (4-29) estimate  $\Delta F$  to be  $\Delta F^J = 0.036\hbar\Omega_0$  and  $\Delta F^{\text{Ad}} = 0.051\hbar\Omega_0$ , respectively, while the exact value of  $\Delta F$  is around  $0.039\hbar\Omega_0$ . Both methods estimate the changing of the free energy quite well, indicating that we drive the system adiabatically. However, if we consider the work distribution of (a.4), these two methods reveal the estimated  $\Delta F$  of  $\Delta F^J = 0.034\hbar\Omega_0$  and  $\Delta F^{\text{Ad}} = 0.094\hbar\Omega_0$ . Now, the free energy difference estimated by Eq. (4-29) deviates from the real value a lot, indicating the driving process in (a.4) is surly away from equilibrium.

In contrast, decoherence in the eigenbasis of  $\hat{H}(t)$  suppresses transitions among energy states with different quantum numbers, bringing the work distribution closer to its adiabatic form. This can be seen by comparing the near adiabatic distribution (a.1) with the fast driving cases (a.4),(a.5), and (a.6) which have varying degrees of decoherence. Interpreting this decoherence as the environmental measurement of the system's energy, one can see that the system is forced to follow the adiabatic trajectory due to wave function collapse. When the collapse rate  $\gamma$  becomes large, the system becomes trapped

in an eigenstate of the instantaneous Hamiltonian – a scenario analogous to the quantum Zeno effect.

With these distributions, the work relation can be tested for each choice of the experimental parameters  $T$ ,  $\tau$ , and  $\gamma$  by direct comparison of the left- and right-hand sides of Eq. (4-2). Note that the quantity  $\langle e^{-\beta W} \rangle$  is calculated using the work distribution while  $e^{-\beta \Delta F}$  follows straightforwardly from knowledge of the energy levels of  $\hat{H}(0)$  and  $\hat{H}(\tau)$ . The results of these calculations, shown in Fig. 4.7, agree to within the error of the experiment and hence validate the work relation.

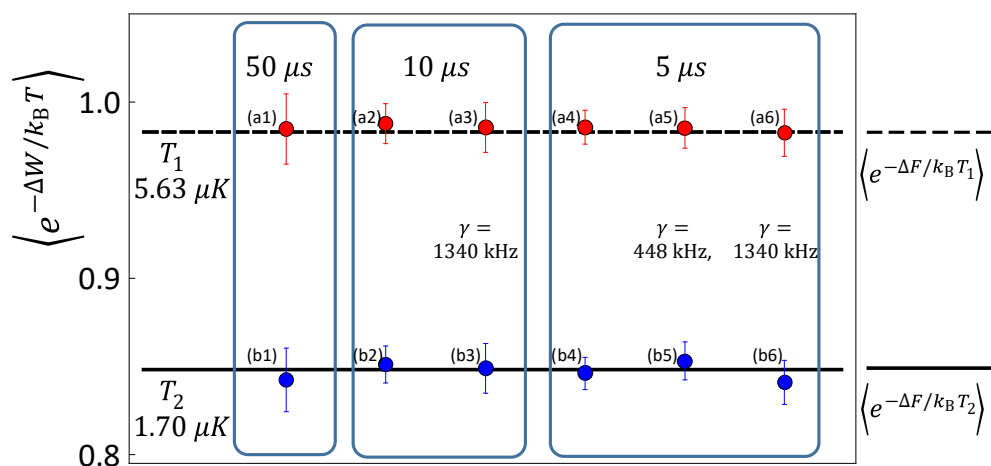


Figure 4.7 Comparison of the exponential average of work for distributions in Fig. 4.6 to the exponential of the free energy difference calculated from the initial and final energy levels of  $H(t)$ .

#### 4.4 Conclusion

While lots of theoretical developments focus on environment-induced decoherence, in fact, the dephasing master equation of Eq. (4-5) can be interpreted in various ways. For instance, (a) the same master equation describes – at the ensemble level – a system that evolves unitarily but is interrupted at random by projective measurements. More precisely, if our experimenter makes measurements in the instantaneous eigenbasis of  $H(t)$  at times dictated by a Poisson process with rate  $\gamma$ , then the density operator resulting from averaging over all measurement realizations obeys Eq. (4-5), with  $\gamma_{ij} = \gamma$ . Yet another interpretation of the dephasing master equation arises when (b) one averages over the noise that is introduced by adding an appropriately designed, randomly fluctuating term to the bare system Hamiltonian  $H(t)$ <sup>[119-120]</sup>. Both interpretations, (a) and (b), support

a fluctuation theorem.

In summary, we have studied the quantum work relation for a system in contact with a decohering bath. Using a system constructed from trapped ions subjected to noisy dynamics, we conducted an experiment that demonstrated the work relation's validity for a dephasing process and represents the first test of Eq. (4-2) beyond the regime of closed quantum systems. These results demonstrate the applicability of fluctuation theorems to open quantum systems, at least for the special case of a decohering heat bath, and may spur additional tests of the work relation for systems with dissipation.

## Chapter 5 Quantum control on multiple qubits

Up to now, we have already introduced quantum operations on a single ion qubit in Chap. 3, and shown that some quantum simulations can be demonstrated even with a single ion. It is time to move to manipulations of multiple qubits. For large-scale universal quantum computation, we require not only a scalable architecture to hold a large amount of the qubits, but also the physical realization of a universal gate set consisting of arbitrary single-qubit rotations and two-qubit entangling gates<sup>[20]</sup>.

In the ion trap community, both Quantum CCD and ion-photon<sup>[125-126]</sup>, two architectures are pursued simultaneously for the scalable quantum computing. In any situation, a single ion-crystal consisting of several ion qubits is treated as the minimal modular, and the capability of individually controlling each qubit is required to apply the universal gate set.

In this chapter, we would first introduce how a two-qubit entangling gate can be achieved on two ion qubits through the collective motion shared by the different ions, where a feature called full connectivity among the whole ion-chain naturally occurs. Then starting from a single ion-crystal as the hardware, we would discuss the experimental realization of multiple qubits initialization, individually coherent manipulations, and detection. Here, the most crucial part is the so-called individual laser addressing system. Finally, as complementary, we would briefly show several schemes to achieve robust single- and two-qubit operations when noises of the system are considered.

### 5.1 Two-qubit entangling gate

In the trapped-ion system, the outmost electron of each ion occupies its lowest orbit, and the average ion-spacing is usually around microns. Therefore, unlike Rydberg atoms, ions cannot interact with each other directly. Instead, an ion-ion interaction is excited through the collective motion induced by the Coulomb interaction. The first scheme of the two-qubit entangling gate was proposed by Ignacio Cirac and Peter Zoller in 1995<sup>[127]</sup>, known as Cirac-Zoller (CZ) gate, and experimentally implemented in 2003<sup>[128]</sup>. However, the performance of the CZ gate can quickly drop if the ions are not well cooled to their motional ground state, and this critical requirement makes it hard to scale up. Another proposal of a Doppler-free gate was made in 1999 by Klaus Mølmer and Anders

Sørensen<sup>[129]</sup>, known as Mølmer-Sørensen (MS) gate, which was developed into geometric phase gates soon after<sup>[130-133]</sup>. This type of gate is insensitive to the initial motional state, which makes it widely used in the trapped-ion community. In this section, we would detail the realization of the MS-type two-qubit entangling gate.

### 5.1.1 State-dependent force

For the sake of simplicity, we illuminate the same intensity of the driving laser onto an ion-chain containing two ions. The interaction Hamiltonian of Eq. (3-20) is revised to,

$$H = \sum_{m=1}^2 \nu_m a_m^\dagger a_m + \sum_{j=1}^2 \frac{\Omega}{2} \left( \sigma_+^j e^{i(\sum_{m=1}^2 \eta_{j,m}(a_m + a_m^\dagger) - \mu t + \phi)} + \text{h.c.} \right). \quad (5-1)$$

Here  $a_m$  and  $a_m^\dagger$  are the annihilation and creation operators of the  $m$ -th normal mode, respectively, and  $\nu_m$  is the corresponding mode frequency.  $\sigma^j$  is the Pauli matrices of the  $j$ -th ion qubit. We also assume that the effective wave vector of two Raman lasers only couples to one of the transverse direction (denoted as  $x$ -direction), resulting in a relation of,

$$k \cdot x_j = \sum_{m=1}^2 \eta_{j,m}(a_m + a_m^\dagger). \quad (5-2)$$

Here the local position operator  $x_j$  is decomposed into the linear combination of the normal-mode operators.  $\eta_{j,m}$  is the scaled Lamb-Dicke parameter in which includes the factor from the normal mode transformation matrix<sup>[43]</sup>,

$$\eta_{j,m} = b_{j,m} k \sqrt{\frac{\hbar}{2M\nu_m}}. \quad (5-3)$$

By tuning the value of  $\mu$  to near  $\nu_m$  or  $-\nu_m$ , we can excite either multi-mode blue or red sideband transition as follows,

$$H_b = \sum_{j=1}^2 \sum_{m=1}^2 \frac{i\eta_{j,m}\Omega_b}{2} \left( \sigma_+^j a_m^\dagger e^{i(\nu_m - \mu_b)t} e^{i\phi_b} - \text{h.c.} \right), \quad (5-4)$$

$$H_r = \sum_{j=1}^2 \sum_{m=1}^2 \frac{i\eta_{j,m}\Omega_r}{2} \left( \sigma_+^j a_m e^{-i(\nu_m + \mu_r)t} e^{i\phi_r} - \text{h.c.} \right). \quad (5-5)$$

Here we have already chosen the rotating frame with respect to  $\sum_{m=1}^2 \nu_m a_m^\dagger a_m$ , and ignored the off-resonant terms. Note that, a state-dependent force can be obtained if we apply bichromatic fields with  $\mu_b = \mu$  and  $\mu_r = -\mu$  simultaneously, which can be expressed as a

Hamiltonian with the form of<sup>[89,134]</sup>,

$$H_{\text{SDF}} = \sum_{j=1}^2 \sum_{m=1}^2 \frac{\eta_{j,m}\Omega}{2} (a_m^\dagger e^{i\delta_m t} e^{-i\phi_p} + a_m e^{-i\delta_m t} e^{i\phi_p}) \sigma_{\phi_s}^j. \quad (5-6)$$

Here  $\delta_m = \nu_m - \mu$  is the detuning with respect to the  $m$ -th mode, and the strengths of both sideband transitions are assumed to be the same,  $\Omega_r = \Omega_b = \Omega$ . The optical phases,  $\phi_b$  and  $\phi_r$ , can be decomposed into two parts for the motion and qubit, with the forms of  $\phi_p = (\phi_r - \phi_b)/2$  and  $\phi_s = (\phi_b + \phi_r + \pi)/2$ , respectively. We can also define a complex force of  $f_{j,m} = \eta_{j,m}\Omega e^{-i\phi_p}/2$ . Without loss of generality, we set  $\phi_p = \phi_s = 0$ , leading to a  $\sigma_x$ -dependent force,

$$H_{\text{SDF}} = \sum_{j=1}^2 \sum_{m=1}^2 \frac{\eta_{j,m}\Omega}{2} (a_m^\dagger e^{i\delta_m t} + a_m e^{-i\delta_m t}) \sigma_x^j. \quad (5-7)$$

### 5.1.2 Unitary evolution operator

The time evolution governed by the Hamiltonian in Eq. (5-7) can be written as,

$$U(\tau) = \mathcal{T} \exp \left[ -i \int_0^\tau H_{\text{SDF}}(t) dt \right]. \quad (5-8)$$

This is a time-ordered integral because of  $[H_{\text{SDF}}(t_2), H_{\text{SDF}}(t_1)] \neq 0$  if  $t_2 \neq t_1$ . Fortunately, by utilizing Magnus formula, Eq. (5-8) can be analytically calculated as follows<sup>[89]</sup>,

$$U(\tau) = \exp \left\{ -i \int_0^\tau H_{\text{SDF}}(t) dt - \frac{1}{2} \int_0^\tau dt_2 \int_0^{t_2} [H_{\text{SDF}}(t_2), H_{\text{SDF}}(t_1)] dt_1 \right\}. \quad (5-9)$$

In detail, the first integral in the exponential turns out to be,

$$\begin{aligned} T_1 &= -i \int_0^\tau H_{\text{SDF}}(t) dt \\ &= -i \int_0^\tau \sum_{j=1}^2 \sum_{m=1}^2 \frac{\eta_{j,m}\Omega}{2} (a_m^\dagger e^{i\delta_m t} + a_m e^{-i\delta_m t}) \sigma_x^j dt \\ &= \sum_{j=1}^2 \sum_{m=1}^2 \left( \alpha_{j,m}(\tau) a_m^\dagger - \alpha_{j,m}^*(\tau) a_m \right) \sigma_x^j, \end{aligned} \quad (5-10)$$

where,

$$\alpha_{j,m}(\tau) = -i \frac{\eta_{j,m}\Omega}{2} \int_0^\tau e^{i\delta_m t} dt = \frac{\eta_{j,m}\Omega}{2} \frac{1 - e^{i\delta_m \tau}}{\delta_m}. \quad (5-11)$$

Obviously, the result of the first integral reveals to be a state-dependent displacement operator on multiple motional modes, which entangles the qubit states with their displacement in the position-momentum phase space.

The second term in Eq. (5-9) is a double-integral which can be simplified to be,

$$\begin{aligned}
 T_2 &= -\frac{1}{2} \int_0^\tau dt_2 \int_0^{t_2} [H_{\text{SDF}}(t_2), H_{\text{SDF}}(t_1)] dt_1 \\
 &= -\sum_{j,j'=1}^2 \sum_{m,m'=1}^2 \frac{\eta_{j,m}\eta_{j',m'}\Omega^2}{8} \sigma_x^j \sigma_x^{j'} \\
 &\quad \int_0^\tau dt_2 \int_0^{t_2} dt_1 [a_m^\dagger e^{i\delta_m t_2} + a_m e^{i\delta_m t_2}, a_{m'}^\dagger e^{i\delta_{m'} t_1} + a_{m'} e^{i\delta_{m'} t_1}] \\
 &= i \sum_{j,j'=1}^2 \sum_{m=1}^2 \frac{\eta_{j,m}\eta_{j',m}\Omega^2}{4} \sigma_x^j \sigma_x^{j'} \int_0^\tau dt_2 \int_0^{t_2} dt_1 \sin[\delta_m(t_2 - t_1)] \\
 &= i \sum_{j,j'=1}^2 \sum_{m=1}^2 \frac{\eta_{j,m}\eta_{j',m}\Omega^2}{4} \left( \frac{\tau}{\delta_m} - \frac{\sin(\delta_m \tau)}{\delta_m^2} \right) \sigma_x^j \sigma_x^{j'} \\
 &= -i\theta_{1,2}(\tau) \sigma_x^1 \sigma_x^2, \tag{5-12}
 \end{aligned}$$

where,

$$\theta_{1,2}(\tau) = -2 \sum_{m=1}^2 \frac{\eta_{1,m}\eta_{2,m}\Omega^2}{4} \left( \frac{\tau}{\delta_m} - \frac{\sin(\delta_m \tau)}{\delta_m^2} \right). \tag{5-13}$$

All self-interaction terms vanish because of  $\sigma_x^j \sigma_x^j = \mathbb{I}$ , leading to constant phases which are ignored. The factor of two in the coupling strength  $\theta_{1,2}$  is due to the symmetrical contributions from  $\sigma_x^1 \sigma_x^2$  and  $\sigma_x^2 \sigma_x^1$ . The qubit-qubit coupling term here provides possibilities to entangle different qubits. Note that, The even higher-order integrals vanish because of  $[H_{\text{SDF}}(t_3), [H_{\text{SDF}}(t_2), H_{\text{SDF}}(t_1)]] = 0$ .

### 5.1.3 Two-qubit entangling gate in a two-ion chain

By inserting Eq. (5-10) and Eq. (5-12) into Eq. (5-9), we finally obtain the simplified evolution operator,

$$U(\tau) = \exp \left[ \sum_{j=1}^2 \sum_{m=1}^2 \left( \alpha_{j,m}(\tau) a_m^\dagger - \alpha_{j,m}^*(\tau) a_m \right) \sigma_x^j - i\theta_{1,2}(\tau) \sigma_x^1 \sigma_x^2 \right]. \tag{5-14}$$

In order to have a pure qubit-qubit coupling, the qubit-motion should be disentangled at the time  $\tau$ , indicating that  $\alpha_{j,m}(\tau)$  should be zero for any  $j, m$ . According to Eq. (5-11), these are equivalent to  $\delta_m \tau$  is an integer multiple of  $2\pi$  for any  $m$ . For a two-ion chain, above conditions can be satisfied by setting  $\mu = (\nu_1 + \nu_2)/2$  and  $\tau = 2n\pi \times 2/(\nu_1 - \nu_2)$  (assuming  $\nu_1 > \nu_2$ ) where  $n$  belongs to the positive integers, as shown in Fig. 5.1. The coupling strength turns out to be,



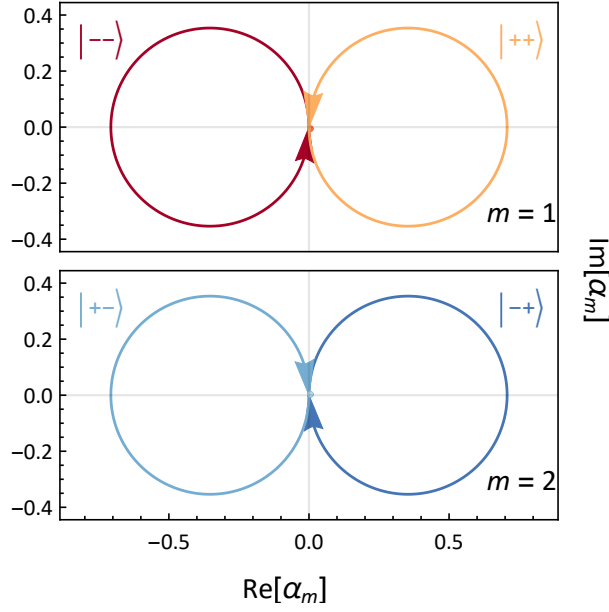


Figure 5.1 State-dependent displacement in phase space. Here  $\alpha_m = \langle \alpha_{1,m} \sigma_x^1 + \alpha_{2,m} \sigma_x^2 \rangle$  and  $\langle \cdot \rangle$  denotes the projection to the qubit-state.  $|\pm\rangle$  are the eigenstates of the  $\sigma_x$  operator. As we can see, for the 1st mode (COM mode), the force pushes the two ions in the same direction; therefore, only the  $|\pm\pm\rangle$  states can be driven. On the contrary, for the 2nd mode (zigzag mode), the ions are driven oppositely, and then the  $|\pm\mp\rangle$  states are coupled. In order to satisfy the requirements of  $\alpha_{j,m}(\tau) = 0$  for any  $j, m$ , the trajectories for all the qubit-states should be enclosed at the time  $\tau$ .

$$\theta_{1,2} = -\frac{n\pi\Omega^2}{\delta_1} \left( \frac{\eta_{1,1}\eta_{2,1}}{\delta_1} + \frac{\eta_{1,2}\eta_{2,2}}{\delta_2} \right) \approx -\frac{2n\pi\eta_{1,1}^2\Omega^2}{\delta_1^2}. \quad (5-15)$$

The last simplification is due to the relations of  $\delta_1 = -\delta_2$  and  $\eta_{1,1} = \eta_{2,1} \approx \eta_{1,2} = -\eta_{2,2}$ . The final evolution operator reveals the two-qubit entangling operation written as,

$$\text{XX}_{1,2}(\theta_{1,2}) = U(\tau) = \exp \left[ -i\theta_{1,2} \sigma_x^1 \sigma_x^2 \right], \quad (5-16)$$

which is one of the Ising-type gates and is denoted as the XX-gate. The two-body coupling strength can be tuned by changing the power of driving laser ( $\Omega$ ).

In the quantum computing community, the Controlled-NOT (CNOT) gate is the more well-known two-qubit gate. The XX-gate can be transformed into the CNOT gate by being sandwiched by several single-qubit rotations<sup>[16]</sup>, as shown in Fig. 5.2. In this sense, we always choose arbitrary single-qubit rotations and two-qubit XX gates, instead of CNOT gates, as our universal gate set in the trapped-ion platform.

One of the most important functions of the XX-gate is to prepare entangled states, as

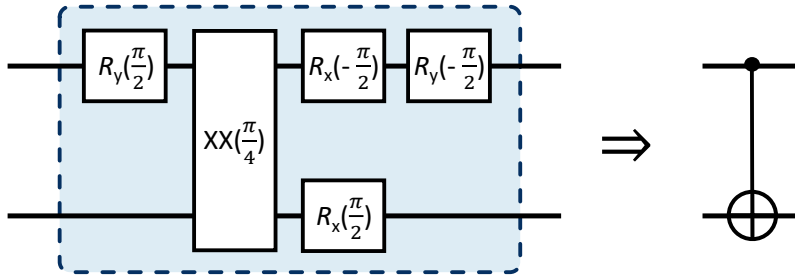


Figure 5.2 Construct a CNOT gate with a XX gate and several single-qubit gates. Two circuits shown in the figure are equivalent except a global phase shift.

shown in the following equation,

$$XX(\theta)|00\rangle = \cos\theta|00\rangle - i\sin\theta|11\rangle. \quad (5-17)$$

When choosing  $\theta$  to be  $\pm\pi/4$ , the prepared states are the maximally entangled states,  $(|00\rangle \mp i|11\rangle)/\sqrt{2}$ , which are equivalent to the Bell states. The state fidelities of these states are always used to characterize the performance of XX-gates. As shown in Fig. 5.3, we experimentally apply a  $XX(-\pi/4)$  gate and then measure the population of the final state. We can observe the domain population occupying the states of  $|00\rangle$  and  $|11\rangle$ .

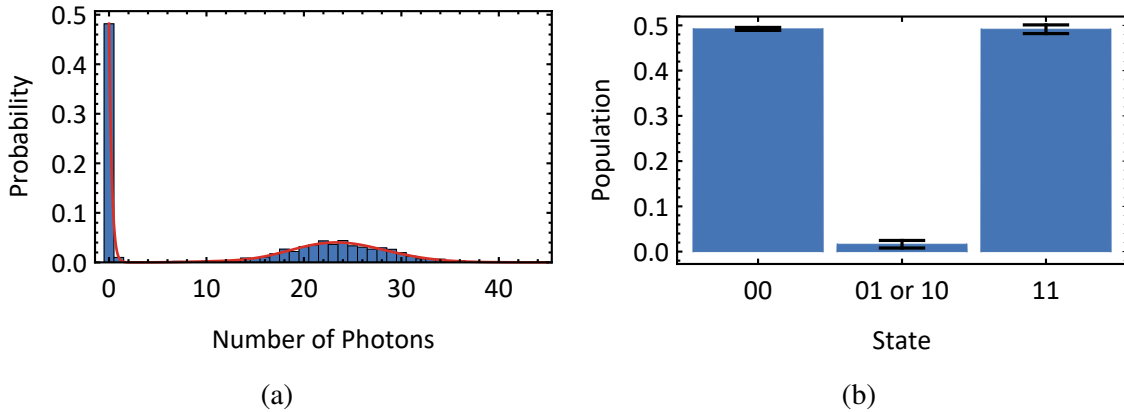


Figure 5.3 Population measurement of prepared entangled state. (a) Probability distribution of the number of incident photons during the detection process. Here we use the normal PMT as our detecting device, and the distribution is obtained after 3000 times repetition. The final distribution is treated as the sum of three Poisson distributions with the average photon numbers of  $n_0 \approx 0$ ,  $n_1$  and  $n_2 \approx 2n_1$ , corresponding to the cases of no bright ion ( $|00\rangle$ ), single bright ion ( $|01\rangle$  or  $|10\rangle$ ) and two bright ions ( $|11\rangle$ ), respectively. (b) Population on each qubit state. By fitting the distribution with the sum of three Poisson distributions, we can obtain the weight of each distribution (solid red line in (a)), which is treated as the population of the corresponding qubit state. The fitting results here indicate  $(98.3 \pm 0.01)\%$  population occupied in the states of  $|11\rangle$  and  $|00\rangle$ .

To determine the state fidelity defined as,

$$\mathcal{F} = \text{Tr} [|\psi_{\text{id}}\rangle\langle\psi_{\text{id}}|\rho_{\text{exp}}] = \frac{\rho_{00} + \rho_{11} + |\rho_{01}| + |\rho_{10}|}{2}, \quad (5-18)$$

where  $|\psi_{\text{id}}\rangle$  is the ideal maximally entangled state and  $\rho_{\text{exp}}$  is the density matrix of the prepared state, we still need to quantify the correlation between the states  $|00\rangle$  and  $|11\rangle$ . A standard method is applying  $\pi/2$ -rotations along the  $\phi$ -axis to both qubits, as shown in Fig. 5.4 (a). The parity of the final state, defined as  $\langle(-1)^{\sigma_z^1\sigma_z^2}\rangle = P_{00} + P_{11} - P_{10} - P_{01}$ , would oscillate with the value of  $\phi$ , while the contrast of the oscillation indicates the value of  $|\rho_{10}|$ , as shown in Fig. 5.4. Here  $\langle\cdot\rangle$  denotes the average over the final state, and  $P_i$  is the population on the  $|i\rangle$  state.

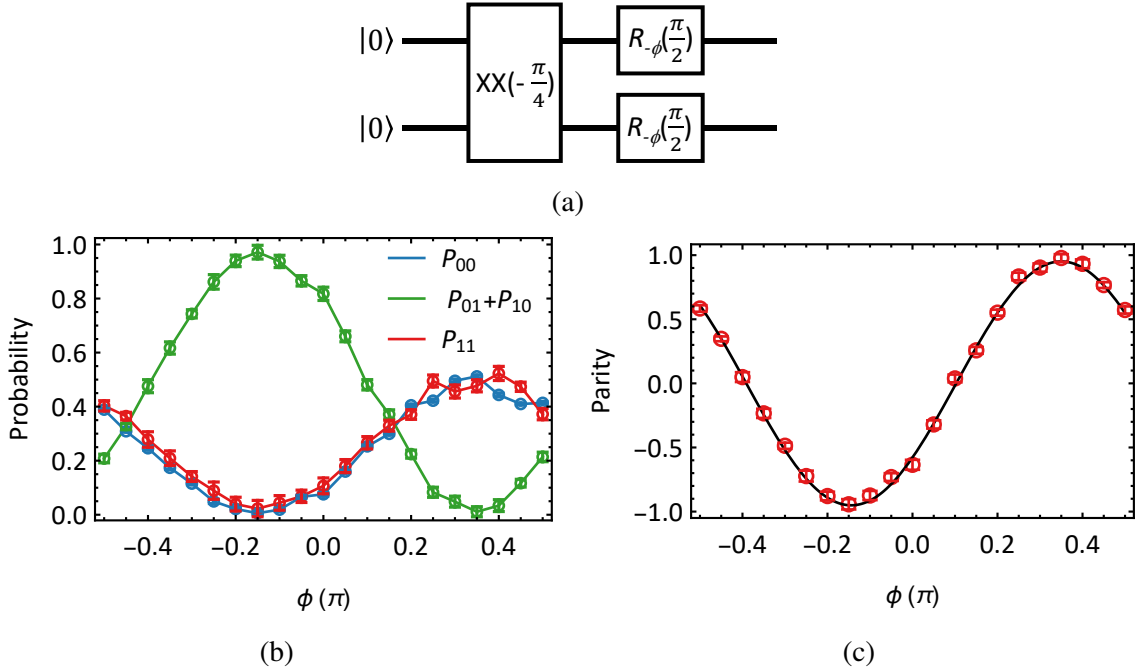


Figure 5.4 Correlation measurement and parity oscillation. (a) Circuit of measuring the state correlation. Note that in our experimental measurement, the single-qubit rotations are along the  $-\phi$ -axis, while the contrast of the parity oscillation would not be affected. (b) Population of the final state with different  $\phi$ . For each point, we repeat 500 times and then obtain the population on different states by fitting the probability distribution of the number of incident photons. (c) Parity oscillation obtained from the data in (b). All the red circles refer to the experimental results, while the solid black line is the fitting result. Here the contrast of the oscillation is  $(95.0 \pm 0.01)\%$ , indicating the state fidelity of  $(96.7 \pm 0.01)\%$  at that time.

### 5.1.4 Further discussion

#### Two-qubit entangling gate in a $N$ -ion chain

Now we consider realizing two-qubit entangling gates on an ion-chain with  $N$  ions ( $N > 2$ ). Note that, all-to-all connections between each ion and each collective motional mode lead to all-to-all connectivity among all ion qubits. Therefore, we can directly apply two-qubit gates on arbitrary qubit-pair even if they are not adjacent in physical space, and this feature is known as full-connectivity<sup>[16,135]</sup>. However, the challenging part is that the number of normal modes increases linearly with the number of ions. By applying state-dependent forces on the target two ions (assuming we have the individual controllability on each ion), we have to decouple the ions from all their motional modes at the gate time  $\tau$  to achieve the pure qubit-qubit interaction as shown in Eq. (5-16), which indicates the constraints of,

$$\alpha_m^{\text{scaled}} = \frac{\alpha_{j,m}(\tau)}{\eta_{j,m}} = -i \int_0^\tau \frac{\Omega}{2} e^{i\delta_m t} e^{-i\phi_p} = 0, \quad (5-19)$$

for  $m = 1, 2, \dots, N$ . These constraints are easy to satisfy when  $N = 2$  but become a tricky problem when more modes get involved, because the  $\delta_m$  with different indexes are always irrational to each other.

Several schemes are developed since the first proposal in 2006<sup>[136-137]</sup>. The main idea is utilizing modulated state-dependent force to drive target qubits, resulting in the modified constraints of,

$$\alpha_m^{\text{scaled}} = -i \int_0^\tau \frac{\Omega(t)}{2} e^{i\delta_m(t)t} e^{-i\phi_p(t)} = 0. \quad (5-20)$$

This can be achieved by changing the parameters of the laser fields in time, including either power ( $\Omega$ )<sup>[138]</sup>, frequency ( $\delta_m$ )<sup>[139]</sup>, phase ( $\phi_p$ )<sup>[140-141]</sup>, or their combinations. Such modulated forces provides enough degree of freedoms to close all the motional trajectories in the phase space with much more complex shapes instead of the simple circle shown in Fig. 5.1. Meanwhile, the modulated pulses can be designed to be robust to system noises<sup>[139-143]</sup>, including such as the drifting in trap frequencies, the heating of motional modes, which makes gate operations more practical.

#### Off-resonant coupling to carrier transition

Here, we had better review the Hamiltonian of the state-dependent force. In the derivation of Eq. (5-7), we neglect the off-resonant coupling to the carrier transition in

the sideband Hamiltonian by assuming that  $\Omega \ll \mu$ . However, this assumption is not always true, especially when we pursue a fast gate operation, which requires pretty large  $\Omega$ . Therefore, the fast oscillation term of the carrier should be included, which modifies the state-dependent form of Eq. (5-7) to be,

$$\begin{aligned} H_{\text{SDF}}^{\text{Full}} &= H_c + H_{\text{SDF}} \\ &= \sum_j \Omega \cos(\mu t) \sigma_y^j + \sum_{j,m} \frac{\eta_{j,m} \Omega}{2} (a_m^\dagger e^{i\delta_m t} + a_m e^{-i\delta_m t}) \sigma_x^j. \end{aligned} \quad (5-21)$$

Note that, the term of  $H_c$  in Eq. (5-21) is proportional to  $\sigma_y^j$ , while  $H_{\text{SDF}} \propto \sigma_x^j$ . Therefore, these two parts yield a non-zero commutator of  $[H_{\text{SDF}}, H_c] \propto \sigma_z^j$ , which make the calculation of Eq. (5-8) a complicated problem because  $[H_{\text{SDF}}^{\text{Full}}(t_3), [H_{\text{SDF}}^{\text{Full}}(t_2), H_{\text{SDF}}^{\text{Full}}(t_1)]]$  is not zero anymore.

This trouble is still unsolved. Therefore, no  $\sigma_x \sigma_x$ -type ultra-fast gate has been demonstrated. However, the operation duration of a  $\sigma_z \sigma_z$ -type gate has already reach 480 ns<sup>[59]</sup>, which is comparable to solid systems. Because the frequencies of driving a  $\sigma_z$ -dependent force can be much far away from the carrier transition, the off-resonant coupling is negligible even in the fast gate region, while a Zeeman qubit is required<sup>[144]</sup>. Moreover, in Ref. [59], the researchers also point out that the high-order sideband transitions also should be considered due to the breakdown of the Lamb-Dicke approximation. To accelerate  $\sigma_x \sigma_x$ -type gates, several methods like utilizing standing-waves or near-field oscillating magnetic fields are under-exploring, in which the amplitude of the driving fields can vanish while the gradient remains. Note that, in Ref. [145], the authors mention that the error from the carrier term can be effectively suppressed when the modulating pulse satisfies  $\int_0^t \Omega(t) \approx 0$ . For now, although we limit ourselves in the slow-gate region, the open question of fast  $\sigma_x \sigma_x$ -type gates is worthwhile for further researches.

## 5.2 Individual laser addressing on five ion qubits

### 5.2.1 Brief introduction to multiple qubits control

It is time to move to hardware levels. To realize a universal quantum computing system on a linear ion-chain, we should have capabilities of achieving single-qubit rotations and two-qubit XX-gates on arbitrary single-qubit and qubit-pair, respectively. Therefore, we need to distinguish each ion and to apply driving fields onto target qubits.

Because ions are always spatially crowded, we can separate all the qubits in the

frequency domain. This scheme can be achieved by employing Zeeman qubits and applying a static magnetic with a spatial gradient<sup>[146-147]</sup>. When a certain qubit is driven resonantly, others that are not desired to be manipulated would be hidden from the control field. Moreover, the sizeable magnetic gradient offers the possibility of exciting the ion-motion coupling even by the long-wavelength microwave. However, the additional phases induced by off-resonate coupling on all other qubits can not be ignored if we apply the long-depth circuits, and high stability of the control field is required if we want to calibrate them. Meanwhile, the Zeeman qubits may suffer from the short coherence time due to the magnetic fluctuation, while a "engineered clock qubit" is proposed and implemented to overcome this shortage<sup>[64-65]</sup>.

Another scheme is spatially resolving each qubit by tightly focusing each beam in an array of the driving laser beams onto each ion in an ion-chain. By independently controlling each driving beam, we can individually manipulate each qubit. Therefore, this setup is usually called as the individual addressing system. In some realizations, the individual beams, which are perpendicular to an ion-chain, execute arbitrary single-qubit rotations or shelve part of qubits to their metastable states when a global entangling operation is applied by the beam which is parallel to the ion-chain<sup>[57]</sup>. While in some setups, the individual beams are employed to execute the whole universal gate set<sup>[16-17]</sup>. Here we choose the final one as our solution to construct a fully controllable quantum computing system, which would be introduced in the following content.

### 5.2.2 Design of the individual addressing system

In practice, the alignment of the whole individual laser addressing system is shown in Fig. 5.5. To drive the two-photon stimulated Raman transition, the pulsed laser is divided into two paths, which are denoted as the individual part and the global part, by a PBS. The individual part is modularized by coupling to a high-power photonic-crystal fiber (provided by NKT Photonics, while the hydrogen loading is done by ourselves). The global Raman beam, which is the  $-1$ st diffractive order from a conventional single-channel AOM, is designed to cover all the whole ion-chain. With the help of two cylinder-lens, which are perpendicular to each other, the global Raman beam is focused at the ion-chain position into an elliptical Gaussian beam, with waists of about  $30 \mu\text{m}$  along the ion-chain and about  $5 \mu\text{m}$  in the perpendicular direction. The delay line is used to balance the length difference between the global part and the individual part. Note that, to compensate for

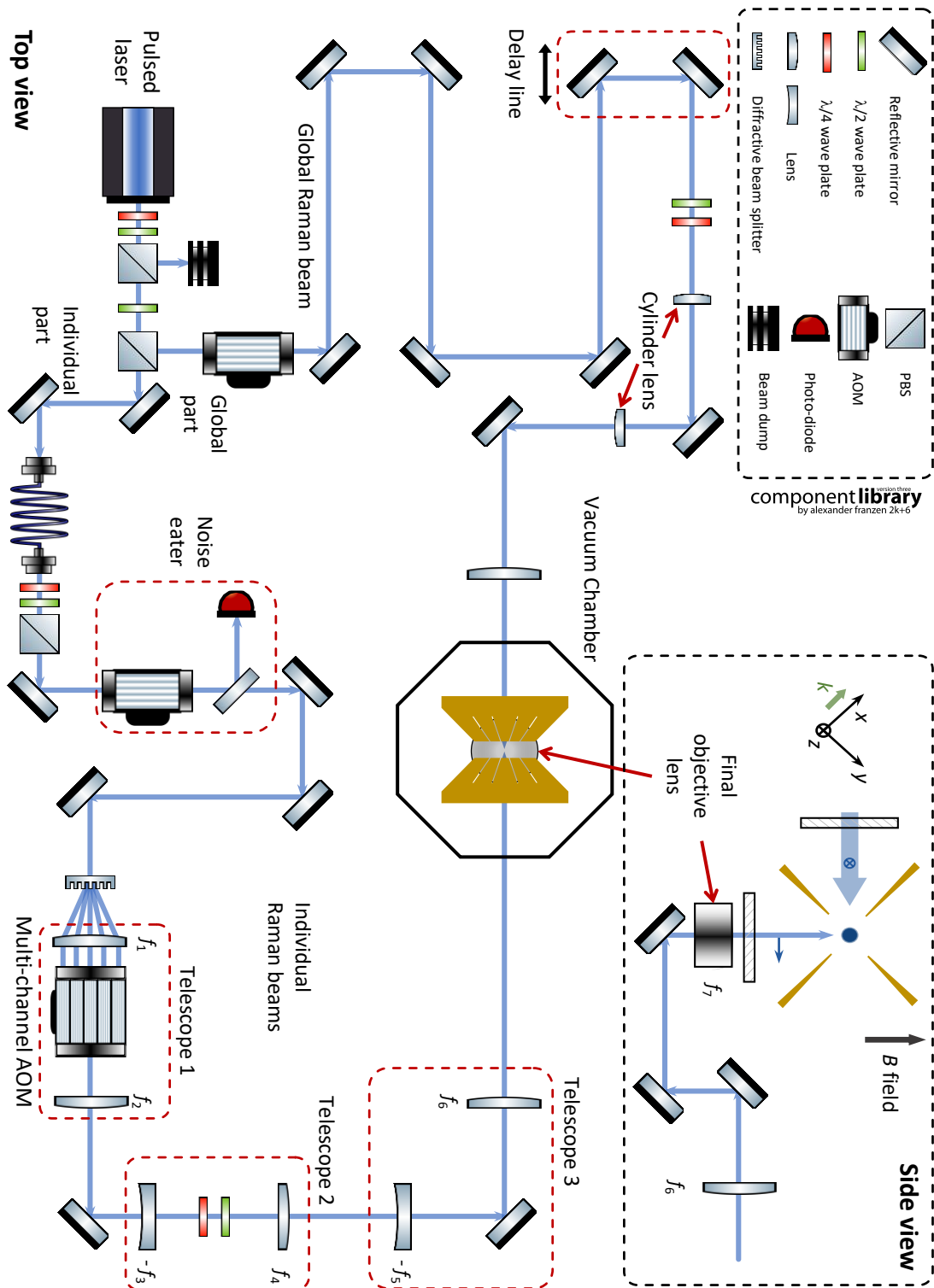


Figure 5.5 Alignment of Raman lasers. Part of the optical elements are not shown in the figure.

the optical path induced by the fiber in the individual part, the total length of the global Raman path is around 3 m. Therefore, to reduce the phase noise due to the airflow, the whole Raman system is covered by several designed boxes.

The more complicated individual part can be divided into three sections, including generating an array of almost identical beams, providing independent control ability, and focusing at the ion-chain position. As shown in Fig. 5.5, after going through a noise eater, which is used to stabilize the laser power, the laser beam first passes a DOE, specifically a diffractive beam splitter (HOLO/OR MS-499-U-Y-X). This element is a transmissive binary phase grating, which is designed to uniformly distribute the most of the laser power ( $\sim 75\%$ ) to the  $\{-2, -1, 0, +1, +2\}$  diffractive orders. Here the diffractive angle  $\vartheta_d$  is around 6.08 mrad at the wavelength of 375 nm. Before going through a multi-channel AOM (Gooch&Housego 97-02411-03, 5 channels), a lens with the proper focal length ( $f_1 \sim 146$  mm) is placed to make the five beams parallel to each other, and then the spacing of the beams matches that of the AOM channels which is around 0.035 inch, as shown in Fig. 5.6 (c). The  $-1$ st orders from all the channels work as the individual Raman beams. Moreover, by employing a multi-channel AWG (SPECTRUM DN2.662-08, 8 channels) to generate RF signals to each AOM channel, the frequency, power, and optical phase of each individual Raman beam can be independently controlled.

To achieve a tightly focusing at the positions of ions, we employ a multi-stage telescope system to amplify the size of the individual beams and then focus them with an objective lens with a quite short work distance, as shown in Fig. 5.5 and Fig. 5.6 (a). To simplify the analysis, we treat each optical lens as the ideal thin one. The individual beam along the chief optical axis (0th diffractive order) is used to estimate the size of the Gaussian beam at the ion position, while the propagating trajectories of all the diffractive beams are tracked to obtain the spacing of the final beam points by utilizing the geometric optical method, as illustrated in Fig. 5.6. The whole amplification system includes three sub-telescopes, providing a total magnification of,

$$M_t = \frac{f_2}{f_1} \times \frac{f_4}{-f_3} \times \frac{f_6}{-f_5}, \quad (5-22)$$

where  $f_i$  is the focal length of each optical lens. With the initial Gaussian beam size of  $\omega_0$  at the DOE position, the beam is expanded to the size of  $\omega'_0 = M_t \omega_0$  after the 6th lens ( $f_6$ ), while the diffractive angle is suppressed from  $\vartheta_d$  to  $\vartheta'_d = \vartheta_d / M_t$ . After focusing by



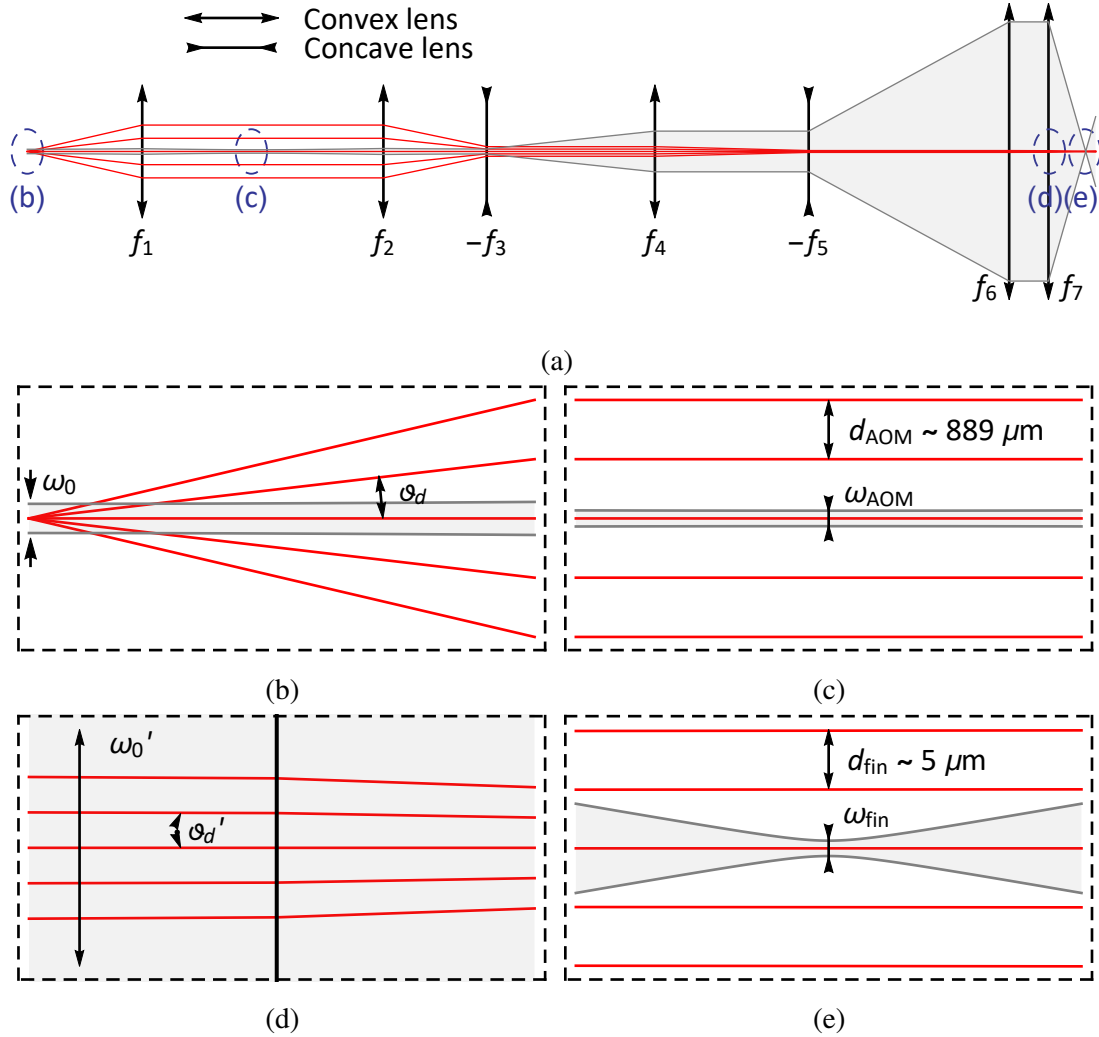


Figure 5.6 Telescope system to achieve tightly focusing. (a) Overall of the three-stage telescope system. The pairs of  $\{f_1, f_2\}$ ,  $\{f_3, f_4\}$  and  $\{f_5, f_6\}$  form the first, the second and the third sub-telescopes, respectively. The concave lenses here are utilized to save the optical length. (b) Starting point of the telescope system. After passing the DOE, the five almost identical beams propagate with the diffractive angle of  $\vartheta_d$ . We assume that the waist of the beam is at the position of the DOE. (c) Place to insert the multi-channel AOM. The five beams are adjusted with a lens to be parallel propagation, and the spacing matches that of the AOM. (d) End of the telescope system. The size of the beam is expanded to be  $\omega_0'$ , while the diffractive angle is reduced to be  $\vartheta_d'$ . (e) Final focused individual beams. The spacing of the final focused position is designed to be around  $5 \mu\text{m}$ . Here, the waists of the individual beams are pretty small, resulting in a pretty short Rayleigh range. The beams would quickly diverge after the focused position.

the final objective lens, the size of each beam can be estimated as,

$$\omega_{\text{fin}} \approx \frac{\lambda f_7}{\pi \omega'_0} = \frac{\lambda f_7}{\pi M_t \omega_0}, \quad (5-23)$$

with a spacing of

$$d_{\text{fin}} \approx f_7 \vartheta'_d = \frac{f_7 \vartheta_d}{M_t}. \quad (5-24)$$

Note that, for an ideal situation, the ratio between the final beam waist and the beam-spacing,

$$\frac{\omega_{\text{fin}}}{d_{\text{fin}}} = \frac{\lambda f_7}{\pi M_t \omega_0} \times \frac{M_t}{f_7 \vartheta_d} = \frac{\lambda}{\pi \omega_0 \vartheta_d}, \quad (5-25)$$

is determined by the beam waist at the DOE position if we fix the parameters of the telescope system. To suppress the crosstalk of the individual beams to their nearby ion qubits, we expect above ratio to be as small as possible. However, such tiny size of the focused beam requires pretty high N.A. of the final objective ( $f_7$ ) and careful compensation for optical aberrations.

As a tradeoff, we expect to achieve the final beam waist to be around  $0.7 \mu\text{m}$ , while the beam spacing is desired to be  $5 \mu\text{m}$ . In this situation, the amplitudes of electric fields spread to the nearby ions are estimated to be  $\exp(-5.0^2/0.7^2) \sim 10^{-25}$ . We choose a final objective lens (RONAR-SMITH 355nmFL47Q) that has an effective focal length around 47 mm and N.A around 0.25, which provides a resolution of around  $0.61\lambda/2\text{N.A.} \approx 0.45 \mu\text{m}$ . The total magnification of the telescope system  $M_t$  is expected to be around 58 by using the lenses listed in Tab. 5.1. Those lenses are selected by the simulation in Zemax to minimize the accumulated optical aberrations.

Table 5.1 Lenses of telescope system

Lens index	Focal length (mm)	Details
$f_1$	146.2	Doublets of Thorlabs LA4579-UV
$f_2$	160.6	Thorlabs LA1708-A and LA1464-A
$f_3$	-29.2	Thorlabs LC4252-UV
$f_4$	243.1	Thorlabs LA4158-UV
$f_5$	-47.5	Thorlabs LC4888-UV and LF4938-UV
$f_6$	302.5	Thorlabs AC508-300-A

The finale focused individual beams achieved in the experiment are shown in Fig.

5.7. Because the objective lens of individual addressing and that of imaging systems are opposite to each other, we can check the quality and size of the beams on the EMCCD. By directly obtaining the position of each individual beam on the camera, we estimate the spacing of the nearest beams to be around  $4.75 \mu\text{m}$  in practice. The waist of each beam is around  $1 \mu\text{m}$ , and we suspect the difference to the theoretical value is due to the uncompensated optical aberrations. In the experimental system, the final objective lens is placed on a five-axis stage (three translational axes two rotational axes) and carefully adjusted, because it is the most sensitive element to introduce huge aberrations. However, in Fig. 5.7, we can still observe the coma aberration from the beam spots on both sides. The spherical aberration is also much larger than the expectation, resulting in optical spillovers to the nearby ions around 1-3%. Because the effective Rabi frequency of the stimulated Raman transition is proportional to the multiplication of the electric field amplitudes of the global Raman beam and the individual beam,  $\Omega \propto E_{\text{global}}E_{\text{ind}}$ , the spillovers turn into crosstalks in quantum operations.

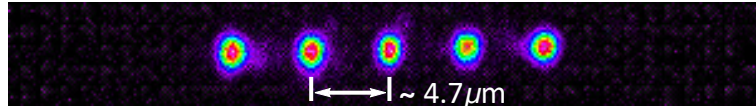


Figure 5.7 Focused individual beams imaged on the EMCCD.

In addition, in the inset figure of Fig. 5.5, we show the geometric configuration of the Raman laser beams. The global beam goes through a side viewport, while the individual beams pass the bottom re-entrant viewport. The global beam and the individual beams intersect each other perpendicularly at the ion chain, resulting in the effective wave vector along the radial  $x$ -direction. Such geometry makes it possible to only drive the normal modes in  $x$ -direction, simplifying the pulse optimization when we apply entangling gates. The beams are polarized linearly, perpendicular to each other, while the static magnetic field is applied along the direction of the individual beams.

### 5.3 Initialization and readout on multiple qubits

Up to now, we do not require independent initialization or detection of multiple qubits, compared with individually coherent control on each ion. Therefore, it is straightforward to extend state initialization&detection to the multi-qubit case. We briefly introduce each part as follows.

### 5.3.1 Multiple qubits initialization

As we have already discussed in Sec. 3.1, single-qubit state initialization is achieved by the standard optical pumping techniques. To extend it to the multi-qubit case, we can broaden the optical pumping beam to cover the whole ion-chain and pump all the ion qubits to the  $|0\dots 0\rangle$  state simultaneously. Therefore, the duration of this process does not increase with the scale of the system.

For motional state initialization, we can also broaden the beam for Doppler cooling to cool the motion of the ion-chain to the Doppler cooling limit. However, to guarantee the fidelity of single-qubit rotations and two-qubit entangling gates, we also demand the ground-state cooling of motional states. Because the collective motional modes are separated in the frequency domain and the conventional sideband cooling has a pretty narrow bandwidth, the problem of multi-ion ground-state cooling becomes less straightforward. In principle, We can alternately drive red sideband transitions of different modes to cool down each mode one by one. The duration of the multi-mode sideband cooling would increase more than linearly ( $N^{3/2}$ ) with the number of the ions  $N$  if we fix the power of the driving laser beam. Here, the factor of  $N$  comes from the number of the motional modes, while the factor of  $N^{1/2}$  is due to the decay of the scale Lamb-Dicke parameters.

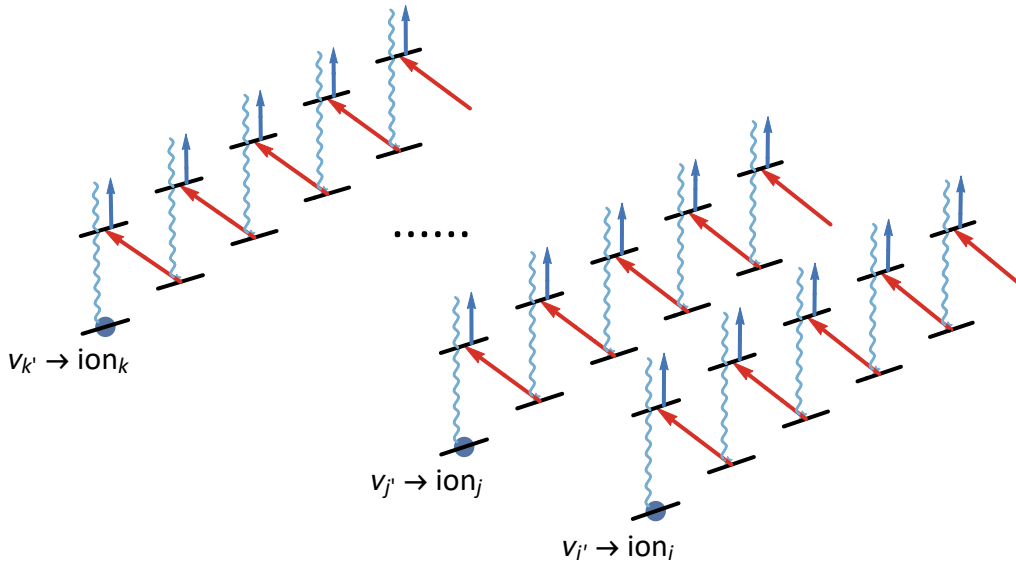


Figure 5.8 Simultaneous sideband cooling of multiple motional modes.

Fortunately, with the help of the individual addressing system, we can apply the multi-mode sideband cooling simultaneously, as shown in Fig. 5.8. The red sideband

transition of each mode is mapped on each ion to reduce one quanta phonon of each mode, and then the optical pumping is applied to the whole ion-chain to reset the state of the qubits. Therefore, the duration of the ground state cooling would be proportional to  $\sqrt{N}$ . Moreover, we must carefully arrange which ion to use to cool which mode. For example, in a three-ion system, the 2nd breathing mode is decoupled from the 2nd ion, as illustrated in Fig. 2.4; therefore, we can not utilize this ion to cool down the 2nd mode.

### 5.3.2 Spatially resolved detection

For multiple ions detection, we have already demonstrated one of the methods in Sec. 5.1, when we characterize the fidelity of the Bell state prepared by the two-qubit entangling gate. Here we discuss to extend this method to the multi-qubits case. After repeating a specific experimental sequence many times, we would obtain a distribution of the number of incident photons. If we can ignore the side-effects from the off-resonant coupling of the detection beam, the distribution should follow the form of,

$$\sum_{N_b=0} A_{N_b} \text{Pois}_{N_b}(n) = \sum_{N_b=0} A_{N_b} \frac{(\bar{n}_{N_b})^n e^{-\bar{n}_{N_b}}}{n!}, \quad (5-26)$$

where  $\text{Pois}_{N_b}(n)$  is the Poisson distribution,  $N_b$  is the number of bright ions and  $\bar{n}_{N_b} \approx N_b \bar{n}_1$  is the corresponding average number of incident photons. The weights  $A_{N_b}$  are fitted by experimental results to estimate the populations of the measured state. This method has several shortages. First, we can only know how many ions are in the  $|1\rangle$  state instead of which ions are in this state, as shown in Fig. 5.3. Then, we can not apply the single-shot measurement. In the single-qubit situation, the single-shot measurement works because of a tiny overlap between the Poisson distributions of the dark ( $|0\rangle$ ) and single-bright ( $|1\rangle$ ) event, as shown in following,

$$\sum_{n=0}^{\infty} \text{Min} [\text{Pois}_0(n), \text{Pois}_1(n)] < 10^{-3}, \quad (5-27)$$

Here the corresponding average photon numbers are estimated to be  $\bar{n}_0 \approx 0.05$  and  $\bar{n}_1 \approx 10$ . Therefore, we can use a fixed threshold to determine the projected state in a high fidelity, as we discussed in Sec. 3.1. However, as the number of ions increasing, the overlap,

$$\sum_0^{\infty} \text{Min} [\text{Pois}_{N_b}(n), \text{Pois}_{N_b+1}(n)], \quad (5-28)$$

quickly increases, as shown in Fig. 5.9. This is because the signal ratio drops from  $\bar{n}_1/\bar{n}_0 > 10^2$  to  $\bar{n}_{N_b+1}/\bar{n}_{N_b} < 2$  when  $N_b \geq 1$ . The threshold method suffers from serious detection errors and can not work. Meanwhile, the fitting method would also fail due to the significant overlap between different distributions.

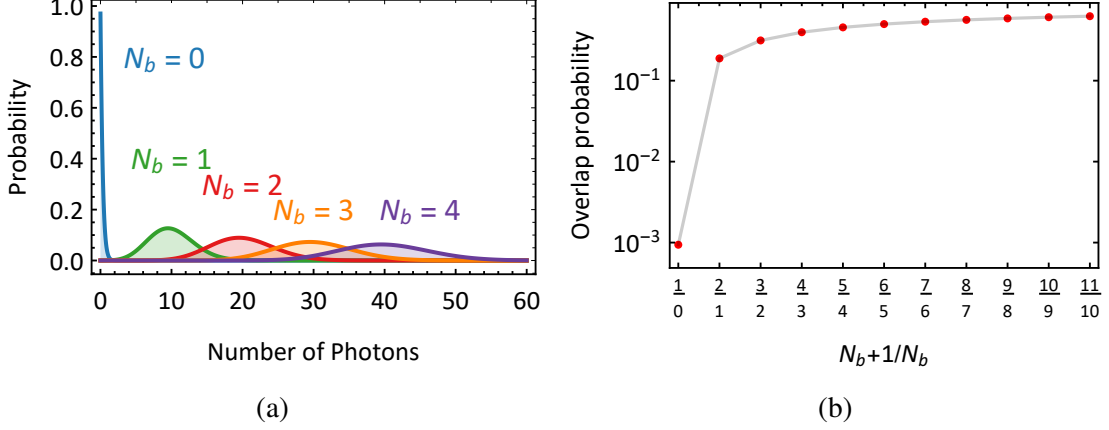


Figure 5.9 Probability distribution of the number of photons during multi-ion detection and their overlap.  $N_b$  is the number of the bright ions, and the effect of the off-resonant coupling is neglected here.

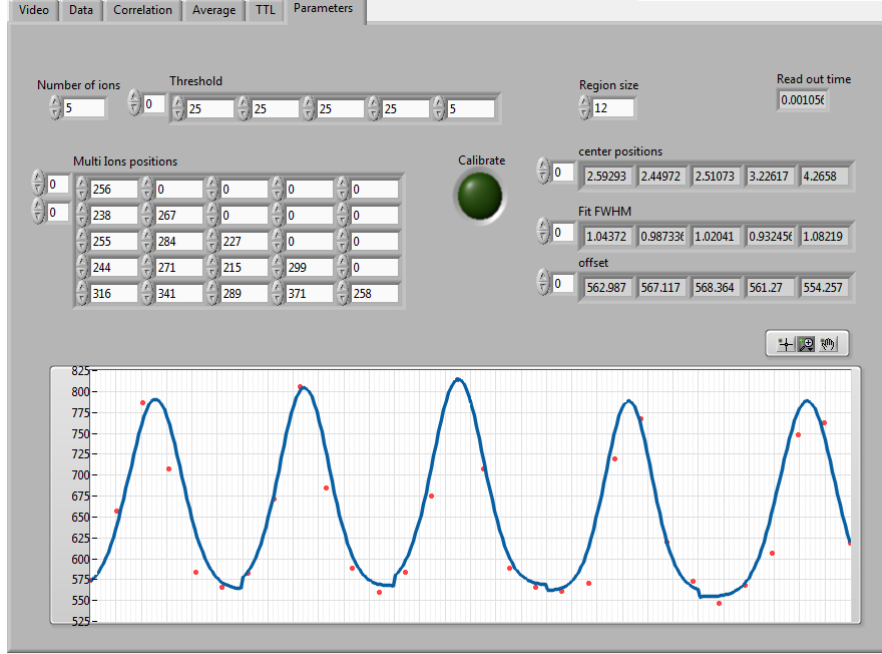
### Detection with EMCCD

To distinguish multi-qubit projected states in a single shot, we replace the detection device with the EMCCD. The chip of our EMCCD contains  $512 \times 512$  active pixels and the size of each pixel is  $16 \mu\text{m} \times 16 \mu\text{m}$ . The positions of all the ions can be naturally resolved, as shown in Fig. 5.10 (a). To detect the state of each qubit, we select several regions of interest (ROI) which contain one ion in each ROI, and then use the brightness (counts) of each pixel to determine the projected state.

In principle, we can sum the counts of all the pixels in each region, and then use the threshold method to estimate the projected state of each ion. However, the counts contributed from the nearby ROIs and pretty high background counts would degrade the detection fidelity. To overcome these problems, we fit the profile of each imaged ion with a Gaussian distribution and then utilize the fitted height of the distribution to determine qubit states<sup>[148]</sup>. The data of each ROI is summed vertically; therefore, we can apply a one-dimensional Gaussian fitting. We first pre-calibrate the positions and sizes of all the ions by shining the detection laser to the ion-chain and exposing them to the camera for a



(a)



(b)

Figure 5.10 Labview interface for detection with the EMCCD. Here, we show the calibration of the positions and the sizes for five ions.

long time. The data of each ROI is fitted with the form of,

$$f_i^{\text{cal}}(x) = A_i \exp \left[ -\frac{(x - x_i)^2}{2\sigma_i^2} \right] + B_i, \quad (5-29)$$

where  $A_i$ ,  $B_i$ ,  $x_i$  and  $\sigma_i$  are the fitting parameters for the  $i$ -th ion. Fig. 5.10 (b) shows the profiles of five ions during the calibration process. After pre-calibration, the position ( $x_i$ ), size ( $\sigma_i$ ) and offset ( $B_i$ ) of each ion are fixed to be the calibrated results,  $x_i^{\text{cal}}$ ,  $\sigma_i^{\text{cal}}$  and  $B_i^{\text{cal}}$ , respectively. The form of

$$f_i^{\text{exp}}(x) = A'_i \exp \left[ -\frac{(x - x_i^{\text{cal}})^2}{2(\sigma_i^{\text{cal}})^2} \right] + B_i^{\text{cal}}, \quad (5-30)$$

is utilized to fit the data obtain in the experiment. Here only the height of the distribution,  $A'_i$ , is the fitting parameter, and its value is compared with a given threshold to determine the projected state.

To characterize the fidelity of single-qubit detection, we obtain the histogram dis-

tributions of the fitting height by preparing the initial  $|0\rangle$  or  $|1\rangle$  state. The experimental results are shown in Fig. 5.11. Due to a low quantum efficiency of the EMCCD, the detection duration is extended to  $800 \mu\text{s}$ . Therefore, the effect of the off-resonant coupling from the detection beam can not be ignored. In the distribution of the  $|1\rangle$  state, the tail near zero is much higher than the standard Poisson distribution. The off-resonant coupling, together with the low signal-to-noise ratio of the EMCCD, degrade the fidelity of single-qubit detection to around 96%.

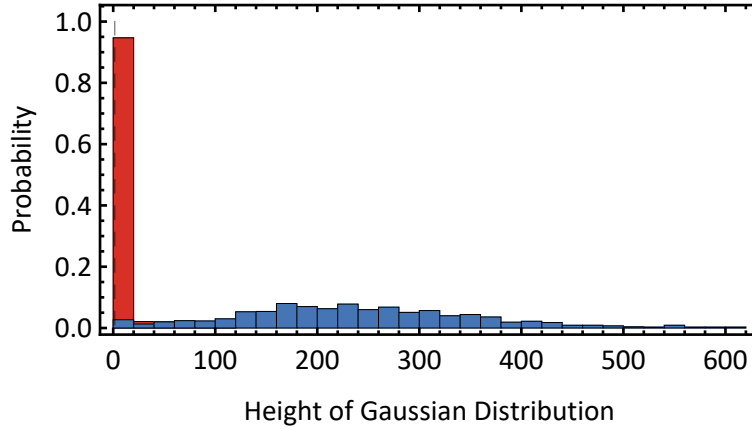


Figure 5.11 Probability distribution of the fitted height of the Gaussian distribution. The red data represents the distribution of the initial  $|0\rangle$  state while the blue one represents the results of the  $|1\rangle$  state.

For now, we do not have a clear idea to improve detection fidelity. Instead, we utilize the method introduced in Ref. [149] to correct the detection errors after obtaining the whole populations of all the qubit-states. For a single ion, the measured populations and the real values should have a relationship of,

$$\begin{pmatrix} P_1^{\text{mea}} \\ P_0^{\text{mea}} \end{pmatrix} = \begin{pmatrix} 1 - p_{1 \rightarrow 0} & p_{0 \rightarrow 1} \\ p_{1 \rightarrow 0} & 1 - p_{0 \rightarrow 1} \end{pmatrix} \begin{pmatrix} P_1^{\text{real}} \\ P_0^{\text{real}} \end{pmatrix} = \mathbf{M} \cdot \begin{pmatrix} P_1^{\text{real}} \\ P_0^{\text{real}} \end{pmatrix}. \quad (5-31)$$

Here  $P_i^{\text{mea}}$  and  $P_i^{\text{real}}$  is the measured and the real population of the  $|i\rangle$  state, and  $p_{i \rightarrow j}$  is the probability of detecting the  $|i\rangle$  state as  $|j\rangle$ . Assuming we have the knowledge of the detection errors of each state, the real state populations can be reconstructed by reversing Eq. (5-31),

$$\begin{pmatrix} P_1^{\text{real}} \\ P_0^{\text{real}} \end{pmatrix} = \mathbf{M}^{-1} \cdot \begin{pmatrix} P_1^{\text{mea}} \\ P_0^{\text{mea}} \end{pmatrix}. \quad (5-32)$$



For a  $N$ -qubit system, the error transfer matrix  $\mathbf{M}$  has  $2^N \times 2^N$  elements. When crosstalk errors in the detection process can be effectively neglected, the  $N$ -qubit error transfer matrix can be decomposed into,

$$\mathbf{M} = \mathbf{M}_N \otimes \dots \otimes \mathbf{M}_1, \quad (5-33)$$

where  $\mathbf{M}_i$  is the error transfer matrix of the  $i$ -th ion. By experimentally determining the matrix  $\mathbf{M}$ , the real population of each state can be reconstructed by  $\vec{P}^{\text{real}} = \mathbf{M}^{-1} \cdot \vec{P}^{\text{meas}}$ , where  $\vec{P} = \{P_{1\dots 1}, \dots, P_{0\dots 0}\}$ . In practice, to avoid non-physical results, we utilize the maximum-likelihood method to estimate the real populations by minimizing the 2-norm  $\|\vec{P}^{\text{meas}} - \mathbf{M} \cdot \vec{P}^{\text{real}}\|_2$  subject to the constraints of  $\sum_i P_i^{\text{real}} = 1$  and  $\vec{P}^{\text{real}} > 0$ .

By combining the tools of the individual laser addressing and the spatially resolved detection, we can independently apply and detect single-qubit rotations on each ion, and the Rabi oscillations obtained in the experiment are shown in Fig. 5.12. Here, all the motional modes are cooled to their ground states, so that we can observe almost full contrast for each oscillation. Due to the mismatch between the equal-spaced individual beams and the unequal-spaced ion-chain, some ions suffer from a higher intensity noise, and the corresponding oscillations are not smooth enough; for example, the oscillation in Fig. 5.12 (a). Moreover, we again prepare a maximally entangled state by applying the two-qubit entangling gate in a two-qubit chain, and the results are illustrated in Fig. 5.13. Compared with the previous results shown in Fig. 5.3 and Fig. 5.4, the state fidelity is improved to  $(98.6 \pm 1.1)\%$  after further stabilizing the pulsed laser and the individual addressing system.

### Updating: detection with multi-channel PMT

By utilizing the EMCCD as the detection device, we can resolve the state of each qubit. However, due to the low quantum efficiency at UV wavelength and slow speed of the readout process, the performance of detection by the EMCCD is worse than that of by the PMT. To achieve spatially resolved detection while keeping the detection speed and fidelity, we are updating the detection device to a multi-channel PMT<sup>[150]</sup>.

For now, we have already installed a 32-channel PMT (Hamamatsu H11460) in our system. All the PMT channels are distributed in a one-dimensional array with a spacing of 1 mm for the nearby two-channel. The active area of each channel is 0.8 mm×7 mm. Considering that the spacing of the ions is around 5  $\mu\text{m}$ , an imaging system with a

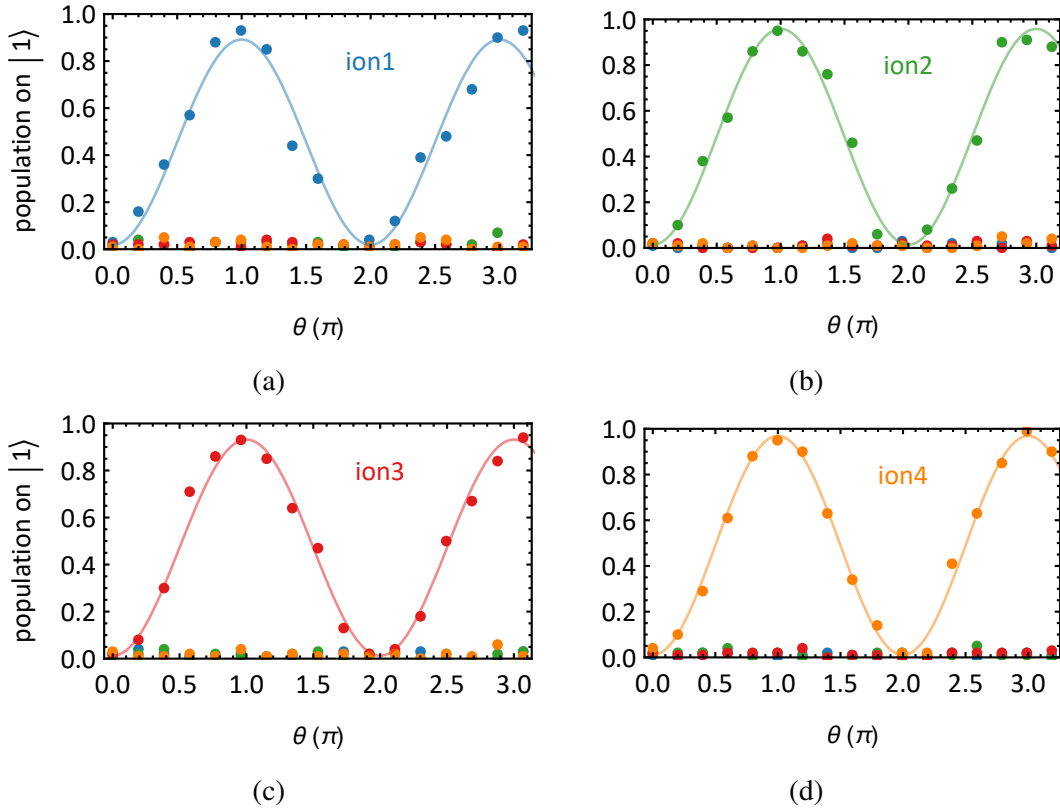


Figure 5.12 Rabi oscillation of carrier transition on each ion. Here, a chain consisting of four ion qubits are confined.

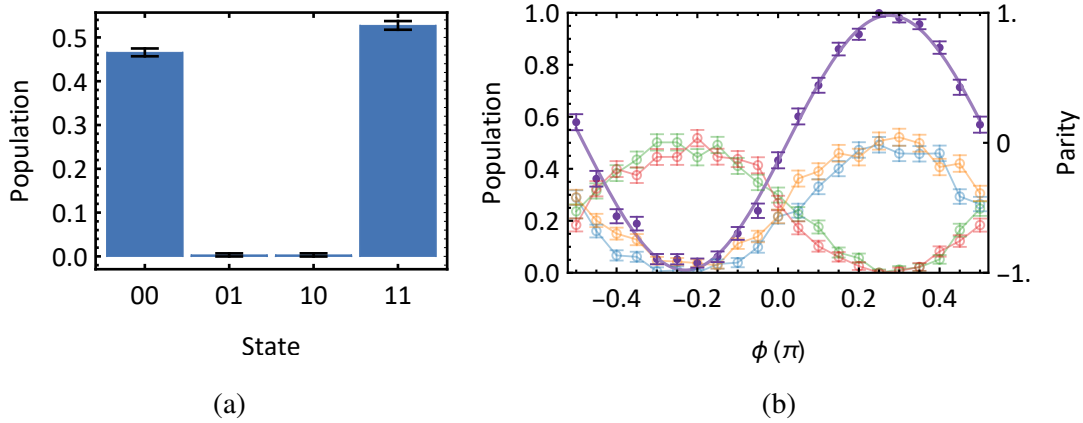


Figure 5.13 Fidelity measurement of the prepared maximally entangled state. (a) Population on each qubit-state. Now we can distinguish all the possible states. The total populations occupied in the  $|00\rangle$  and  $|11\rangle$  states is 99.3%. (b) Measurement of state correlation. The parity oscillation (shown in the purple dots) is obtain from the state oscillations (shown in the blue, green, red and orange lines for the  $|00\rangle$ ,  $|01\rangle$ ,  $|10\rangle$  and  $|11\rangle$  states, respectively). The fitting result of the parity oscillation (shown in the purple line) indicate a contrast of 98.0%. All the data is detection error corrected.

magnification of  $1 \text{ mm}/5 \mu\text{m} \sim 200$  is required. Therefore, we update the imaging system shown in Fig. 3.7 to a new version, which is illustrated in Fig. 5.14.

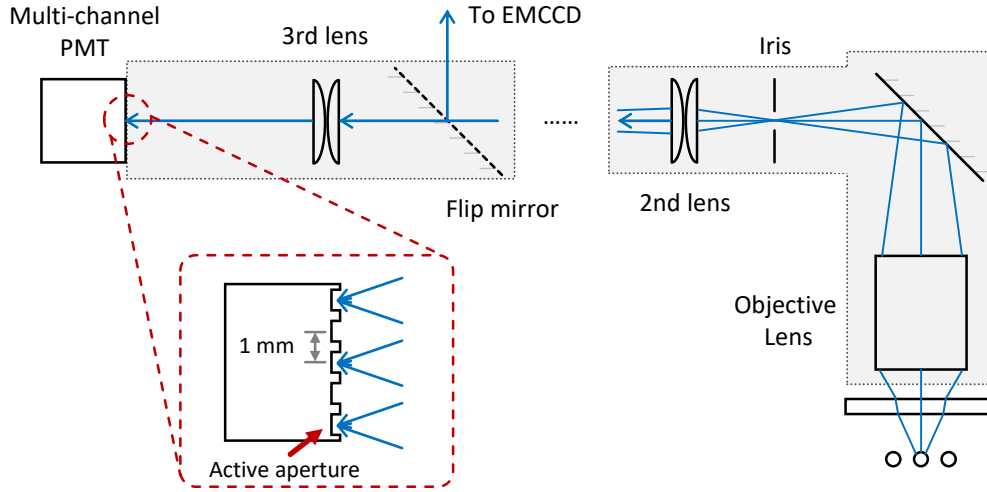


Figure 5.14 Updated imaging system. The 3rd lens is installed to provide an additional magnification around four in this path.

To minimize the detection crosstalk from nearby ions, we map all the ions to the channels with the odd (or even) number, as shown in the inset figure of Fig. 5.14, which requires the magnification provided by the third lens to be around four. The collected fluorescence from five ions by using the multi-channel PMT is shown in Fig. 5.15, in which each ion can be clearly distinguished. However, it is challenging to focus the image of each ion well and then map them to the corresponding channel. In the figure, the spread of the ion's fluorescence to the nearby channels is quite severe. The primary error source, which induces the spread, is due to the serious spherical aberration. Because the quantum efficiency of this type multi-channel PMT is only a half of the single-channel one, and the part of counts would be lost due to the dead area between the adjacent channels, the duration of detection is extended to  $250 \mu\text{s}$  to keep the same amount of the average photon number.

This detection setup is still under exploring, and the detection fidelity and the crosstalk of multiple qubits should be carefully characterized. In order to suppress the crosstalk and improve the detection fidelity, we can try to optimize the imaging of the ion-chain. Meanwhile, several schemes are proposed to improve the fidelity of classifying the projected state by the way of machine learning<sup>[87-88]</sup>. Moreover, it is believed that by coupling fluorescence from the ion-chain to a fiber-array can significantly suppress crosstalk, due to limited N.A. of fibers.

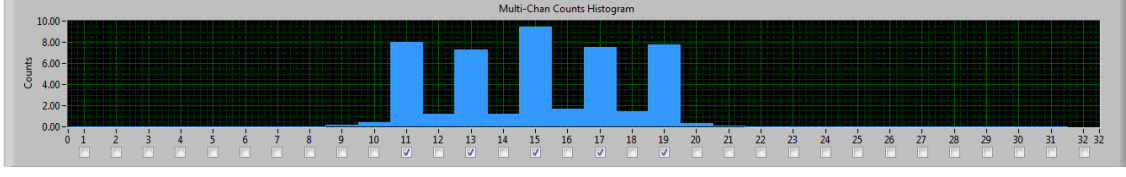


Figure 5.15 Photons collected by each PMT channel. Here, five ions are mapped on the odd channels of  $\{11, 13, 15, 17, 19\}$ . Due to the mismatch between the ion-spacings and channel spacings, and the dead area between nearby two channels, the counts of the 2nd and the 4th ions are less than the others.

## 5.4 Robust universal gate set

As we mentioned at the beginning of this chapter, to achieve universal quantum computation, the universal gate set, including single-qubit rotations and two-qubit entangling gates, is required. According to the discussion in Chap. 3 and this chapter, we have been clear of how to scalably realize the universal gate set in the trapped-ion platform. However, for fault-tolerant quantum computation, we need quantum gates with pretty low error rates. On the one hand, we should fully stabilize the whole system, suppressing all potential noises as well as possible. On the other hand, robust schemes are pursued to make gates insensitive to particular noises. In the following content, several popular schemes would be introduced.

### 5.4.1 Single-qubit rotation

For single-qubit rotations,  $R_\phi(\theta)$ , the noises in the rotation angle  $\theta$ , and the rotation axis  $\phi$  are mainly considered, which are directly related to the intensity and phase of the driving fields.

#### Intensity insensitive rotation

Here, we characterize the noise on the rotation angle as a small perturbation  $\epsilon\theta$ . The intensity noisy rotation,  $R_\phi(\tilde{\theta})$ , can be express as,

$$\begin{aligned} R_\phi(\tilde{\theta}) &= R_\phi(\theta(1 + \epsilon)) \\ &= R_\phi(\theta) \left( 1 - i \frac{\epsilon\theta}{2} \sigma_\phi \right) + O(\epsilon^2), \end{aligned} \quad (5-34)$$

where  $\theta$  is the desired value of the rotation angle, while  $\tilde{\theta} = \theta(1 + \epsilon)$  is the corresponding noisy one. The last line is obtained from the Taylor expansion of  $R_\phi(\epsilon\theta)$ . Therefore, the conventional single-qubit rotation is sensitive to the first-order of the intensity noise.

To reduce the sensitivity, a simple way is to utilize composite rotations, and one of the broadly used methods is known as SK1 (SK stands for Solovay-Kitaev)<sup>[151]</sup>. The sequence of the SK1 composite rotations can be written as,

$$R_{\phi}^{\text{SK1}}(\theta) = R_{\phi}(\tilde{\theta})R_{\phi+\phi_{\theta}}(-\tilde{2}\pi)R_{\phi-\phi_{\theta}}(-\tilde{2}\pi), \quad (5-35)$$

where  $\phi_{\theta} = \arccos(\theta/4\pi)$ . By inserting Eq. (5-34) into Eq. (5-35), the composite rotations can be approximated to be,

$$\begin{aligned} R_{\phi}^{\text{SK1}}(\theta) &= R_{\phi}(\theta) \left( 1 - i\frac{\epsilon\theta}{2}\sigma_{\phi} \right) (1 + i\epsilon\pi\sigma_{\phi+\phi_{\theta}}) (1 + i\epsilon\pi\sigma_{\phi-\phi_{\theta}}) + O(\epsilon^2) \\ &= R_{\phi}(\theta) \left( 1 - i\frac{\epsilon\theta}{2}\sigma_{\phi} \right) \left( 1 + i\frac{\epsilon\theta}{2}\sigma_{\phi} \right) + O(\epsilon^2) \\ &= R_{\phi}(\theta) + O(\epsilon^2), \end{aligned} \quad (5-36)$$

where the simplification of the first line is due to  $R_{\phi\pm\phi_{\theta}}(-2\pi) = -1$ , and the second line is due to the relation of  $\sigma_{\phi+\phi_{\theta}} + \sigma_{\phi-\phi_{\theta}} = 2\cos(\phi_{\theta})\sigma_{\phi}$ . Obviously in Eq. (5-36), the first order sensitivity to the intensity noise vanishes. Experimentally we test the SK1 composite rotations with  $\theta = \pi$  and  $\theta = \pi/2$ , corresponding to the  $\pi$ -rotation and  $\pi/2$ -rotation respectively, by varying the relative intensity error  $\epsilon$  from  $-1$  to  $1$ . The results are summarized in Fig. 5.16. The wider plateaus near  $\epsilon \sim 0$ , compared with that of by using the conventional single-qubit rotation, indicate the robustness to the intensity noise.

Moreover, in general, the  $n$ -th order SK composite gate (SK $n$ ) can get rid of all the noise sensitivity up to the  $n$ -th order, resulting in an operation described by<sup>[151]</sup>,

$$R_{\phi}^{\text{SK}n}(\theta) = R_{\phi}(\theta) + O(\epsilon^{n+1}). \quad (5-37)$$

As a trade-off, such a composite pulse would be decomposed into a pretty long sequence of noisy rotations. Other than the SK method, there are still several methods to construct the composite sequence, for example the broadband method<sup>[152]</sup> and the transformed SK method<sup>[153]</sup>.

### Phase insensitive rotation

For the single-qubit rotation achieved by the two-photon stimulated Raman transition, the rotating axis  $\phi$  is determined by the relative optical phase of the two Raman beams. However, if we apply non-copropagating Raman beams, the jittering of the relative optical length,  $\delta r$ , would introduce a phase noise,  $\delta\phi = k\delta r$ , resulting in a phase-noisy rotation

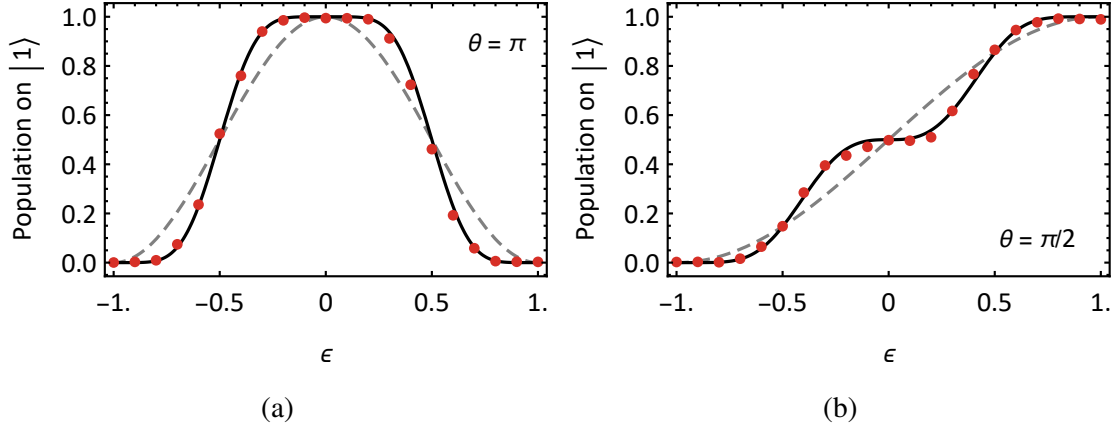


Figure 5.16 Application of the SK1 composite rotations to achieve intensity insensitive single-qubit rotation. The population on the  $|1\rangle$  state with varying relative error  $\epsilon$  is measured experimentally. (a) and (b) refer to the  $\pi$ -rotation and  $\pi/2$ -rotation, respectively. The black lines are the theoretical prediction by applying the SK1 composite rotations, while the gray lines indicates the theoretical results by using the noisy rotation in Eq. (5-34). The red dots are experimental results, which match the theoretical calculation well.

$R_{\tilde{\phi}}(\theta)$ , where  $\tilde{\phi} = \phi + \delta\phi$ . Note that, the value of the effective wave vector  $k$  is  $\sqrt{2} \times 2\pi/375 \text{ nm} \approx 24 \mu\text{m}^{-1}$  according to the Raman geometry shown in Fig. 5.5, which means that  $0.13 \mu\text{m}$  shift in the relative optical length would cause a  $\pi$  phase shift. Such jittering mainly comes from mechanical fluctuations and vibrates at low frequencies. Therefore, the value of  $\phi$  might be stable in the duration of a single rotation, but be fluctuating between different rotations, resulting in an unpredictable rotation axis.

In practice, we passively stabilize the Raman system by tightly fixing every optical element and cover the laser path to reduce the influence of the airflow. We also consider an active lock of the length difference through an interferometer consisted of the two Raman arms in the future. However, it is still challenging to control the stability of the laser path in long term. Instead, another straightforward way is to apply co-propagating Raman beams, getting rid of the phase noise by vanishing the effective wave vector  $k$ , resulting in a phase-insensitive single-qubit rotation,  $R_{\phi}^{\text{co}}(\theta)$ . The ensuing problem is how to realize a two-qubit entangling gate in the phase-insensitive way.

#### 5.4.2 Two-qubit entangling gate

Implementing a phase-insensitive two-qubit gate is tricky because we have to apply non-copropagating Raman beams for the ion-motion coupling. Therefore, the phase noise from the jittering optical path is inevitable. To cancel such phase noise, a composite-like

gate<sup>[55,89]</sup>,

$$\begin{aligned} ZZ(\theta) &= R_{\pi/2+\delta\phi}\left(\frac{\pi}{2}\right) \cdot e^{-i\theta\sigma_{\delta\phi}\sigma_{\delta\phi}} \cdot R_{\pi/2+\delta\phi}\left(-\frac{\pi}{2}\right) \\ &= e^{-i\theta\sigma_z\sigma_z}, \end{aligned} \quad (5-38)$$

might work, where a phase-noisy XX-gate is sandwiched by two phase-noisy single-qubit rotations along the y-axis, yielding a phase-free ZZ-gate. We can employ phase-insensitive single-qubit rotations,  $R_{\phi}^{\text{co}}(\theta)$ , and above phase-free ZZ-gate as our practical universal gate set. Note that, both phase insensitive and sensitive single-qubit rotations are required here.

Another scheme is proposed by applying the blue sideband and red sideband induced by different geometric configurations of the Raman laser beams<sup>[89]</sup>, as shown in Fig. 5.17. The effective Hamiltonian of the sideband transitions from these two configurations can be written as,

$$H_{\text{bsb}} = \frac{i\eta\Omega}{2} \left( \sigma_+ a^\dagger e^{i(\nu-\mu)t} e^{i\phi_b} - \text{h.c.} \right), \quad (5-39)$$

$$H_{\text{rsb}} = \frac{-i\eta\Omega}{2} \left( \sigma_+ a e^{-i(\nu-\mu)t} e^{i\phi_r} - \text{h.c.} \right), \quad (5-40)$$

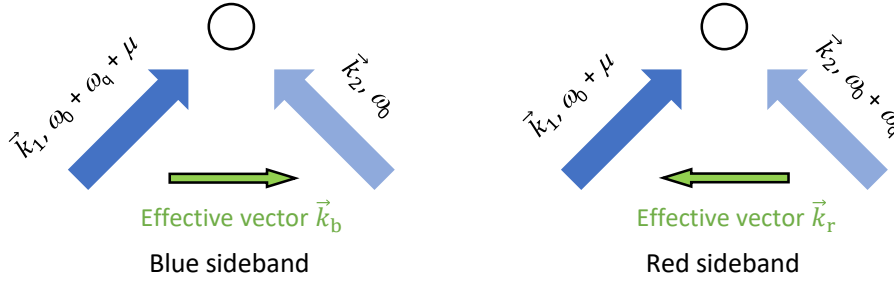


Figure 5.17 Different geometric configurations to apply sideband transitions. In the left configuration, the frequency of the Raman beam in the darker blue arrow is higher than that of in the lighter blue arrow, yielding an effective wave vector pointing to the right. On the contrary, in the right configuration, the frequency of the Raman beam in the darker blue arrow is lower, resulting in an effective wave vector pointing to the left.

The additional minus sign in the red sideband transition is due the opposite directions of the two effective wave vectors. The state-dependent force obtained from those two sidebands can be expressed as,

$$H_{\text{SDF}} = \frac{i\eta\Omega}{2} (\sigma_+ e^{i\phi_s} + \text{h.c.}) \left( a^\dagger e^{i(\nu-\mu)t} e^{-i\phi_p} - \text{h.c.} \right), \quad (5-41)$$





## Chapter 6 Extension: Global entangling gates on arbitrary ion qubits

In the framework of the quantum circuit model, any universal quantum computation task, such as the quantum phase estimation<sup>[20]</sup>, the Shor's algorithm<sup>[4]</sup> or the quantum variational eigensolver<sup>[21]</sup>, can be decomposed into a sequence consisting of the single-qubit rotations and the two-qubit entangling gates. However, such decomposition is not necessarily efficient. It has been pointed out that polynomial or even exponential speedups can be obtained with global  $N$ -qubit ( $N$  greater than two) entangling gates<sup>[154-156]</sup>. Such global gates involve all-to-all connectivity, which emerges naturally among trapped-ion qubits with laser-driven collective motional modes<sup>[16,135,157-160]</sup>, and have been implemented by using a single motional mode<sup>[12,56]</sup>. However, the single-mode approach is hard to scale up because isolation of single mode is challenging as the number of ions increases in a single crystal. The multi-mode schemes, as we briefly introduced in Sec. 5.1, are scalable<sup>[136-137,161]</sup>, but no one has explored the possibility of experimentally applying them to the global  $N$ -qubit case yet.

In this chapter, we would introduce a scalable scheme to realize the global entangling gates on multiple  $^{171}\text{Yb}^+$  ion qubits by coupling to multiple motional modes through modulated laser fields. Such global gates require decoupling multiple motional modes and balancing all pairwise coupling strengths during the gate, demanding fully independent control capability on each ion<sup>[16]</sup>. To demonstrate the usefulness and flexibility of these global gates, we experimentally generate a Greenberger-Horne-Zeilinger (GHZ) state with up to four qubits using a single global operation. Our approach realizes global entangling gates as scalable building blocks for universal quantum computing, motivating future research in scalable global methods for quantum information processing.

### 6.1 Entangling multiple ion qubits through multiple motional modes

One of the representative more than 2-qubit entangling gates is a global entangling gate, which can generate entanglement among all involved qubits in a symmetric way. The global entangling gate acting on  $N$  qubits is defined as,

$$\text{GE}_N(\Theta) = \exp \left[ -i \Theta \sum_{j < j'}^N \sigma_x^j \sigma_x^{j'} \right], \quad (6-1)$$

where all of the two-body couplings are driven simultaneously. Apparently, a global entangling gate applied to  $N$  qubits is equivalent to  $N(N - 1)/2$  pairwise entangling gates<sup>[156]</sup>, which provides the possibility of simplifying the quantum circuits. For example, the  $N - 1$  pairwise entangling operations in the preparation of the  $N$ -qubit GHZ state<sup>[13,138]</sup> can be replaced by a single global entangling gate  $GE_N(\pi/4)$ , as shown in Fig. 6.1. In fact, several theoretical works have already indicated that innumerable quantum algorithms and universal quantum simulation of various many-body systems would benefit from the global entangling gates in the efficient construction of quantum circuits. In particular, a set of  $O(N)$  CNOT gates in the quantum phase estimation algorithm<sup>[156]</sup> and each  $O(N)$ -body interaction term emerged in the simulation of fermionic systems due to the Jordan-Wigner transformation<sup>[21,162]</sup>, which requires  $O(N)$  two-qubit entangling gates, can be both efficiently implemented by  $O(1)$  global gates.

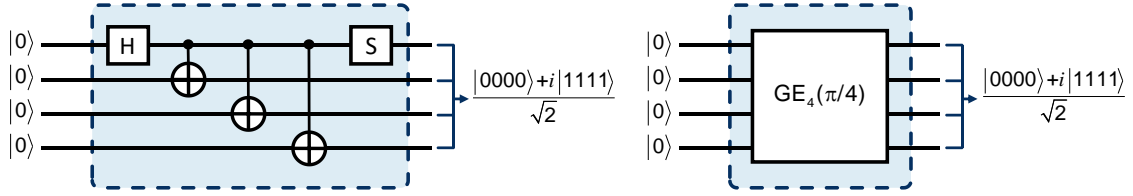


Figure 6.1 Efficient construction of a quantum circuit using a global gate. For the generation of the four-qubit GHZ state, we need one Hadamard gate (H gate in the figure) and three pairwise entangling gates, which can be replaced by a single global four-qubit entangling gate. The phase gate (S gate) at the end of the first circuit is used to compensate for the phase difference between two circuit outputs.

Considering the experimental realization, as we discussed in the last chapter, the ion qubits are entangling through the collective motional modes. Therefore, the ion qubits confined in a single ion crystal have the long-range interaction naturally, which is similar to the form of Eq. (6-1). By simultaneously applying the state-dependent forces<sup>[163]</sup> to the multiple ions, as shown in Fig. 6.2, the Hamiltonian in Eq. (5-6) can be extended to be<sup>[137]</sup>,

$$H_{\text{SDF}} = \sum_{j=1}^N \sum_{m=1}^M \frac{\eta_{j,m} \Omega_j(t)}{2} \left( a_m^\dagger e^{i\delta_m t} e^{-i\phi_j(t)} + a_m e^{-i\delta_m t} e^{i\phi_j(t)} \right) \sigma_x^j. \quad (6-2)$$

Here we consider a general situation with  $N$  qubits and  $M$  collective motional modes, and have already assumed to modulate the forces on each ion independently. The evolution

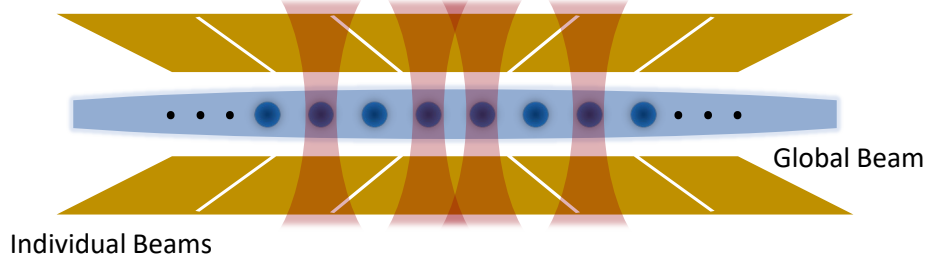


Figure 6.2 Experimental setup used for the implementation of the global entangling gate. Each ion in the trap is individually manipulated by Raman beams: a global beam (blue) and an individual beam addressing a single ion (red). The individually addressed qubits are involved in the global entangling gate.

operator governed by the above Hamiltonian turns out to be

$$U(\tau) = \exp \left[ \sum_{j,m} \left( \alpha_{j,m}(\tau) a_m^\dagger - \alpha_{j,m}^*(\tau) a_m \right) \sigma_x^j - i \sum_{j < j'} \theta_{j,j'}(\tau) \sigma_x^j \sigma_x^{j'} \right]. \quad (6-3)$$

Here  $\theta_{j,j'}(\tau)$  represents the coupling strength between the  $j$ -th and the  $j'$ -th qubit, which has the form of,

$$\theta_{j,j'}(\tau) = - \sum_m \int_0^\tau dt_2 \int_0^{t_2} dt_1 \frac{\eta_{j,m} \eta_{j',m} \Omega_j(t_2) \Omega_{j'}(t_1)}{2} \sin [\delta_m(t_2 - t_1) - (\phi_j(t_2) - \phi_{j'}(t_1))], \quad (6-4)$$

while the residual displacement of the  $j$ -th ion and  $m$ -th mode is given by

$$\alpha_{j,m}(\tau) = -i\eta_{j,m} \int_0^\tau \frac{\Omega_j(t) e^{-i\phi_j(t)}}{2} e^{i\delta_m t} dt = 0. \quad (6-5)$$

Compared with the evolution operator in Eq. (5-14), all the pairwise coupling are included.

To perform the global gate  $GE_N(\Theta)$  in Eq. (6-1) from the time evolution of Eq. (6-3), we have to close all the motional trajectories and balance all the coupling strengths, which lead to the following constraints,

$$\alpha_{j,m}(\tau) = 0, \quad (6-6)$$

$$\theta_{j,j'}(\tau) = \Theta. \quad (6-7)$$

Given the size of the whole system, there are  $N \times M$  constraints from Eq. (6-6) and  $\binom{N}{2}$  from Eq. (6-7). Therefore, we have to satisfy a total number of  $N(N-1)/2 + NM$  constraints. In principle, we can fulfill the constraints by independently modulating the amplitude

$\Omega_j(t)$  or the phase  $\phi_j(t)$  of the Rabi frequency on each ion in a continuous or discrete way. In the experimental implementation, we choose discrete phase modulation because we have high-precision controllability on the phase degree of freedom. We divide the total gate operation into  $K$  segments with equal duration and independently modulate the phase on each ion in each segment, which provides  $N \times K$  independent variables. Because of the nonlinearity of the constraints, it is challenging to find analytical solutions of the constraints Eq. (6-6) and Eq. (6-7). Therefore, we construct an optimization problem to find numerical solutions. We minimize the objective function of  $\sum_{j,m} |\alpha_{j,m}(\tau)|^2$ <sup>[139,142-143]</sup> subject to the constraints of Eq. (6-7). The details of the constraints under discrete phase modulation and the optimisation problem construction are provided in the following section.

## 6.2 Pulse optimization with phase modulation

### 6.2.1 Expressions of constraints under discrete phase modulation

In this section, we first give the detailed expressions of the constraints under the discrete phase modulation. For the convenience of theoretical calculation, we fix the total gate time to be  $\tau$  and divide it into  $K$  equal segments with the segment duration of  $\tau_s = \tau/K$ . The phases are modulated discretely with the form of

$$\phi_j(t) = \begin{cases} \phi_{j,1} & 0 \leq t \leq \tau_s \\ \dots & \\ \phi_{j,k} & (k-1)\tau_s \leq t \leq k\tau_s, \\ \dots & \\ \phi_{j,K} & \tau - \tau_s \leq t \leq \tau \end{cases} \quad (6-8)$$

where  $\phi_{j,k}$  is the phase of the Rabi frequency on the  $j$ -th qubit in the  $k$ -th segment. Moreover, the amplitude of Rabi frequency on each qubit is also modulated in time, with the form of,

$$\Omega_j(t) = \Omega_j^{\max} w(t), \quad (6-9)$$

where  $\Omega_j^{\max}$  is the maximal value of the amplitude applied on the  $j$ -th qubit, and  $w(t)$  is the pulse-shaping function to slowly turn on (off) amplitude at the first (last) segment. For

simplicity, here we choose  $w(t)$  to be the following form,

$$w(t) = \begin{cases} \sin^2\left(\frac{\pi}{2\tau_s}t\right) & 0 \leq t \leq \tau_s \\ 1 & \tau_s \leq t \leq \tau - \tau_s \\ \sin^2\left(\frac{\pi}{2\tau_s}(t - \tau)\right) & \tau - \tau_s \leq t \leq \tau \end{cases} \quad (6-10)$$

The  $\sin^2$ -profile pulse shaping here is to flatten the fast oscillation due to the off-resonant coupling to the carrier transition, minimizing the sensitivity to the gate duration<sup>[164]</sup>.

We further calculate the detailed expression of the constraints. Starting from the constraint of Eq. (6-5) and then inserting the pulse scheme of Eq. (6-8) and Eq. (6-10), we can rewrite the residual displacements to be,

$$\begin{aligned} \alpha_{j,m}(\tau) &= -i\eta_{j,m} \int_0^\tau \frac{\Omega_j(t)e^{-i\phi_j(t)}}{2} e^{i\delta_m t} dt \\ &= \frac{\eta_{j,m}\Omega_j^{\max}}{2} \sum_{k=1}^K (-ie^{-i\phi_{j,k}}) \int_{(k-1)\tau_s}^{k\tau_s} w(t)e^{i\delta_m t} dt. \end{aligned} \quad (6-11)$$

Here we define several notations as follows,

$$\text{Ts}_{m,k} = \int_{(k-1)\tau_s}^{k\tau_s} w(t) \sin[\delta_m t] dt, \quad (6-12)$$

$$\text{Tc}_{m,k} = - \int_{(k-1)\tau_s}^{k\tau_s} w(t) \cos[\delta_m t] dt, \quad (6-13)$$

$$\text{X}_{j,k} = \cos \phi_{j,k}, \quad (6-14)$$

$$\text{Y}_{j,k} = \sin \phi_{j,k}, \quad (6-15)$$

and then the residual displacement  $\alpha_{j,m}(\tau)$  can be simplified to be

$$\alpha_{j,m}(\tau) = \eta_{j,m}\Omega_j^{\max} d_{j,m}/2 \quad (6-16)$$

$$d_{j,m} = \sum_{k=1}^K (\text{Ts}_{m,k}\text{X}_{j,k} + \text{Tc}_{m,k}\text{Y}_{j,k}) + i \sum_{k=1}^K (\text{Tc}_{m,k}\text{X}_{j,k} - \text{Ts}_{m,k}\text{Y}_{j,k}). \quad (6-17)$$

Here  $d_{j,m}$  is the scaled residual displacement of  $\alpha_{j,m}(\tau)$  to remove the redundant factor, Similarly, for the coupling strength of Eq. (6-4) we can also rewrite it to be

$$\begin{aligned} \theta_{j,j'}(\tau) &= \Omega_j^{\max}\Omega_{j'}^{\max} g_{j,j'}, \quad (6-18) \\ g_{j,j'} &= \sum_{k,l} \text{X}_{j,k}\text{Gs}_{j,j',k,l}\text{X}_{j',l} + \text{Y}_{j,k}\text{Gs}_{j,j',k,l}\text{Y}_{j',l} \end{aligned}$$

$$+ \mathbf{X}_{j,k} \mathbf{Gc}_{j,j',k,l} \mathbf{Y}_{j',l} - \mathbf{Y}_{j,k} \mathbf{Gc}_{j,j',k,l} \mathbf{X}_{j',l}, \quad (6-19)$$

where  $g_{j,j'}$  is the rescaled coupling strength of  $\theta_{j,j'}(\tau)$  and

$$\mathbf{Gs}_{j,j',k,l} = \begin{cases} -\sum_m \frac{\eta_{j,m} \eta_{j',m}}{2} \int_{(k-1)\tau_s}^{k\tau_s} \int_{(l-1)\tau_s}^{l\tau_s} dt_2 dt_1 w(t_2) w(t_1) \sin[\delta_m(t_2 - t_1)] & l < k \\ -\sum_m \frac{\eta_{j,m} \eta_{j',m}}{2} \int_{(k-1)\tau_s}^{k\tau_s} \int_{(k-1)\tau_s}^{t_2} dt_2 dt_1 w(t_2) w(t_1) \sin[\delta_m(t_2 - t_1)] & l = k \\ 0 & l > k \end{cases}, \quad (6-20)$$

$$\mathbf{Gc}_{j,j',k,l} = \begin{cases} -\sum_m \frac{\eta_{j,m} \eta_{j',m}}{2} \int_{(k-1)\tau_s}^{k\tau_s} \int_{(l-1)\tau_s}^{l\tau_s} dt_2 dt_1 w(t_2) w(t_1) \cos[\delta_m(t_2 - t_1)] & l < k \\ -\sum_m \frac{\eta_{j,m} \eta_{j',m}}{2} \int_{(k-1)\tau_s}^{k\tau_s} \int_{(k-1)\tau_s}^{t_2} dt_2 dt_1 w(t_2) w(t_1) \cos[\delta_m(t_2 - t_1)] & l = k \\ 0 & l > k \end{cases}. \quad (6-21)$$

Note that, both  $\mathbf{Gs}_{j,j',k,l}$  and  $\mathbf{T}_{s_{j,j',k,l}}$  are non-zero only when  $l \leq k$ , because the double integral is performed when  $t_1 \leq t_2$ <sup>[165]</sup>. The advantage of choosing expression of Eq. (6-17) and Eq. (6-19) is that it is convenient to rearrange them into the matrix-form as follows,

$$d_{j,m} = (\mathbf{T}_{s_m}^T \mathbf{X}_j + \mathbf{T}_{c_m}^T \mathbf{Y}_j) + i (\mathbf{T}_{c_m}^T \mathbf{X}_j - \mathbf{T}_{s_m}^T \mathbf{Y}_j), \quad (6-22)$$

$$g_{j,j'} = \mathbf{X}_j^T \mathbf{Gs}_{j,j'} \mathbf{X}_{j'} + \mathbf{Y}_j^T \mathbf{Gs}_{j,j'} \mathbf{Y}_{j'} + \mathbf{X}_j^T \mathbf{Gc}_{j,j'} \mathbf{Y}_{j'} - \mathbf{Y}_j^T \mathbf{Gc}_{j,j'} \mathbf{X}_{j'}. \quad (6-23)$$

Here  $\mathbf{T}_{s_m}$ ,  $\mathbf{T}_{c_m}$ ,  $\mathbf{X}_j$  and  $\mathbf{Y}_j$  are the column vectors of  $\{\mathbf{T}_{s_{m,k}}\}$ ,  $\{\mathbf{T}_{c_{m,k}}\}$ ,  $\{\mathbf{X}_{j,k}\}$  and  $\{\mathbf{Y}_{j,k}\}$  respectively, while  $\mathbf{Gs}_{j,j'}$  and  $\mathbf{Gc}_{j,j'}$  are the matrix-form of  $\{\{\mathbf{Gs}_{j,j',k,l}\}\}$  and  $\{\{\mathbf{Gc}_{j,j',k,l}\}\}$  respectively. Note that, all the elements in the vectors  $\mathbf{T}_{s_m}$  and  $\mathbf{T}_{c_m}$  and the matrices  $\mathbf{Gs}_{j,j'}$  and  $\mathbf{Gc}_{j,j'}$  are fully determined by the system parameters ( $\{\nu_m\}$ ,  $\{\{\eta_{j,m}\}\}$ ) and the laser detuning respect to the carrier transition ( $\mu$ ).

According to the above calculations, we rewrite the constraints in Eq. (6-6) and Eq.

(6-7), and then summarize them as below,

$$d_{j,m} = 0, \quad (6-24)$$

$$\Omega_j^{\max} \Omega_{j'}^{\max} g_{j,j'} = \Theta, \quad (6-25)$$

$$\mathbf{X}_j^T \mathbf{X}_j + \mathbf{Y}_j^T \mathbf{Y}_j = \mathbf{1}, \quad (6-26)$$

for all the  $j, j', m$ . The constraints of Eq. (6-24) and Eq. (6-25) originate from Eq. (6-6) and Eq. (6-7), respectively, while the last one is the requirement for the normalization of trigonometric functions.

### 6.2.2 Pulse Scheme Optimization

Although we have already written all the constraints in their detailed matrix-form, it is challenging to solve the equations of constraints directly, due to the nonlinearity of Eq. (6-25) and Eq. (6-26). Instead, we construct an optimization problem by minimizing the following objective function,

$$f_{\text{obj}} = \sum_{j,m} |d_{j,m}|^2, \quad (6-27)$$

which is equivalent to  $\sum_{j,m} |\alpha_{j,m}(\tau)|^2$ , subject to the constraints of Eq. (6-25) and Eq. (6-26). The construction is still non-trivial because we want to efficiently obtain the suitable pulse scheme. The main difficulty in performing optimization is to fulfill the non-linear constraints and moreover, the number of the non-linear constraints grows quadratically with the number of qubits. To simplify the optimization problem, we utilize the symmetries of the scaled Lamb-Dicke parameters, which always have the relations of  $\eta_{j,m} = \pm \eta_{N-j+1,m}$ , and then set the  $\phi_j(t)$  and  $\Omega_j^{\max}$  to be same for the ion qubits  $j$  and  $(N - j + 1)$ . Taking  $N = 4$  case as an example, the constraints of the coupling strengths are reduced from

$$\theta_{1,2}(\tau) = \theta_{1,3}(\tau) = \theta_{1,4}(\tau) = \theta_{2,3}(\tau) = \theta_{2,4}(\tau) = \theta_{3,4}(\tau) = \Theta, \quad (6-28)$$

to

$$\theta_{1,2}(\tau) = \theta_{1,3}(\tau) = \theta_{1,4}(\tau) = \theta_{2,3}(\tau) = \Theta \quad (6-29)$$

because  $\theta_{1,2}(\tau) = \theta_{3,4}(\tau)$  and  $\theta_{1,3}(\tau) = \theta_{2,4}(\tau)$  always establish. Moreover, in practice we enforce an additional symmetry to the modulated patterns by presetting the modulated phases to be  $\phi_j(t) = -\phi_j(\tau - t)$  or  $\phi_{j,k} = -\phi_{j,K-k+1}$  before the optimizing procedure.

For this small scale case, we rewrite Eq. (6-29) with their scaled coupling strengths. By utilizing the relations of  $\Omega_1^{\max} = \Omega_4^{\max}$  and  $\Omega_2^{\max} = \Omega_3^{\max}$ , we can further simplify the non-linear constraints to be,

$$g_{1,2} = g_{1,3} \quad \text{and} \quad g_{1,2} * g_{1,3} = g_{1,4} * g_{2,3},$$

resulting in the optimization problem of minimizing  $f_{\text{obj}}$  subject to the constraints of Eq. (6.2.2) and Eq. (6-26). Therefore, we do not need to treat the amplitudes of the Rabi frequencies,  $\{\Omega_j^{\max}\}$ , as the optimization parameters, which can be solved after obtaining the modulated phase patterns.

Moreover, we note that once we find the solution of the global  $N$ -qubit entangling gate, this solution is still valid for any subset of this  $N$ -qubit system after setting  $\Omega_j^{\max}$  to be zero for any qubit  $j$  does not belong to the subset. This feature indicates that, the entangling gate can be applied on any subset of qubits by simply turn off the driving lasers on the qubits outside the subset during the operation.

### 6.3 Experimental results

We experimentally implement the global entangling gates in a single linear chain of  $^{171}\text{Yb}^+$  ions, based on the individual addressing system described in the last chapter. To test the performance of the global  $N$ -qubit entangling gate, we use the  $\text{GE}_N(\pi/4)$  gate to generate the  $N$ -qubit GHZ state and then measure the state fidelity. Starting from the product state  $|0 \cdots 0\rangle$ , the GHZ state can be prepared by applying the global entangling gate, while additional single-qubit rotations of  $R_x^j(\pm\pi/2)$  on all the qubits are required if  $N$  is odd,

$$\text{GE}_N\left(\frac{\pi}{4}\right)|0 \cdots 0\rangle = \frac{|0 \cdots 0\rangle + (-)^{N/2}i|1 \cdots 1\rangle}{\sqrt{2}} \quad N \text{ is even,} \quad (6-30)$$

$$\prod_j R_x^j\left(\pm\frac{\pi}{2}\right) \text{GE}_N\left(\frac{\pi}{4}\right)|0 \cdots 0\rangle = \frac{|0 \cdots 0\rangle + (-)^{(N\pm 1)/2}i|1 \cdots 1\rangle}{\sqrt{2}} \quad N \text{ is odd.} \quad (6-31)$$

Similar to the two-qubit bell state, the fidelity of the GHZ state can characterized as

$$\mathcal{F}_{N\text{-GHZ}} = \frac{\rho_{|0\rangle^{\otimes N}, |0\rangle^{\otimes N}} + \rho_{|1\rangle^{\otimes N}, |1\rangle^{\otimes N}} + |\rho_{|0\rangle^{\otimes N}, |1\rangle^{\otimes N}}| + |\rho_{|1\rangle^{\otimes N}, |0\rangle^{\otimes N}}|}{2}. \quad (6-32)$$

Therefore, after the state preparation, we obtain the state fidelity by measuring the population of the entangled state and the contrast of the parity oscillation as well<sup>[166]</sup>. We also use the fidelity of the GHZ state to test the important feature of the global entangling gate,



which is that we can realize entangling gates on any subset of qubits that are addressed by individual laser beams without changing any modulation pattern.

### 6.3.1 Global entangling gates on a three-ion chain

As the first demonstration, we use three  $^{171}\text{Yb}^+$  ions with the frequencies of the collective motional modes in the x-direction  $\{\nu_1, \nu_2, \nu_3\} = 2\pi \times \{2.184, 2.127, 2.044\}$  MHz. We choose the detuning  $\mu$  to be  $2\pi \times 2.094$  MHz, between the last two modes. The total gate time is fixed to be  $80 \mu\text{s}$  and divided into six segments. The details of the phase modulation pattern and the amplitude shaping with relative ratio are shown in Fig. 6.3. The specific values of the modulated phases are given in Tab. 6.1. With these parameters, the constraints of Eq. (6-6) and Eq. (6-7) are fulfilled, shown in Fig. 6.4 (a) and (b), respectively.

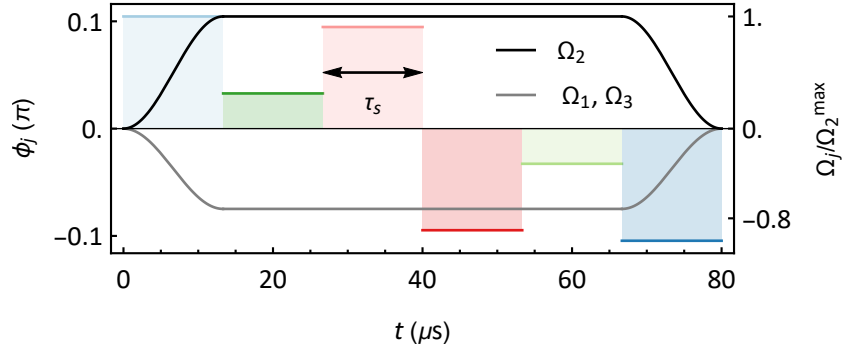
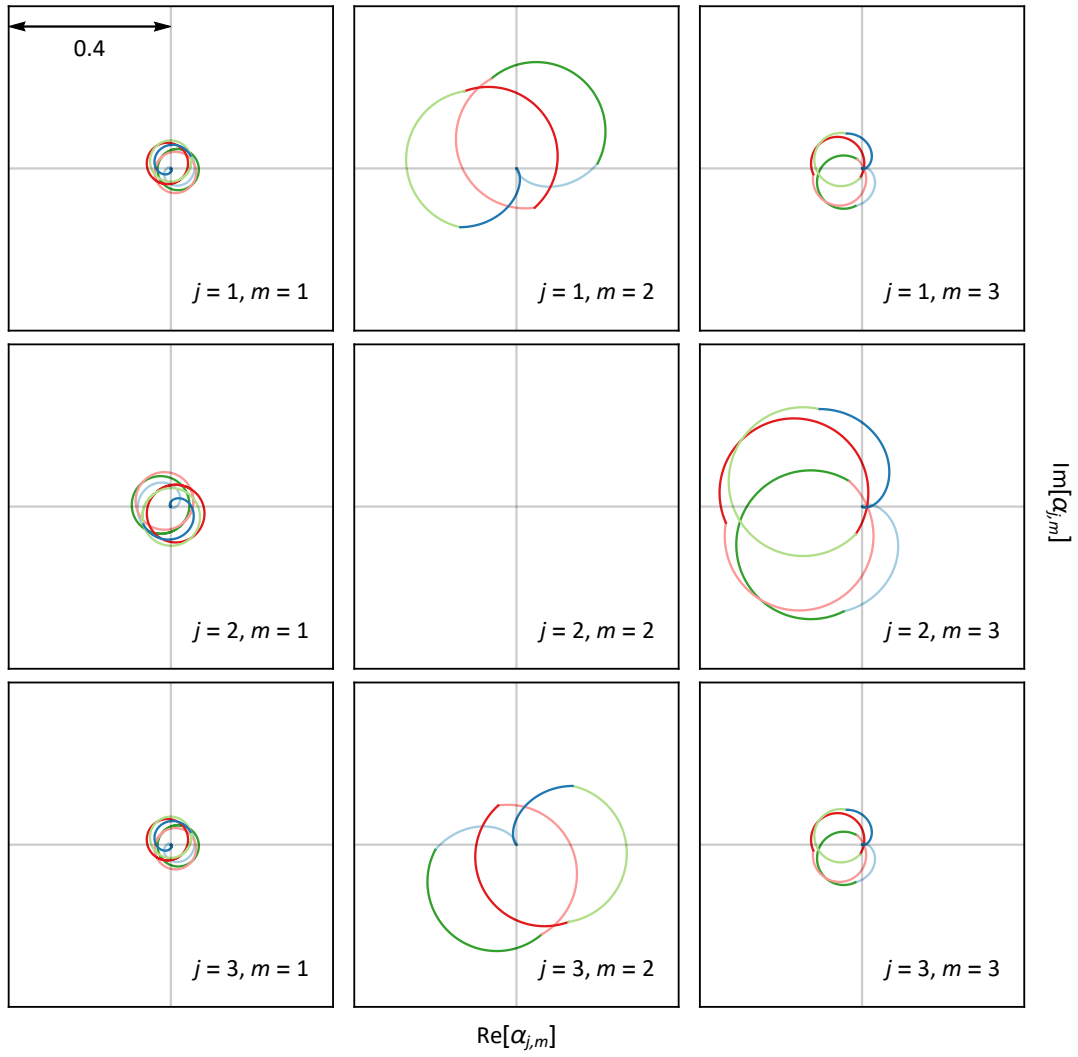


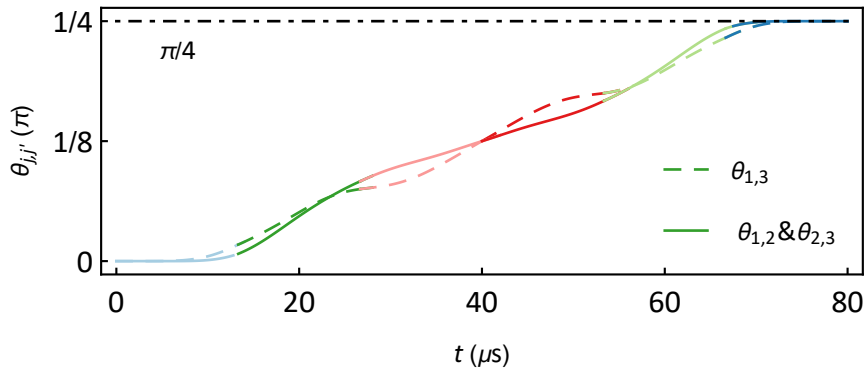
Figure 6.3 Pulse scheme with phase and amplitude modulation. The phase  $\phi_j$  is discretely modulated, as shown by the coloured lines. The amplitudes of the Rabi frequencies  $\Omega_j$ , shown by the black and grey curves, are shaped at the beginning (end) of the gate operation using a sin-squared profile with switching time equal to the duration of a single segment,  $\tau_s$ . We note that the additional  $\pi$ -phase shift of the middle ion is treated as a negative sign for  $\Omega$ .

Table 6.1 Pulse scheme for the global 3-qubit entangling gate

qubit $j$		1	2	3
$\Omega_j^{\max}$ (MHz)		$-2\pi \times 0.181$	$2\pi \times 0.253$	$-2\pi \times 0.181$
$\phi_{j,k}(\pi)$	1	0.104	0.104	0.104
	2	0.033	0.033	0.033
	3	0.095	0.095	0.095
	4	-0.095	-0.095	-0.095
	5	-0.033	-0.033	-0.033
	6	-0.104	-0.104	-0.104



(a)



(b)

Figure 6.4 Visualization of satisfaction of constraints Eq. (6-6) and Eq. (6-7). (a) Motional trajectories  $\alpha_{j,m}$ . Different colours correspond to the different segments in Fig. 6.3. (b) Accumulation of coupling strength  $\theta_{j,j'}$  over the evolution time. All of the coupling strengths increase to the desired value of  $\pi/4$ .

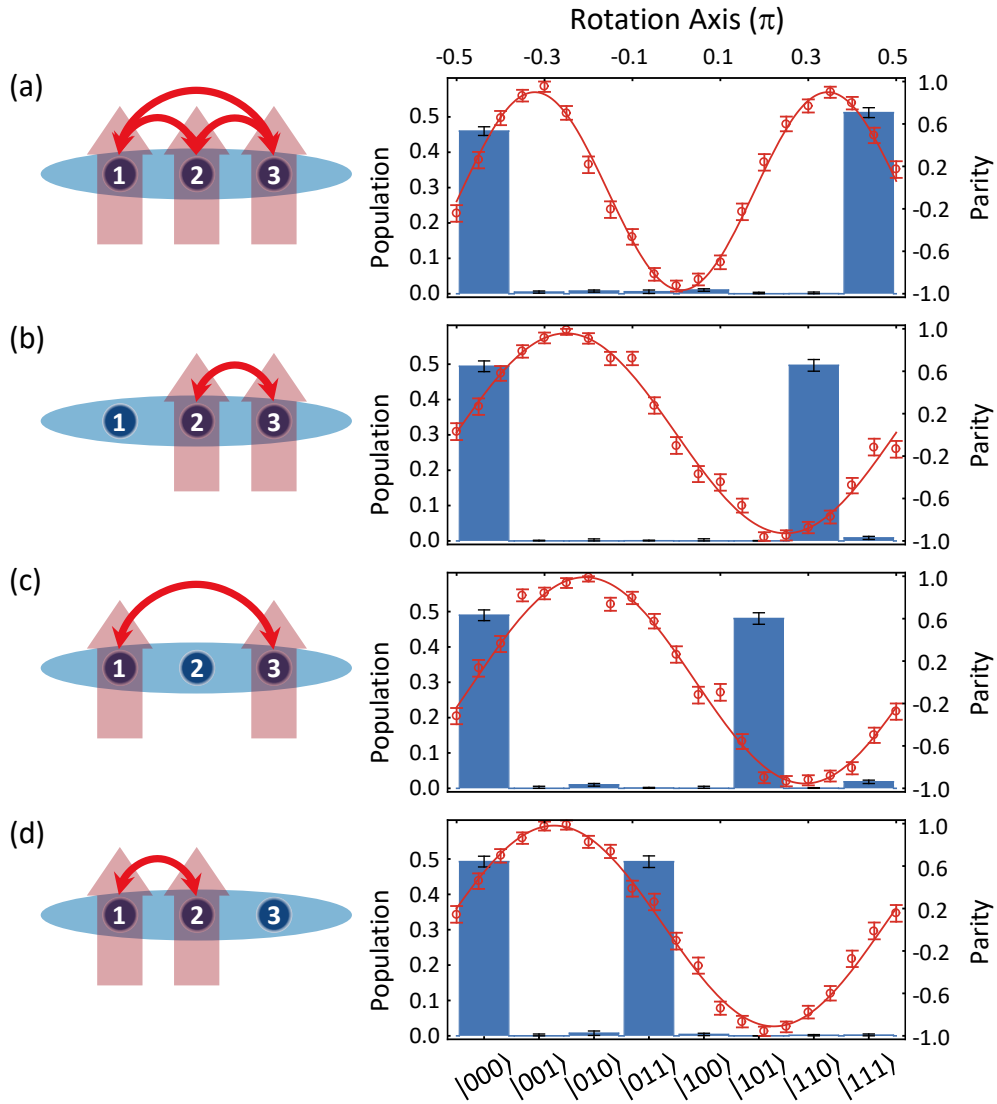


Figure 6.5 Experimental results of the global entangling gates in three ion qubits. Left column shows the capability of the global entangling gate, which can generate entanglement of (a) the entire qubits or (b)-(d) any pairs by switching on the individual beams on the target ions without changing any modulated patterns. Right column shows the population (blue histogram) and the parity oscillation (red circles for the experimental data and red curves for the fitting results) of the generated GHZ state.

We use this global 3-qubit entangling gate to prepare the 3-qubit GHZ state with the state fidelity of  $(95.2 \pm 1.5)\%$ , as shown in Fig. 6.5 (a). Moreover, by turning off the individual beam on a qubit, we can remove the couplings between the qubit and the others, as shown in Fig. 6.5. In the 3-qubit system, the global entangling gates on the subsets become the pairwise gates on the arbitrary qubit-pair, which are used to generate the 2-qubit GHZ states with the fidelities of  $(96.7 \pm 1.8)\%$ ,  $(97.1 \pm 1.9)\%$  and  $(96.5 \pm 1.5)\%$  for the qubit pairs  $\{2, 3\}$ ,  $\{1, 3\}$  and  $\{1, 2\}$ , respectively, as shown in Fig. 6.5 (b-d).

### 6.3.2 Global entangling gates on a four-ion chain

For the further demonstration, we move to a 4-qubit system with the motional frequencies  $\{\nu_1, \nu_2, \nu_3, \nu_4\} = 2\pi \times \{2.186, 2.147, 2.091, 2.020\}$  MHz. The larger system means more constraints and segments are required. To realize the global 4-qubit entangling gate, we choose the detuning  $\mu$  to be  $2\pi \times 2.104$  MHz and fix the total gate time to be  $120 \mu\text{s}$ , which is divided into twelve segments. The pulse scheme is shown in Fig. 6.6, and the specific values are shown in Tab. 6.2. The motional trajectories in the phase space are shown in Fig. 6.7 (a). The number of the constraints in Eq. (6-7) increases quadratically with the number of the qubits and reaches to six in the 4-qubit case, as shown in Fig. 6.7 (b).

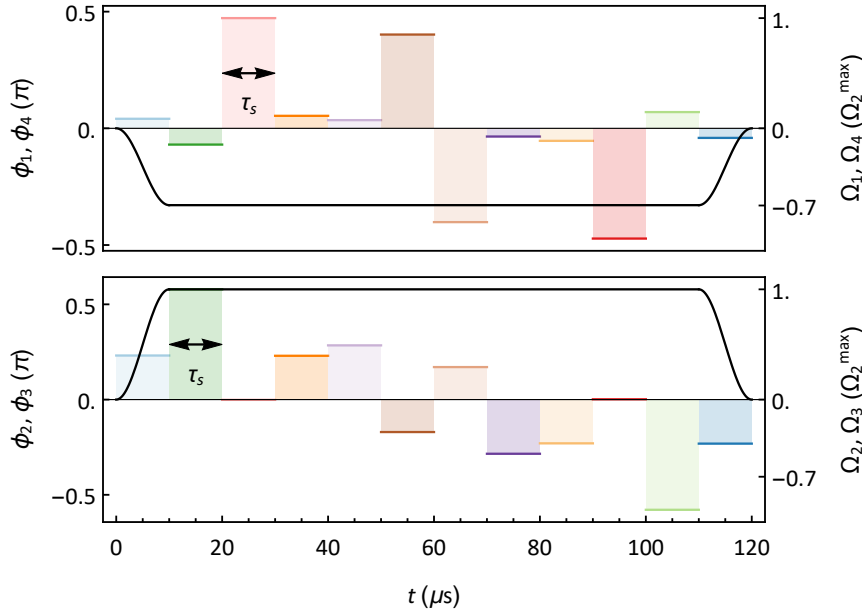
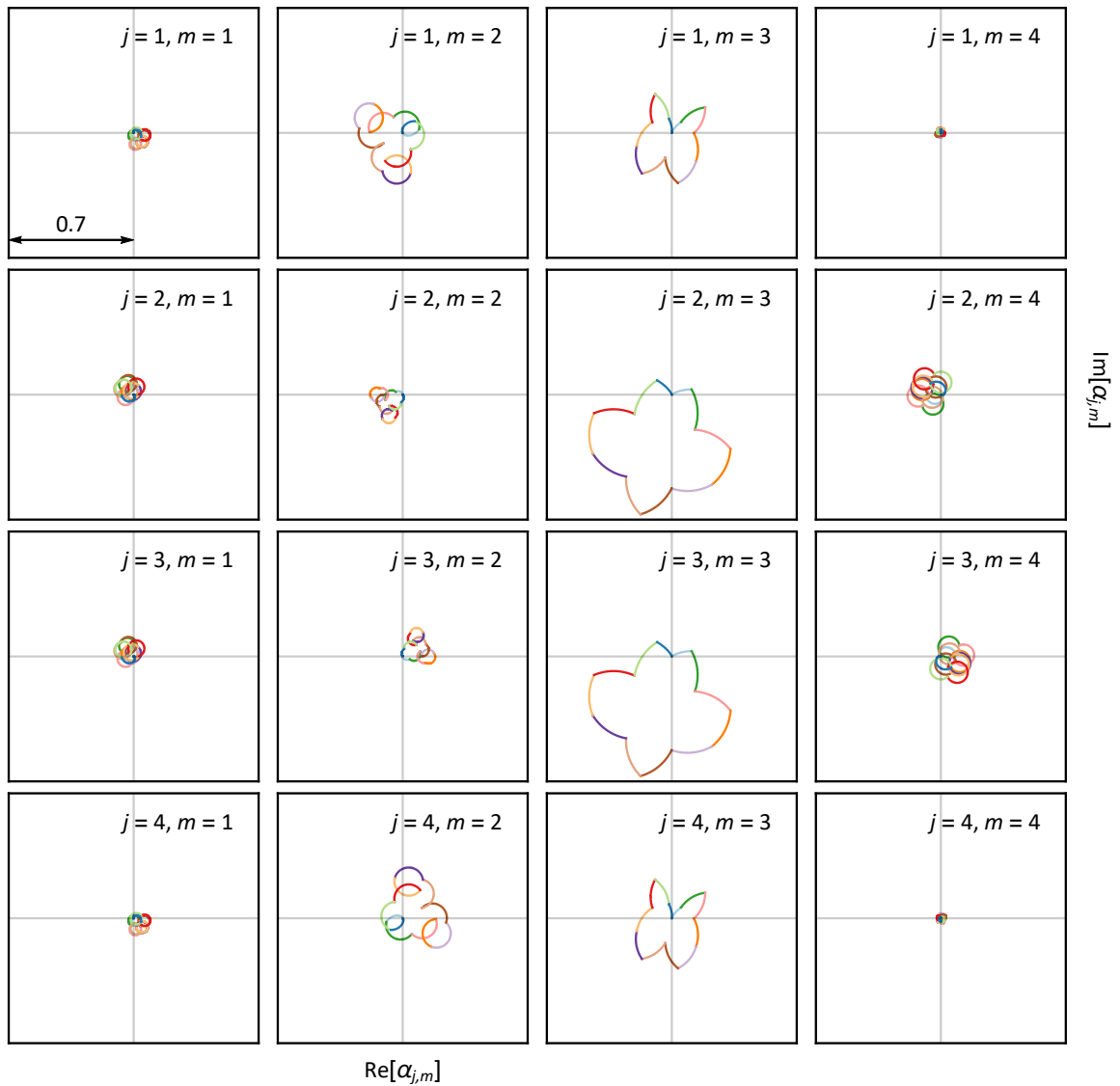
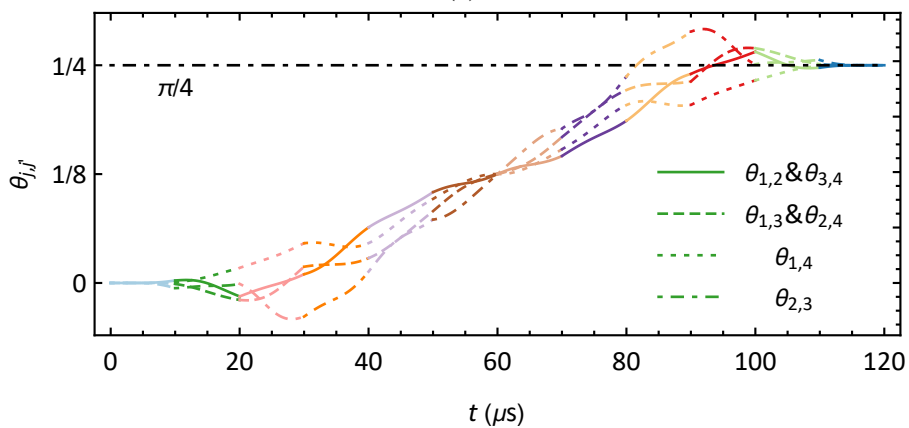


Figure 6.6 Pulse scheme with phase and amplitude modulation. Using the symmetry of the system, we set the modulation patterns to be the same for the outer two qubits,  $\{1, 4\}$ , and the inner two qubits,  $\{2, 3\}$ .



(a)



(b)

Figure 6.7 Visualization of satisfaction of constraints for four-qubit global entangling gate. (a) Motional trajectories  $\alpha_{j,m}$  in phase space for the global four-qubit entangling gate. (b) Accumulation of coupling strength  $\theta_{j,j'}$  over the evolution time.

By applying the global 4-qubit entangling gate to all the qubits, we successfully generate the 4-qubit GHZ state with the state fidelity of  $(93.4 \pm 2.0)\%$ , as shown in Fig. 6.8 (a). Similarly, we can prepare the 3-qubit GHZ state or the 2-qubit GHZ state by only addressing arbitrary three or two qubits, respectively. Experimentally we choose the qubits of  $\{2, 3, 4\}$  to prepare the 3-qubit GHZ state and the qubit-pair of  $\{1, 3\}$  to prepare the 2-qubit GHZ state, with the state fidelities of  $(94.2 \pm 1.8)\%$  and  $(95.1 \pm 1.6)\%$ , respectively, as shown in Fig. 6.8 (b)-(c).

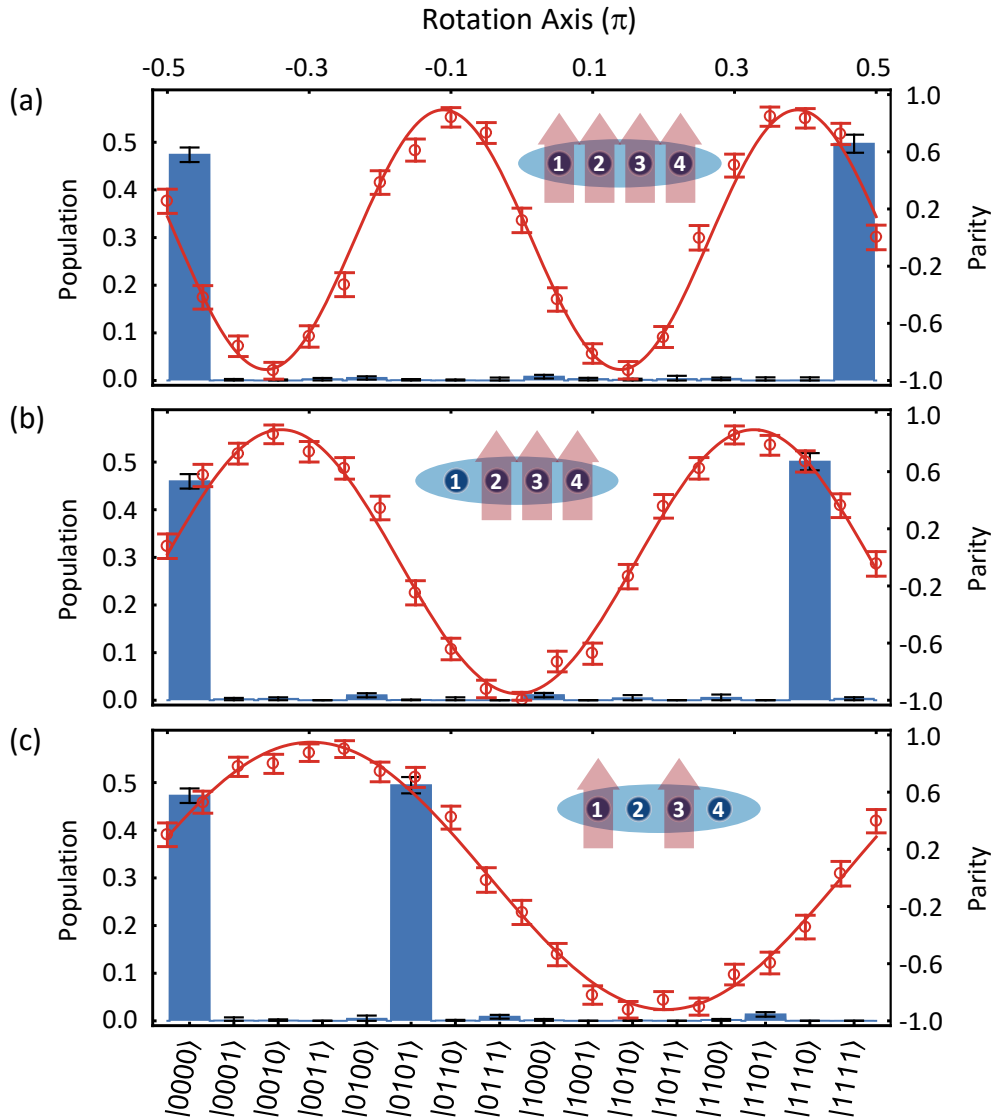


Figure 6.8 GHZ states prepared by the global entangling gates. By addressing an arbitrary subset of qubits—for example,  $\{1, 2, 3, 4\}$ ,  $\{2, 3, 4\}$  and  $\{1, 3\}$ —we can apply the entangling gate on the subset. The frequency of the parity oscillation, which is proportional to the number of addressed qubits, reveals that the prepared state is the GHZ state.

Table 6.2 Pulse scheme for the global 4-qubit entangling gate

qubit $j$		1	2	3	4
$\Omega_j^{\max}$ (MHz)		$-2\pi \times 0.117$	$2\pi \times 0.168$	$2\pi \times 0.168$	$-2\pi \times 0.117$
$\phi_{j,k}(\pi)$	1	0.041	0.231	0.231	0.041
	2	-0.070	0.579	0.579	-0.070
	3	0.472	-0.001	-0.001	0.472
	4	0.054	0.230	0.230	0.054
	5	0.035	0.285	0.285	0.035
	6	0.402	-0.170	-0.170	0.402
	7	-0.402	0.170	0.170	-0.402
	8	-0.035	-0.285	-0.285	-0.035
	9	-0.054	-0.230	-0.230	-0.054
	10	-0.472	0.001	0.001	-0.472
	11	0.070	-0.579	-0.579	0.070
	12	-0.041	-0.231	-0.231	-0.041

All of the results are calibrated to remove the detection errors. The state fidelities of all the prepared GHZ states are mainly limited by the fluctuations of the tightly focused individual beams and the optical paths jittering of the Raman beams ( $2 \sim 4\%$ ). Other infidelity sources in the experiment include the drifting of the motional frequencies ( $1 \sim 2\%$ ) and the crosstalk of the individual beams to the nearby ions ( $\sim 1\%$ ). Moreover, the weak coupling to the y-direction slightly excite the corresponding collective motional modes, while the high average phonon number after Doppler cooling would amplify the errors induced from the unclosed trajectories. Meanwhile, the anharmonicity in the axial potential may lead the experimental Lamb-Dicke parameters to be different from the theoretically used one, resulting in certain infidelity in the real experiment. The amplitude noise when we suddenly alternate the optical phase of the 1st order diffractive beam from the AOM would also introduce certain error in the gate operation, due to the limited bandwidth of the AOM. The future improvements may consider to continuously modulate laser parameters, which is much more friendly to physical devices.

#### 6.4 Algorithm demonstration: digitized adiabatic evolution

Adiabatic quantum computation (AQC) is one promising branch of quantum computing, playing an important role in the optimization and the combinatorial search problem<sup>[167-168]</sup>. The core of the AQC, the adiabatic evolution, relies on the adiabatic theo-

rem<sup>[7]</sup>. For a conventional analog adiabatic evolution, we first prepare the ground state of the initial Hamiltonian  $H_{\text{ini}}$ , and then apply the adiabatic evolution of

$$H(t) = \left(1 - \frac{t}{\tau_{\text{ad}}}\right) H_{\text{ini}} + \frac{t}{\tau_{\text{ad}}} H_{\text{fin}}. \quad (6-33)$$

Here the Hamiltonian is slowly varied from the initial  $H_{\text{ini}}$  to the final target  $H_{\text{fin}}$  over the duration of  $\tau_{\text{ad}}$ . According to the adiabatic theorem, as long as  $t_{\text{ad}}$  is much large than the inverse of the minimal energy gap between the ground state and first excited state, the final state can be well approximated as the ground state of the Hamiltonian  $H_{\text{fin}}$ . However, in practice, it is always difficult to program the final target Hamiltonian to be arbitrary form in an analog way. Instead, we move to a digital way<sup>[169]</sup>.

To achieve a digitized adiabatic evolution, we first decompose the continuous time evolution into several sequentially applied discrete time evolutions,

$$\begin{aligned} U(\tau_{\text{ad}}) &= \mathcal{T} \exp \left[ -i \int_0^{\tau_{\text{ad}}} H(t) dt \right] \\ &\approx \exp [-iH(t_p)\Delta t] \dots \exp [-iH(t_2)\Delta t] \exp [-iH(t_1)\Delta t], \end{aligned} \quad (6-34)$$

where  $p$  is the number of divided sections,  $\Delta t = \tau_{\text{ad}}/p$  and  $t_i = i\Delta t$  ( $i = 1, 2, \dots, p$ ). For each discrete time evolution, it is achieved by utilizing the standard Trotter decomposition,

$$\exp [-iH(t_i)\Delta t] \approx \left( \exp \left[ -iA_{1,i} \frac{\Delta t}{2n} \right] \exp \left[ -iA_{2,i} \frac{\Delta t}{n} \right] \exp \left[ -iA_{1,i} \frac{\Delta t}{2n} \right] \right)^n, \quad (6-35)$$

where  $H(t_i) = A_{1,i} + A_{2,i}$ . This is a second-order Trotterization and  $n$  is the number of Trotter steps<sup>[20]</sup>. In detail, the operators  $A_{1,i}$  and  $A_{2,i}$  here can be written as,

$$A_{1,i} = \left(1 - \frac{t_i}{\tau_{\text{ad}}}\right) H_{\text{ini}}, \quad (6-36)$$

$$A_{2,i} = \frac{t_i}{\tau_{\text{ad}}} H_{\text{fin}}. \quad (6-37)$$

In principle, we can further decompose Eq. (6-35) into gate operations, indicating that the final Hamiltonian  $H_{\text{fin}}$  can be fully programmable. Therefore, we can employ a universal quantum computer to realize arbitrary adiabatic evolution in the digital way.

For the experimental demonstration, we adiabatically prepare the ground state of a fully connected Ising model with three spins by choosing,

$$H_{\text{ini}} = B \sum_{j=1}^3 \sigma_y^j, \quad (6-38)$$



$$H_{\text{fin}} = J \sum_{j < j'} \sigma_x^j \sigma_x^{j'}. \quad (6-39)$$

Due to the limited fidelities of our gate operations, we set  $p = 4$  and  $n = 1$ , respectively. The decomposed quantum circuit is shown in Fig. 6.9. Note that, by utilizing the conventional universal gate set, the final Hamiltonian  $H_{\text{fin}}$  should be decomposed into three two-qubit gates, while here we can achieve it with a single global 3-qubit entangling gate. In the experimental realization, we set  $J$  to be  $-1.0$  while  $B$  to be  $-1.2$ , making the final Hamiltonian to be the ferromagnetic Ising model. Therefore, the ground state of  $H_{\text{fin}}$  refers to a 3-qubit GHZ state. We can quantify the overlap between the theoretical ground state and the experimental final state, by measuring its population and parity oscillation, as shown in Fig. 6.10. The population occupied in the states of  $|000\rangle$  and  $|111\rangle$ , and the contrast of the parity oscillation are 83.9% and 71.9%, respectively, revealing the ground state fidelity of 77.9%. The theoretical state fidelities are 96.6% and 94.1% by utilizing the ideal analog and digitized ways, respectively. The experimental result is mainly limited by the fidelity of the global entangling gate ( $94.1\% \times (95.2\%)^4 \approx 77.2\%$ ).

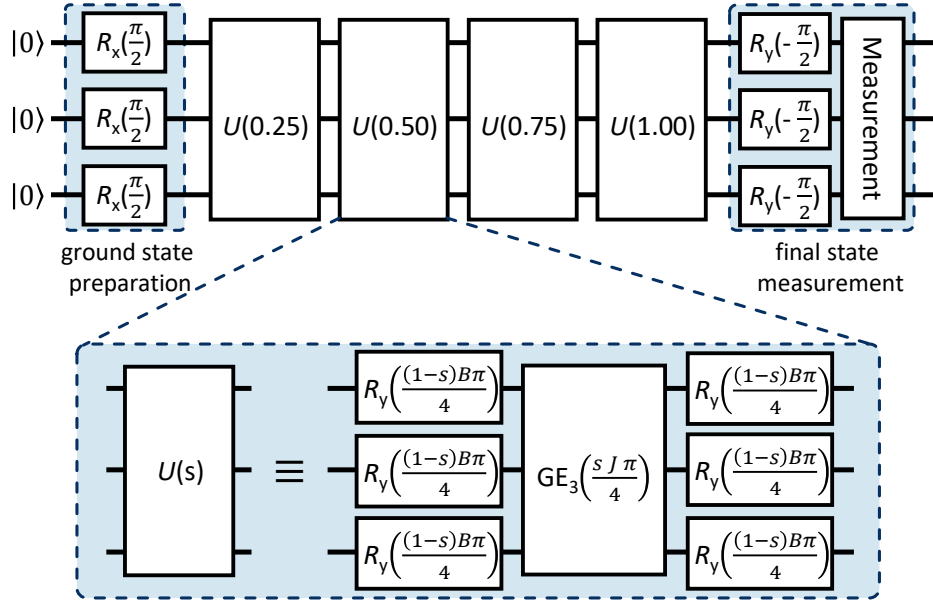


Figure 6.9 Quantum circuit for digitized adiabatic evolution. The preparation of the initial ground state of  $H_{\text{ini}}$  is achieved by the single-qubit rotations  $R_x(\pi/2)$  on all the qubits, while the final measurement is applied after rotating the state from the  $\sigma_x$ -basis to the  $\sigma_z$ -basis. The evolution operator in each step can be decomposed into a global 3-qubit entangling gate sandwiched by the single-qubit rotations with proper rotation angles. The duration of the adiabatic evolution  $\tau_{\text{ad}}$  is set to be  $\pi$ .

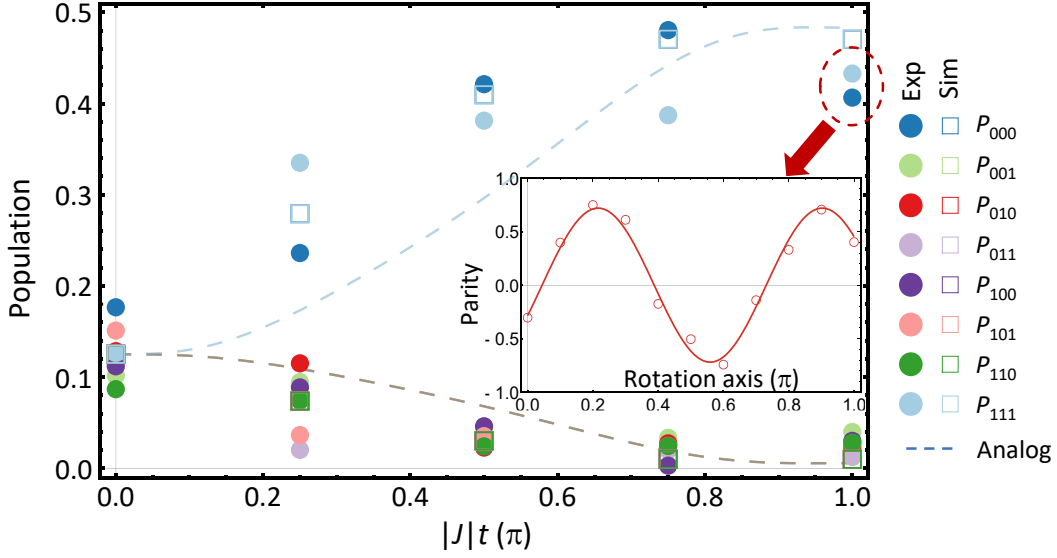


Figure 6.10 Ground state of the ferromagnetic Ising model. The figure shows the population on each qubit state in each Trotterization step. During the adiabatic evolution, the populations accumulate to the states of  $|000\rangle$  and  $|111\rangle$ , which are the degenerate ground states of the final Hamiltonian. The inset figure shows the parity oscillation of the prepared state in the final step (marked in the red dashed circle). The contrast of the oscillation surpasses the classical boundary, indicating the genuine entanglement between the different degenerate ground states.

Compared with the previous analog demonstration in the trapped-ion system<sup>[170-171]</sup>, our results reveal significant improvement. The conventional adiabatic evolution of the transverse Ising model in the trapped-ion system suffers from the effect of the phonon excitation seriously. Therefore, the contrast of the parity oscillation drops to 47% even with just three ions<sup>[171]</sup>. On the contrary, the digitized evolution totally gets rid of this problem, because we close all the motional trajectories in each step to remove the phonon excitation. Although we can also realize the arbitrary lattice<sup>[172]</sup> in the analog evolution, it is much more complicated than the digitized programming. Moreover, the fault-tolerant techniques allow the digitized adiabatic evolution to be error-free in the future<sup>[169]</sup>, making it more scalable and practicable.

## 6.5 Discussion

### 6.5.1 Comparison of single-mode and multimode approaches

The implementation of global entangling gates would be straightforward if we can only drive the COM mode, either in the axial or radial direction<sup>[12,56,157]</sup>. The homogeneous ion-motion couplings of the COM modes,  $\eta_{j,1} = \eta_{\text{COM}}$ , make all of the coupling strengths

$\theta_{j,j'}(\tau)$  uniform as

$$\theta_{j,j'}(\tau) = -\frac{\eta_{\text{COM}}^2 \Omega^2 \tau}{2\delta_1}, \quad (6-40)$$

ensuring  $\alpha_{j,1}(\tau) = 0$  at time  $\tau = 2\pi/|\delta_1|$  with the condition of  $\Omega_j(t) = \Omega$  and  $\phi_j(t) = 0$  for all the ions. However, due to the bunching of an increasing number of motional modes and their crosstalk when the number of ions increases, we have to dramatically slow down the gate speed to isolate the COM mode<sup>[138]</sup>. Otherwise, it is inevitable to drive the rest of the modes. Either of them would decrease the gate fidelity, due to the limited coherence time or the undesired inhomogeneous couplings. In detail, if we include the contribution from the nearest second mode, the coupling strength should modified to be,

$$\theta_{j,j'} = -\frac{\delta_1}{|\delta_1|} \frac{\pi(r-1)^2 \eta_{\text{COM}}^2 \Omega^2}{\Delta\nu^2} \left( 1 + \frac{\eta_{j,2} \eta_{j',2}}{r \eta_{\text{COM}}^2} \right), \quad (6-41)$$

where  $\Delta\nu = |\nu_1 - \nu_2|$  is the frequency difference of the two modes. The gate duration  $\tau$  is  $2\pi|\delta_1|^{-1} = 2\pi|r-1|\Delta\nu^{-1}$ . To close the trajectories of both modes simultaneously, we let  $\delta_2/\delta_1$  to be an integer  $r$ . The inhomogeneous  $\eta_{j,2}$  would imbalance the coupling strengths. We numerically evaluate the fidelities of the created GHZ states by calculating

$$\mathcal{F} = \left| \langle 0..0 | \text{GE}_N^\dagger(\pi/4) \exp \left[ -i \sum_{j < j'} \theta_{j,j'} \sigma_x^j \sigma_x^{j'} \right] | 0..0 \rangle \right|^2, \quad (6-42)$$

with the radial trap frequency of  $2\pi \times 2.18$  MHz and the axial trap frequency varying from  $2\pi \times 0.5$  MHz (for 3 ions) to  $2\pi \times 0.32$  MHz (for 6 ions). These values are consistent to the experimental conditions that the average spacing of the nearby ions is around  $4.7 \mu\text{m}$ . It is difficult to perform a decent quantum gate with single axial COM mode at such low axial trap frequencies, due to high heating rates and poor ground state cooling. The gate fidelity would seriously be degraded as the number of ions increases. Therefore, we only consider to utilize the radial COM mode for the single-mode method. The results of the numerical simulation are summarized in the Fig. 6.11.

As shown in the figure, to achieve a certain value of the state fidelity, the minimal gate duration increases  $\sim N^{2.4}$  as the number of the ions increases. We note that, we do not include the other modes in the simulation, which would lead to further decrease of the fidelity. On the contrary, in our multi-mode approach, we consider the effects of all the modes. The gate duration increases nearly linear with the number of ions with unity of the theoretical fidelity. The comparably shorter gate duration would suppress the

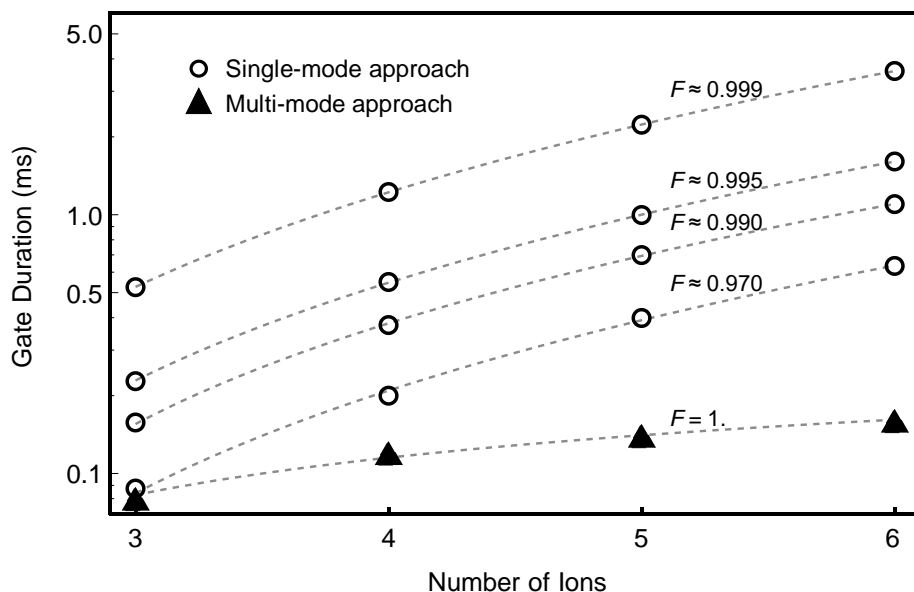


Figure 6.11 Comparison of gate durations between single- and multiple-mode approaches. For the given trap frequencies, the gate duration  $\tau$  of the single-mode approach grows more than linearly ( $\tau \propto N^{2.4}$ ) to keep the fidelity when the number of ions  $N$  increases. The gate duration of the multi-mode approach grows near linearly with unity of the theoretical fidelity. The vertical axis is a logarithmic scale.

infidelities from the limited coherence time, the Raman scattering, motional heating and so on. Moreover, the COM modes suffer from electrical noise more seriously, and the heating rates increase with the number of ions<sup>[81]</sup>, which would further degrade the gate fidelity. Therefore, in the experimental realization, we always choose  $\mu$  to be away from the COM mode.

### 6.5.2 Conclusion

We present the experimental realization of the global entangling gates, which can make the quantum circuit efficient, in scalable approach on the trapped-ion platform. The duration of a single global gate is comparable to that of a single pairwise gate with the same total number of ions<sup>[138]</sup>. We conjecture that the duration of the gate is mainly affected by the density of the motional spectrum, instead of the number of the qubits we desire to entangle. The crowder the frequencies of the motional modes are, the longer the gate would be. Therefore, we clearly observe the speedups of the global gates in total gate counts and duration.

Moreover, we theoretically optimize the pulse schemes for the five and six qubits, and we find the required number of segments and the gate duration increase linearly with the

number of qubits. Therefore, this approach shows well scalability even with an ion-chain consisting of plenties of ions. As long as the solutions to the optimization problem are found, we could extend and apply the global entangling gate to a further number of qubits. However, the general form of the pulse optimization with a large number of qubits belongs to NP-hard problems, but could be assisted by classical machine learning technique. Note that, in a recent preprint, the researchers develop a systematic method called "EASE" to construct arbitrary simultaneously entangling gates<sup>[173]</sup>. With the help of this protocol, modulated pulsed schemes can be efficiently constructed, with the number of segments linearly scaling with the size of system. Furthermore, by extending the global entangling gate to a general form with arbitrary coupling strengths of  $\{\theta_{j,j'}(\tau) = \Theta_{j,j'}\}$ <sup>[173-174]</sup>, we could further simplify quantum circuits for large-scale quantum computation and simulation.

## Chapter 7 Conclusion and Outlook

Here, we come to the end of this thesis. In my whole Ph.D. life, I started from the manipulation on a single trapped-ion, and utilized the single-ion system to experimentally study a certain topics of quantum thermodynamics. Then I gradually moved to the realization of a multi-qubit system, constructing the individual laser addressing system. Finally we achieved a small-scale but fully controllable quantum computing system. Based on such a platform, I theoretically and experimentally explore the possibility of apply global entangling gate through multiple motional modes. During these years, I have participated in plenties of researches on quantum simulation and quantum computation as well, not limited to the projects which I led then list in this thesis. However, we just near the entrance of the NISQ era, and it is still far away from ultimate fault-tolerant quantum computation. From my perspective, several directions are worthwhile to follow in the next stage to achieve a more practical quantum computing system.

### **Fast&robust gate**

For scalable quantum computation, we expect that error rates of gate operations would not increase as the system scaling up. However, according to current best records on the experiments, the gate performance, especially for two-qubit entangling gates, does degrade when the number of ions increases. The infidelity of a two-qubit gate can be suppressed to be less than  $10^{-3}$  with a two-ion system, but increase to  $> 10^{-2}$  when being extended to 11 qubits. Although the motion mediated entangling gate provides us the feature of full-connectivity, possible errors induced by the increasing number of motional mode would also challenge us in improving gate performance. Various pulse shaping methods, which demonstrated recently inspire us to construct a more robust gate insensitive to specific noises, and we had better figure out what kind of pulse shaping is the best for both the theoretical construction and experimental implementation. Moreover, the combination of classical machine learning and real-time feedback may help us to improve gate performance automatically.

Another aspect is the speed-up of gate operations. Compared with solid systems, the strengths of ion-laser interactions are much weaker. Recently progresses in ultra-fast gates are pretty attractive, indicating the possibility of achieving a GHz running-speed even in

trapped-ion platforms. Therefore, gate schemes beyond the Lamb-Dicke approximation should be carefully considered and further developed. Moreover, we should explore a more efficient tool to characterize system noises and gate performance when we deal with an intermediate or even large scale system.

### **Integrated trapped-ion system**

Another technique direction of the trapped-ion based quantum computing is system integration. The enlightenment of the development of modern electronic technology is that integration is an effective way to achieve a large-scale robust system. Currently, the progress of integration in the trapped-ion community mainly focuses on micro-surface or chip traps, in which the positions of ions can be precisely controlled with the help of a large amount of micro-electrodes. Challenges in such micro-traps include the anomalous heating and the dielectric charging by UV lasers. The mechanism of the anomalous heating is still under exploring and urgently needs to be solved.

The technique of optical waveguide provides an idea of integrating not only electronics but also optical elements on-chip<sup>[68]</sup>. The on-chip optical system would significantly suppress the phase noise due to the jittering in free space, ensuring a long-term phase stability. Meanwhile, with the help of micro-grating, the laser focusing close to the diffractive limitation can be achievable<sup>[175]</sup>. Therefore, we might obtain extremely high intensities without considerable power of laser beams, which is critical for the realization of ultra-fast gates. Moreover, other integration techniques, such as detection by nano-wire, might further make trapped-ion quantum computers more practicable in the near future.

## Reference

- [1] Wheeler J A. Information, physics, quantum: the search for links[J]. Complexity, Entropy, and the Physics of Information, 1990, 8.
- [2] Deutsch D. It from qubit[J]. Science and Ultimate Reality. Quantum Theory, Cosmology, and Complexity, 2004: 90-102.
- [3] Feynman R P. Simulating physics with computers[J]. International Journal of Theoretical Physics, 1982, 21(6): 467-488.
- [4] Shor P W. Polynomial-time algorithms for prime factorization and discrete logarithms on a quantum computer[J]. SIAM Review, 1999, 41(2): 303-332.
- [5] Lloyd S. Universal quantum simulators[J]. Science, 1996: 1073-1078.
- [6] Benioff P. The computer as a physical system: A microscopic quantum mechanical hamiltonian model of computers as represented by turing machines[J]. Journal of Statistical Physics, 1980, 22(5): 563-591.
- [7] Farhi E, Goldstone J, Gutmann S, et al. Quantum computation by adiabatic evolution[J]. arXiv preprint quant-ph/0001106, 2000.
- [8] Coppersmith D. An approximate Fourier transform useful in quantum factoring[J]. arXiv preprint quant-ph/0201067, 2002.
- [9] DiVincenzo D P. The physical implementation of quantum computation[J]. Fortschritte der Physik: Progress of Physics, 2000, 48(9-11): 771-783.
- [10] Langer C, Ozeri R, Jost J D, et al. Long-lived qubit memory using atomic ions[J]. Physical Review Letters, 2005, 95(6): 060502.
- [11] Wang Y, Um M, Zhang J, et al. Single-qubit quantum memory exceeding ten-minute coherence time[J]. Nature Photonics, 2017, 11(10): 646.
- [12] Monz T, Schindler P, Barreiro J T, et al. 14-qubit entanglement: creation and coherence[J]. Physical Review Letters, 2011, 106(13): 130506.
- [13] Kaufmann H, Ruster T, Schmiegelow C T, et al. Scalable creation of long-lived multipartite entanglement[J]. Physical Review Letters, 2017, 119(15): 150503.
- [14] Harty T, Allcock D, Ballance C J, et al. High-fidelity preparation, gates, memory, and readout of a trapped-ion quantum bit[J]. Physical Review Letters, 2014, 113(22): 220501.
- [15] Gaebler J P, Tan T R, Lin Y, et al. High-fidelity universal gate set for  ${}^9\text{Be}^+$  ion qubits[J]. Physical Review Letters, 2016, 117(6): 060505.
- [16] Debnath S, Linke N M, Figgatt C, et al. Demonstration of a small programmable quantum computer with atomic qubits[J]. Nature, 2016, 536(7614): 63.
- [17] Wright K, Beck K, Debnath S, et al. Benchmarking an 11-qubit quantum computer[J]. arXiv preprint arXiv:1903.08181, 2019.
- [18] Shor P W. Fault-tolerant quantum computation[C]//Proceedings of 37th Conference on Foundations of Computer Science. [S.l.]: IEEE, 1996: 56-65.



- [19] Preskill J. Fault-tolerant quantum computation[M]//Introduction to quantum computation and information. [S.l.]: World Scientific, 1998: 213-269
- [20] Nielsen M A, Chuang I L. Quantum computation and quantum information: 10th anniversary edition[M]. [S.l.]: Cambridge University Press, 2010
- [21] Yung M H, Casanova J, Mezzacapo A, et al. From transistor to trapped-ion computers for quantum chemistry[J]. Scientific Reports, 2014, 4: 3589.
- [22] Farhi E, Goldstone J, Gutmann S. A quantum approximate optimization algorithm[J]. arXiv preprint arXiv:1411.4028, 2014.
- [23] Li Y, Benjamin S C. Efficient variational quantum simulator incorporating active error minimization[J]. Physical Review X, 2017, 7(2): 021050.
- [24] Temme K, Bravyi S, Gambetta J M. Error mitigation for short-depth quantum circuits[J]. Physical Review Letters, 2017, 119(18): 180509.
- [25] Preskill J. Quantum computing in the nisq era and beyond[J]. Quantum, 2018, 2: 79.
- [26] Paul W. Electromagnetic traps for charged and neutral particles[J]. Reviews of Modern Physics, 1990, 62(3): 531.
- [27] Dehmelt H. Experiments with an isolated subatomic particle at rest[J]. Reviews of Modern Physics, 1990, 62(3): 525-530.
- [28] Ramsey N F. Experiments with separated oscillatory fields and hydrogen masers[J]. Reviews of Modern Physics, 1990, 62(3): 541.
- [29] Neuhauser W, Hohenstatt M, Toschek P, et al. Optical-sideband cooling of visible atom cloud confined in parabolic well[J]. Physical Review Letters, 1978, 41(4): 233.
- [30] Wineland D J, Drullinger R E, Walls F L. Radiation-pressure cooling of bound resonant absorbers[J]. Physical Review Letters, 1978, 40(25): 1639.
- [31] Wineland D, Dehmelt H. Proposed  $10^{14} \delta\nu/\nu$  laser fluorescence spectroscopy on  $Tl^+$  mono-ion oscillator III (side band cooling)[J]. Bulletin of the American Physical Society, 1975, 20(4): 637-637.
- [32] Hänsch T W, Schawlow A L. Cooling of gases by laser radiation[J]. Optics Communications, 1975, 13(1): 68-69.
- [33] Neuhauser W, Hohenstatt M, Toschek P, et al. Localized visible  $Ba^+$  mono-ion oscillator[J]. Physical Review A, 1980, 22(3): 1137.
- [34] Wineland D, Itano W M. Spectroscopy of a single  $Mg^+$  ion[J]. Physics Letters A, 1981, 82(2): 75-78.
- [35] Bergquist J, Hulet R G, Itano W M, et al. Observation of quantum jumps in a single atom[J]. Physical Review Letters, 1986, 57(14): 1699.
- [36] Nagourney W, Sandberg J, Dehmelt H. Shelved optical electron amplifier: Observation of quantum jumps[J]. Physical Review Letters, 1986, 56(26): 2797.
- [37] Blatt R, Zoller P. Quantum jumps in atomic systems[J]. European Journal of Physics, 1988, 9 (4): 250.
- [38] Diedrich F, Peik E, Chen J, et al. Observation of a phase transition of stored laser-cooled ions [J]. Physical Review Letters, 1987, 59(26): 2931.

- [39] Wineland D J. Nobel lecture: superposition, entanglement, and raising Schrödinger's cat[J]. *Reviews of Modern Physics*, 2013, 85(3): 1103.
- [40] Earnshaw S. On the nature of the molecular forces which regulate the constitution of the luminiferous ether[J]. *Transactions of the Cambridge Philosophical Society*, 1842, 7: 97-112.
- [41] Leibfried D, Blatt R, Monroe C, et al. Quantum dynamics of single trapped ions[J]. *Reviews of Modern Physics*, 2003, 75(1): 281.
- [42] Berkeland D, Miller J, Bergquist J C, et al. Minimization of ion micromotion in a Paul trap[J]. *Journal of Applied Physics*, 1998, 83(10): 5025-5033.
- [43] James D F. Quantum dynamics of cold trapped ions with application to quantum computation [J]. *Applied Physics B: Lasers and Optics*, 1998, 66(2): 181-190.
- [44] Lin G D, Zhu S L, Islam R, et al. Large-scale quantum computation in an anharmonic linear ion trap[J]. *Europhysics Letters*, 2009, 86(6): 60004.
- [45] Bastin S, Lee T E. Ion crystals in anharmonic traps[J]. *Journal of Applied Physics*, 2017, 121 (1): 014312.
- [46] Xie Y, Zhang X, Ou B, et al. Creating equally spaced linear ion string in a surface-electrode trap by feedback control[J]. *Physical Review A*, 2017, 95(3): 032341.
- [47] Wang Y. Development of trapped ion system for quantum computing[D]. P. R. China: Institute for Interdisciplinary Information Sciences (IIIS), Tsinghua University.
- [48] An S. Quantum control in the trapped ion system[D]. P. R. China: Institute for Interdisciplinary Information Sciences (IIIS), Tsinghua University.
- [49] Mizrahi J A. Ultrafast control of spin and motion in trapped ions[D]. USA: Joint Quantum Institute, University of Maryland Department, 2013.
- [50] Macalpine W, Schildknecht R. Coaxial resonators with helical inner conductor[J]. *Proceedings of the IRE*, 1959, 47(12): 2099-2105.
- [51] Johnson K, Wong-Campos J, Restelli A, et al. Active stabilization of ion trap radiofrequency potentials[J]. *Review of Scientific Instruments*, 2016, 87(5): 053110.
- [52] Monroe C, Meekhof D, King B, et al. Demonstration of a fundamental quantum logic gate[J]. *Physical Review Letters*, 1995, 75(25): 4714.
- [53] Lin Y, Gaebler J P, Reiter F, et al. Preparation of entangled states through Hilbert space engineering[J]. *Physical Review Letters*, 2016, 117(14): 140502.
- [54] Barrett M D, DeMarco B, Schaetz T, et al. Sympathetic cooling of  $^9\text{Be}^+$  and  $^{24}\text{Mg}^+$  for quantum logic[J]. *Physical Review A*, 2003, 68(4): 042302.
- [55] Wan Y, Kienzler D, Erickson S D, et al. Quantum gate teleportation between separated qubits in a trapped-ion processor[J]. *Science*, 2019, 364(6443): 875-878.
- [56] Lanyon B P, Hempel C, Nigg D, et al. Universal digital quantum simulation with trapped ions [J]. *Science*, 2011, 334(6052): 57-61.
- [57] Monz T, Nigg D, Martinez E A, et al. Realization of a scalable Shor algorithm[J]. *Science*, 2016, 351(6277): 1068-1070.
- [58] Ballance C, Harty T, Linke N, et al. High-fidelity quantum logic gates using trapped-ion hyperfine qubits[J]. *Physical Review Letters*, 2016, 117(6): 060504.

- [59] Schäfer V, Ballance C, Thirumalai K, et al. Fast quantum logic gates with trapped-ion qubits[J]. *Nature*, 2018, 555(7694): 75.
- [60] Dietrich M R, Avril A, Bowler R, et al. Barium ions for quantum computation[C]//AIP Conference Proceedings: volume 1114. [S.l.]: AIP, 2009: 25-30.
- [61] Dietrich M, Kurz N, Noel T, et al. Hyperfine and optical barium ion qubits[J]. *Physical Review A*, 2010, 81(5): 052328.
- [62] Hucul D, Christensen J E, Hudson E R, et al. Spectroscopy of a synthetic trapped ion qubit[J]. *Physical Review Letters*, 2017, 119(10): 100501.
- [63] Olmschenk S, Younge K C, Moehring D L, et al. Manipulation and detection of a trapped Yb<sup>+</sup> hyperfine qubit[J]. *Physical Review A*, 2007, 76(5): 052314.
- [64] Weidt S, Randall J, Webster S, et al. Trapped-ion quantum logic with global radiation fields[J]. *Physical Review Letters*, 2016, 117(22): 220501.
- [65] Lekitsch B, Weidt S, Fowler A G, et al. Blueprint for a microwave trapped ion quantum computer [J]. *Science Advances*, 2017, 3(2): e1601540.
- [66] Myerson A, Szwed D, Webster S, et al. High-fidelity readout of trapped-ion qubits[J]. *Physical Review Letters*, 2008, 100(20): 200502.
- [67] Noek R, Vrijzen G, Gaultney D, et al. High speed, high fidelity detection of an atomic hyperfine qubit[J]. *Optics Letters*, 2013, 38(22): 4735-4738.
- [68] Bruzewicz C D, Chiaverini J, McConnell R, et al. Trapped-ion quantum computing: Progress and challenges[J]. *Applied Physics Reviews*, 2019, 6(2): 021314.
- [69] Nägerl H, Roos C, Leibfried D, et al. Investigating a qubit candidate: Spectroscopy on the S<sub>1/2</sub> to D<sub>5/2</sub> transition of a trapped calcium ion in a linear paul trap[J]. *Physical Review A*, 2000, 61(2): 023405.
- [70] Yum D, De Munshi D, Dutta T, et al. Optical barium ion qubit[J]. *Journal of the Optical Society of America B*, 2017, 34(8): 1632-1636.
- [71] Fisk P T, Sellars M, Lawn M A, et al. Accurate measurement of the 12.6 GHz "clock" transition in trapped <sup>171</sup>Yb<sup>+</sup> ions[J]. *IEEE transactions on Ultrasonics, Ferroelectrics, and Frequency Control*, 1997, 44(2): 344-354.
- [72] Huntemann N, Okhapkin M, Lipphardt B, et al. High-accuracy optical clock based on the octupole transition in <sup>171</sup>Yb<sup>+</sup>[J]. *Physical Review Letters*, 2012, 108(9): 090801.
- [73] Senko C R. Dynamics and excited states of quantum many-body spin chains with trapped ions [D]. USA: Joint Quantum Institute, University of Maryland Department, 2014.
- [74] Martin W C, Zalubas R, Hagan L. Atomic energy levels-the rare-earth elements. the spectra of lanthanum, cerium, praseodymium, neodymium, promethium, samarium, europium, gadolinium, terbium, dysprosium, holmium, erbium, thulium, ytterbium, and lutetium[R]. [S.l.]: National Standard Reference Data System, 1978.
- [75] Lide D R. Ionization potentials of atoms and atomic ions[J]. *Handbook of Chemistry and Physics*, 1992: 10-211.
- [76] Balzer C, Braun A, Hannemann T, et al. Electrostatically trapped Yb<sup>+</sup> ions for quantum information processing[J]. *Physical Review A*, 2006, 73(4): 041407.
- [77] Foot C J, et al. Atomic physics[M]. [S.l.]: Oxford University Press, 2005

- [78] Ejtemaee S, Haljan P. 3D sisyphus cooling of trapped ions[J]. *Physical Review Letters*, 2017, 119(4): 043001.
- [79] Morigi G, Eschner J, Keitel C H. Ground state laser cooling using electromagnetically induced transparency[J]. *Physical Review Letters*, 2000, 85(21): 4458.
- [80] Roos C, Leibfried D, Mundt A, et al. Experimental demonstration of ground state laser cooling with electromagnetically induced transparency[J]. *Physical Review Letters*, 2000, 85(26): 5547.
- [81] Lechner R, Maier C, Hempel C, et al. Electromagnetically-induced-transparency ground-state cooling of long ion strings[J]. *Physical Review A*, 2016, 93(5): 053401.
- [82] Monroe C, Meekhof D, King B, et al. Resolved-sideband raman cooling of a bound atom to the 3D zero-point energy[J]. *Physical Review Letters*, 1995, 75(22): 4011.
- [83] Roos C, Zeiger T, Rohde H, et al. Quantum state engineering on an optical transition and decoherence in a paul trap[J]. *Physical Review Letters*, 1999, 83(23): 4713.
- [84] Blinov B B, Leibfried D, Monroe C, et al. Quantum computing with trapped ion hyperfine qubits[J]. *Quantum Information Processing*, 2004, 3(1-5): 45-59.
- [85] Wong-Campos J, Johnson K, Neyenhuis B, et al. High-resolution adaptive imaging of a single atom[J]. *Nature Photonics*, 2016, 10(9): 606.
- [86] Berkeland D, Boshier M. Destabilization of dark states and optical spectroscopy in Zeeman-degenerate atomic systems[J]. *Physical Review A*, 2002, 65(3): 033413.
- [87] Seif A, Landsman K A, Linke N M, et al. Machine learning assisted readout of trapped-ion qubits[J]. *Journal of Physics B: Atomic, Molecular and Optical Physics*, 2018, 51(17): 174006.
- [88] Ding Z H, Cui J M, Huang Y F, et al. Fast high-fidelity readout of a single trapped-ion qubit via machine-learning methods[J]. *Physical Review Applied*, 2019, 12(1): 014038.
- [89] Lee P J, Brickman K A, Deslauriers L, et al. Phase control of trapped ion quantum gates[J]. *Journal of Optics B: Quantum and Semiclassical Optics*, 2005, 7(10): S371.
- [90] Craik D A, Linke N, Sepiol M, et al. High-fidelity spatial and polarization addressing of  $^{43}\text{Ca}^+$  qubits using near-field microwave control[J]. *Physical Review A*, 2017, 95(2): 022337.
- [91] James D, Jerke J. Effective Hamiltonian theory and its applications in quantum information[J]. *Canadian Journal of Physics*, 2007, 85(6): 625-632.
- [92] Hayes D, Matsukevich D N, Maunz P, et al. Entanglement of atomic qubits using an optical frequency comb[J]. *Physical Review Letters*, 2010, 104(14): 140501.
- [93] Lee A C, Smith J, Richerme P, et al. Engineering large stark shifts for control of individual clock state qubits[J]. *Physical Review A*, 2016, 94(4): 042308.
- [94] Zhang J. Quantum operation of phonons and entanglement of multi-species ions[D]. P. R. China: Institute for Interdisciplinary Information Sciences (IIIS), Tsinghua University.
- [95] Zhang X, Shen Y, Zhang J, et al. Time reversal and charge conjugation in an embedding quantum simulator[J]. *Nature Communications*, 2015, 6: 7917.
- [96] Lv D, An S, Liu Z, et al. Quantum simulation of the quantum Rabi model in a trapped ion[J]. *Physical Review X*, 2018, 8(2): 021027.
- [97] Shen Y, Lu Y, Zhang K, et al. Quantum optical emulation of molecular vibronic spectroscopy using a trapped-ion device[J]. *Chemical Science*, 2018, 9(4): 836-840.

- [98] Smith A, Lu Y, An S, et al. Verification of the quantum nonequilibrium work relation in the presence of decoherence[J]. *New Journal of Physics*, 2018, 20(1): 013008.
- [99] Jarzynski C. Nonequilibrium equality for free energy differences[J]. *Physical Review Letters*, 1997, 78(14): 2690.
- [100] Jarzynski C. Equalities and inequalities: irreversibility and the second law of thermodynamics at the nanoscale[J]. *Annual Review of Condensed Matter Physics*, 2011, 2(1): 329-351.
- [101] Liphardt J, Dumont S, Smith S B, et al. Equilibrium information from nonequilibrium measurements in an experimental test of Jarzynski's equality[J]. *Science*, 2002, 296(5574): 1832-1835.
- [102] Collin D, Ritort F, Jarzynski C, et al. Verification of the Crooks fluctuation theorem and recovery of RNA folding free energies[J]. *Nature*, 2005, 437(7056): 231.
- [103] Shank E A, Cecconi C, Dill J W, et al. The folding cooperativity of a protein is controlled by its chain topology[J]. *Nature*, 2010, 465(7298): 637.
- [104] Pohorille A, Jarzynski C, Chipot C. Good practices in free-energy calculations[J]. *The Journal of Physical Chemistry B*, 2010, 114(32): 10235-10253.
- [105] Hänggi P, Talkner P. The other QFT[J]. *Nature Physics*, 2015, 11(2): 108.
- [106] Talkner P, Lutz E, Hänggi P. Fluctuation theorems: work is not an observable[J]. *Physical Review E*, 2007, 75(5): 050102.
- [107] Mukamel S. Quantum extension of the Jarzynski relation: analogy with stochastic dephasing [J]. *Physical Review Letters*, 2003, 90(17): 170604.
- [108] Huber G, Schmidt-Kaler F, Deffner S, et al. Employing trapped cold ions to verify the quantum Jarzynski equality[J]. *Physical Review Letters*, 2008, 101(7): 070403.
- [109] Dorner R, Clark S R, Heaney L, et al. Extracting quantum work statistics and fluctuation theorems by single-qubit interferometry[J]. *Physical Review Letters*, 2013, 110(23): 230601.
- [110] Mazzola L, De Chiara G, Paternostro M. Measuring the characteristic function of the work distribution[J]. *Physical Review Letters*, 2013, 110(23): 230602.
- [111] Roncaglia A J, Cerisola F, Paz J P. Work measurement as a generalized quantum measurement [J]. *Physical Review Letters*, 2014, 113(25): 250601.
- [112] Batalhão T B, Souza A M, Mazzola L, et al. Experimental reconstruction of work distribution and study of fluctuation relations in a closed quantum system[J]. *Physical Review Letters*, 2014, 113(14): 140601.
- [113] An S, Zhang J N, Um M, et al. Experimental test of the quantum Jarzynski equality with a trapped-ion system[J]. *Nature Physics*, 2015, 11(2): 193.
- [114] De Roeck W, Maes C. Quantum version of free-energy-irreversible-work relations[J]. *Physical Review E*, 2004, 69(2): 026115.
- [115] Campisi M, Talkner P, Hänggi P. Fluctuation theorem for arbitrary open quantum systems[J]. *Physical Review Letters*, 2009, 102(21): 210401.
- [116] Deffner S, Lutz E. Nonequilibrium entropy production for open quantum systems[J]. *Physical Review Letters*, 2011, 107(14): 140404.
- [117] Zurek W H. Decoherence and the transition from quantum to classical-revisited[J]. *Los Alamos Science*, 2002, 27: 86-109.

- [118] Rastegin A E. Non-equilibrium equalities with unital quantum channels[J]. *Journal of Statistical Mechanics: Theory and Experiment*, 2013, 2013(06): P06016.
- [119] Loreti F, Balantekin A. Neutrino oscillations in noisy media[J]. *Physical Review D*, 1994, 50(8): 4762.
- [120] Chenu A, Beau M, Cao J, et al. Quantum simulation of generic many-body open system dynamics using classical noise[J]. *Physical Review Letters*, 2017, 118(14): 140403.
- [121] Levy A, Torrontegui E, Kosloff R. Action-noise-assisted quantum control[J]. *Physical Review A*, 2017, 96(3): 033417.
- [122] Van Kampen N G. *Stochastic processes in physics and chemistry*[M]. [S.l.]: Elsevier, 1992
- [123] Demirplak M, Rice S A. Adiabatic population transfer with control fields[J]. *The Journal of Physical Chemistry A*, 2003, 107(46): 9937-9945.
- [124] Berry M V. Transitionless quantum driving[J]. *Journal of Physics A: Mathematical and Theoretical*, 2009, 42(36): 365303.
- [125] Kielpinski D, Monroe C, Wineland D J. Architecture for a large-scale ion-trap quantum computer [J]. *Nature*, 2002, 417(6890): 709.
- [126] Monroe C, Raussendorf R, Ruthven A, et al. Large-scale modular quantum-computer architecture with atomic memory and photonic interconnects[J]. *Physical Review A*, 2014, 89(2): 022317.
- [127] Cirac J I, Zoller P. Quantum computations with cold trapped ions[J]. *Physical Review Letters*, 1995, 74(20): 4091.
- [128] Schmidt-Kaler F, Häffner H, Riebe M, et al. Realization of the Cirac-Zoller controlled-NOT quantum gate[J]. *Nature*, 2003, 422(6930): 408.
- [129] Sørensen A, Mølmer K. Quantum computation with ions in thermal motion[J]. *Physical Review Letters*, 1999, 82(9): 1971.
- [130] Sørensen A, Mølmer K. Entanglement and quantum computation with ions in thermal motion [J]. *Physical Review A*, 2000, 62(2): 022311.
- [131] Milburn G, Schneider S, James D. Ion trap quantum computing with warm ions[J]. *Fortschritte der Physik: Progress of Physics*, 2000, 48(9-11): 801-810.
- [132] Wang X, Sørensen A, Mølmer K. Multibit gates for quantum computing[J]. *Physical Review Letters*, 2001, 86(17): 3907.
- [133] Leibfried D, DeMarco B, Meyer V, et al. Experimental demonstration of a robust, high-fidelity geometric two ion-qubit phase gate[J]. *Nature*, 2003, 422(6930): 412.
- [134] Haljan P, Lee P, Brickman K, et al. Entanglement of trapped-ion clock states[J]. *Physical Review A*, 2005, 72(6): 062316.
- [135] Linke N M, Maslov D, Roetteler M, et al. Experimental comparison of two quantum computing architectures[J]. *Proceedings of the National Academy of Sciences*, 2017, 114(13): 3305-3310.
- [136] Zhu S L, Monroe C, Duan L M. Arbitrary-speed quantum gates within large ion crystals through minimum control of laser beams[J]. *Europhysics Letters*, 2006, 73(4): 485.
- [137] Zhu S L, Monroe C, Duan L M. Trapped ion quantum computation with transverse phonon modes[J]. *Physical Review Letters*, 2006, 97(5): 050505.

- [138] Choi T, Debnath S, Manning T, et al. Optimal quantum control of multimode couplings between trapped ion qubits for scalable entanglement[J]. *Physical Review Letters*, 2014, 112(19): 190502.
- [139] Leung P H, Landsman K A, Figgatt C, et al. Robust 2-qubit gates in a linear ion crystal using a frequency-modulated driving force[J]. *Physical Review Letters*, 2018, 120(2): 020501.
- [140] Green T J, Biercuk M J. Phase-modulated decoupling and error suppression in qubit-oscillator systems[J]. *Physical Review Letters*, 2015, 114(12): 120502.
- [141] Milne A R, Edmunds C L, Hempel C, et al. Phase-modulated entangling gates robust against static and time-varying errors[J]. *arXiv preprint arXiv:1808.10462*, 2018.
- [142] Shapira Y, Shaniv R, Manovitz T, et al. Robust entanglement gates for trapped-ion qubits[J]. *Physical Review Letters*, 2018, 121(18): 180502.
- [143] Webb A E, Webster S C, Collingbourne S, et al. Resilient entangling gates for trapped ions[J]. *Physical Review Letters*, 2018, 121(18): 180501.
- [144] Steane A M, Imreh G, Home J P, et al. Pulsed force sequences for fast phase-insensitive quantum gates in trapped ions[J]. *New Journal of Physics*, 2014, 16(5): 053049.
- [145] Wu Y, Wang S T, Duan L M. Noise analysis for high-fidelity quantum entangling gates in an anharmonic linear paul trap[J]. *Physical Review A*, 2018, 97(6): 062325.
- [146] Warring U, Ospelkaus C, Colombe Y, et al. Individual-ion addressing with microwave field gradients[J]. *Physical Review Letters*, 2013, 110(17): 173002.
- [147] Piltz C, Sriarunothai T, Varón A, et al. A trapped-ion-based quantum byte with  $10^{-5}$  next-neighbour cross-talk[J]. *Nature Communications*, 2014, 5: 4679.
- [148] Burrell A H. High fidelity readout of trapped ion qubits[D]. UK: Oxford University, 2010.
- [149] Shen C, Duan L. Correcting detection errors in quantum state engineering through data processing[J]. *New Journal of Physics*, 2012, 14(5): 053053.
- [150] Debnath S. A programmable five qubit quantum computer using trapped atomic ions[D]. USA: Joint Quantum Institute, University of Maryland Department.
- [151] Brown K R, Harrow A W, Chuang I L. Arbitrarily accurate composite pulse sequences[J]. *Physical Review A*, 2004, 70(5): 052318.
- [152] Wimperis S. Broadband, narrowband, and passband composite pulses for use in advanced nmr experiments[J]. *Journal of Magnetic Resonance, Series A*, 1994, 109(2): 221-231.
- [153] Merrill J T, Doret S C, Vittorini G, et al. Transformed composite sequences for improved qubit addressing[J]. *Physical Review A*, 2014, 90(4): 040301.
- [154] Ivanov S S, Ivanov P A, Vitanov N V. Efficient construction of three-and four-qubit quantum gates by global entangling gates[J]. *Physical Review A*, 2015, 91(3): 032311.
- [155] Martinez E A, Monz T, Nigg D, et al. Compiling quantum algorithms for architectures with multi-qubit gates[J]. *New Journal of Physics*, 2016, 18(6): 063029.
- [156] Maslov D, Nam Y. Use of global interactions in efficient quantum circuit constructions[J]. *New Journal of Physics*, 2018, 20(3): 033018.
- [157] Kim K, Chang M S, Islam R, et al. Entanglement and tunable spin-spin couplings between trapped ions using multiple transverse modes[J]. *Physical Review Letters*, 2009, 103(12): 120502.

- [158] Britton J W, Sawyer B C, Keith A C, et al. Engineered two-dimensional ising interactions in a trapped-ion quantum simulator with hundreds of spins[J]. *Nature*, 2012, 484(7395): 489.
- [159] Senko C, Smith J, Richerme P, et al. Coherent imaging spectroscopy of a quantum many-body spin system[J]. *Science*, 2014, 345(6195): 430-433.
- [160] Jurcevic P, Hauke P, Maier C, et al. Spectroscopy of interacting quasiparticles in trapped ions [J]. *Physical Review Letters*, 2015, 115(10): 100501.
- [161] García-Ripoll J J, Zoller P, Cirac J I. Coherent control of trapped ions using off-resonant lasers [J]. *Physical Review A*, 2005, 71(6): 062309.
- [162] Casanova J, Mezzacapo A, Lamata L, et al. Quantum simulation of interacting fermion lattice models in trapped ions[J]. *Physical Review Letters*, 2012, 108(19): 190502.
- [163] Haljan P C, Brickman K A, Deslauriers L, et al. Spin-dependent forces on trapped ions for phase-stable quantum gates and entangled states of spin and motion[J]. *Physical Review Letters*, 2005, 94(15): 153602.
- [164] Roos C F. Ion trap quantum gates with amplitude-modulated laser beams[J]. *New Journal of Physics*, 2008, 10(1): 013002.
- [165] Wang S. Applications of atomic systems in quantum simulation, quantum computation and topological phases of matter[D]. USA: University of Michigan, 2017.
- [166] Sackett C A, Kielpinski D, King B E, et al. Experimental entanglement of four particles[J]. *Nature*, 2000, 404(6775): 256.
- [167] Crosson E, Farhi E, Lin C Y Y, et al. Different strategies for optimization using the quantum adiabatic algorithm[J]. *arXiv preprint arXiv:1401.7320*, 2014.
- [168] Lucas A. Ising formulations of many NP problems[J]. *Frontiers in Physics*, 2014, 2: 5.
- [169] Barends R, Shabani A, Lamata L, et al. Digitized adiabatic quantum computing with a superconducting circuit[J]. *Nature*, 2016, 534(7606): 222.
- [170] Islam R, Edwards E, Kim K, et al. Onset of a quantum phase transition with a trapped ion quantum simulator[J]. *Nature Communications*, 2011, 2: 377.
- [171] Islam K R. Quantum simulation of interacting spin models with trapped ions[D]. USA: Joint Quantum Institute, University of Maryland Department, 2012.
- [172] Korenblit S, Kafri D, Campbell W C, et al. Quantum simulation of spin models on an arbitrary lattice with trapped ions[J]. *New Journal of Physics*, 2012, 14(9): 095024.
- [173] Grzesiak N, Blümel R, Beck K, et al. Efficient arbitrary simultaneously entangling gates on a trapped-ion quantum computer[J]. *arXiv preprint arXiv:1905.09294*, 2019.
- [174] Figgatt C, Ostrander A, Linke N M, et al. Parallel entangling operations on a universal ion-trap quantum computer[J]. *Nature*, 2019, 572(7769): 368-372.
- [175] Mehta K K, Ram R J. Precise and diffraction-limited waveguide-to-free-space focusing gratings [J]. *Scientific Reports*, 2017, 7(1): 2019.



## Acknowledgments

It has been a long time since I joined this lab, which has already been another home. Throughout my whole Ph.D. life, I would like first to express my great appreciation to my supervisor, Prof. Kihwan Kim, for leading me into this fantastic research area. I still remember that when I was still a freshman and knew nothing, you guided me strictly but patiently. With your continuous support, I can grow into a qualified research scientist. Everything I have learned in this invaluable stage would be treasures in my future life.

My sincere thanks also goes Dr. Jing-Ning Zhang, Prof. H. T. Quan, Prof. Christopher Jarzynski and Prof. Hyunchul Nha for all the theoretical collaborations and discussions. Your insights in physics inspire me and broaden my eyes in the relevant researches.

Of course, I am also grateful to all of those guys who work together with me for the past several years: Dahyun Yum, Xiang Zhang, Um Mark, Shuoming An, Dingshun Lv, Yangchao Shen, Ye Wang, Junhua Zhang, Kuan Zhang and Shuaining Zhang. I pretty enjoy the thousands of days and nights working hard with all of you. My thanks and best wishes should also be delivered to the young men in our labs: Pengfei Wang, Wentao Chen, Mu Qiao, Chunyang Luan, Zhengyang Cai and Jialiang Zhang. This is a golden age for all of us.

I would also like to extend my thanks to the undergraduate students who have worked in our labs: Guanhao Huang, Naijun Jin, Tian Xie and Botao Du. Although I did not have much overlap with other experimental groups on work, I am still grateful to all the members in the Center for Quantum Information.

Finally, my particular thanks should give to my parents for their sacrifice in raising me, and their full support in my career. I would try my best to become your proud son. Graduate life is fruitful but also stressful, and I would not have made it without the companion of my cherished wife, Yuyin Yang. I would like to enjoy everything with you in the rest of my life.

## 声 明

本人郑重声明：所呈交的学位论文，是本人在导师指导下，独立进行研究工作所取得的成果。尽我所知，除文中已经注明引用的内容外，本学位论文的研究成果不包含任何他人享有著作权的内容。对本论文所涉及的研究工作做出贡献的其他个人和集体，均已在文中以明确方式标明。

签 名：\_\_\_\_\_ 日 期：\_\_\_\_\_

## Appendix A Electric multipole field

In Chap. 2, we introduce the classical dynamics of a single ion trapped in a quadrupole field oscillating at the RF frequency. In practice, the quadrupole field is generated from the four parallel cylinder electrodes in which the RF voltage and the DC voltage are alternatively applied, as show in Fig. A.1 (a). So what would happen if we increase the number of rods? In Fig. A.1 (b), we give an example of the potential generated from eight electrodes. In the following content, we would estimate the electric potential generated from  $m$ -rod.

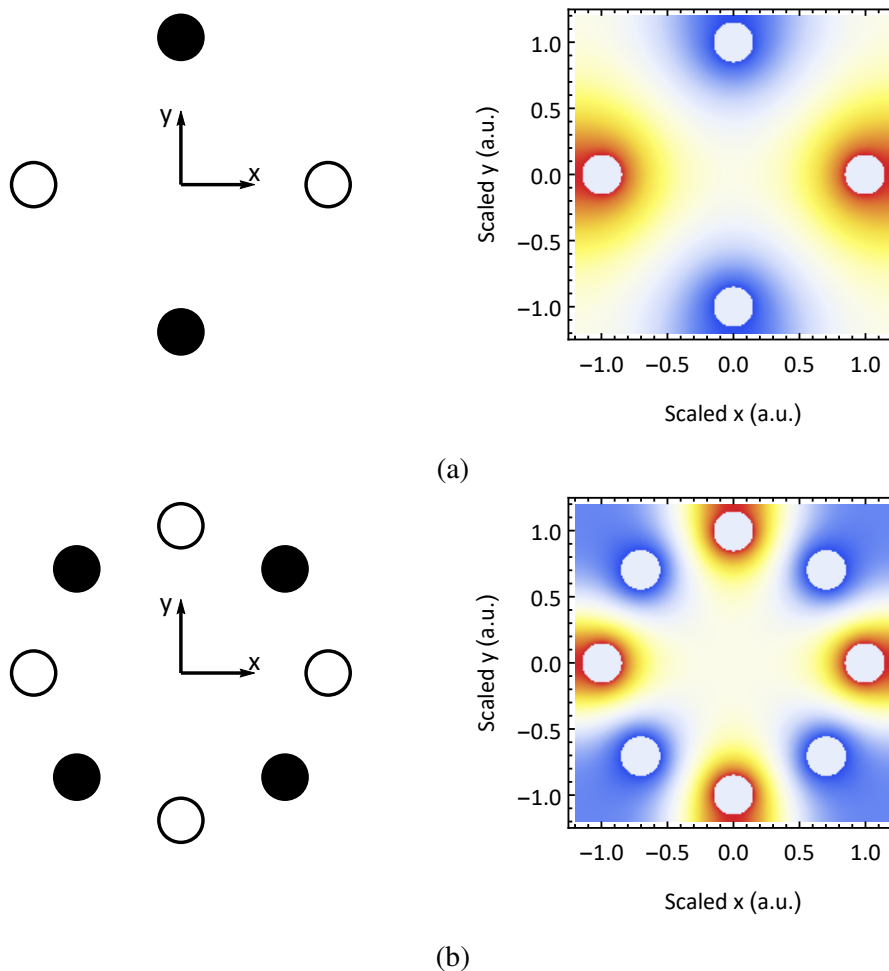


Figure A.1 Electric multipole field. The sub-figures in the left column show the geometric configuration of 4-rod and 8-rod situations. The RF voltage is applied to the white rods while the DC voltage is applied to the black rods. The sub-figures in the right column show the electric potential induced from the rods at a certain time.

Without loss of generality, we assume that  $m$  electrodes are symmetrically arranged in a circle, and  $m$  must be an even number. The electric potential  $\Phi$  near the center position can be expanded into the form of (in the cylindrical coordinate),

$$\Phi(r, \theta) = A_0 + \sum_{n=1}^{\infty} r^n [A_n \cos(n\theta) + B_n \sin(n\theta)], \quad (\text{A-1})$$

where all the  $A_n$  and  $B_n$  are the undetermined coefficients. For convenience, we temporarily ignore the time-dependent part ( $\cos(\Omega_{\text{rf}}t)$ ). We also assume that the length of the rods along the  $z$ -direction is pretty long, hence the electric potential has the translational symmetry along the  $z$ -direction.

Due to the symmetry of the electrode-configuration, we have a set of constraints on the electric potential,

$$\Phi(r, \theta) = (-1)^k \Phi\left(r, \theta + k \frac{2\pi}{m}\right), \quad (\text{A-2})$$

where  $k = 1, 2, 3, \dots, m$ . By inserting Eq. (A-2) into Eq. (A-1) and then setting  $\theta$  to be 0, we would have equations written as,

$$A_n = (-1)^k \left[ A_n \cos\left(nk \frac{2\pi}{m}\right) + B_n \sin\left(nk \frac{2\pi}{m}\right) \right]. \quad (\text{A-3})$$

The above equation clearly shows that  $A_0 = 0$  and  $B_n = 0$ , and the simplified constraints on the coefficients  $A_n$  are

$$A_n \left[ (-1)^k \cos\left(nk \frac{2\pi}{m}\right) - 1 \right] = 0 \quad (\text{A-4})$$

Therefore, the value of  $A_n$  can be non-zero only when the equations of,

$$(-1)^k \cos\left(nk \frac{2\pi}{m}\right) - 1 = 0, \quad (\text{A-5})$$

are satisfied for all the  $k$ . Apparently, the minimal value of  $n$  is equal to  $m/2$ , which means that the first non-zero coefficient is  $A_{m/2}$ . After neglecting other higher order contributions, the electric potential generated from  $m$  rods can be approximated as,

$$\Phi(r, \theta) \sim r^{m/2} \cos\left(\frac{m}{2}\theta\right). \quad (\text{A-6})$$

When  $m = 4$ , we would have the quadratic potential,

$$\Phi(r, \theta) \sim r^2 \cos(2\theta) = x^2 - y^2. \quad (\text{A-7})$$

To obtain the pseudo-potential when the electric potential oscillates at the RF frequency,  $\Phi(t) \rightarrow \Phi(t) \cos(\Omega_{\text{rf}}t)$ , we calculate the electric field induced from the potential Eq. (A-6),

$$\begin{aligned}\vec{E}(r, \theta) &= -\frac{\partial \Phi}{\partial r} \vec{e}_r - \frac{1}{r} \frac{\partial \Phi}{\partial \theta} \vec{e}_\theta \\ &\sim -\frac{m}{2} r^{m/2-1} \cos\left(\frac{m}{2}\theta\right) \vec{e}_r + \frac{m}{2} r^{m/2-1} \sin\left(\frac{m}{2}\theta\right) \vec{e}_\theta.\end{aligned}\quad (\text{A-8})$$

Therefore, the final pseudo-potential generated from  $m$  rods turns out to be,

$$\Phi_p \sim |\vec{E}|^2 \sim (r^2)^{m/2-1} = (x^2 + y^2)^{m/2-1}.\quad (\text{A-9})$$

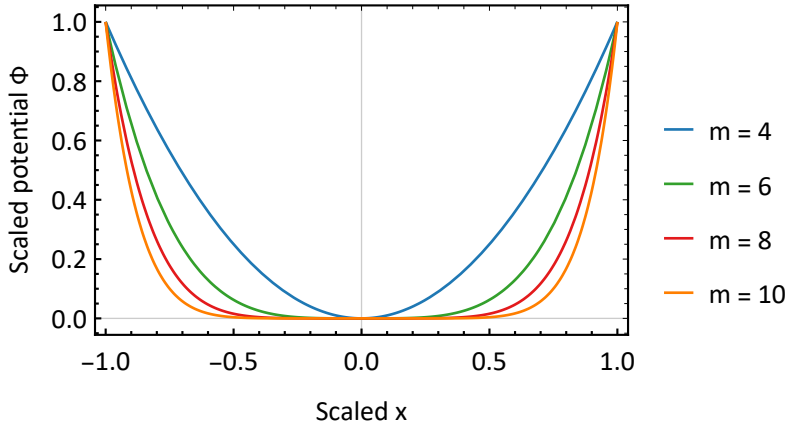


Figure A.2 Pseudo-potential along the  $x$ -direction with  $y = 0$ . The potential gets flatter as the number of the rods increasing.

As shown in Fig. A.2, the potential is flattening when the high order an-harmonic potential dominates. One advantage is that ions would be almost uniformly distributed if we utilize a large number of the rods and then confine a two-dimensional ion-crystal in the  $x$ - $y$  plane. Moreover, the "RF null" line along the center of the multiple rods becomes an "RF null" volume, which is a significant improvement for the purpose of the precision measurement.

## Appendix B System stabilization

System stabilization is one crucial part of a real quantum computing system because quantum systems are fragile to external perturbations. Therefore, we have to suppress all the possible noises well to achieve high-fidelity quantum controls by either passive stabilization or active feedback. In this appendix, we would briefly discuss several feedback loops in our system, which are used to stabilize the repetition rate of the pulsed laser, the trap frequencies, and the power of the laser.

### Repetition rate

In Fig. B.1, we show the schematic diagram of the feedback loop used to stabilize the pulsed laser's repetition rate. Thanks to the dual wavelength outputs of the Mira, we employ the visible laser of 750 nm to measure the repetition rate, while utilize the 375 nm laser for the experiments.

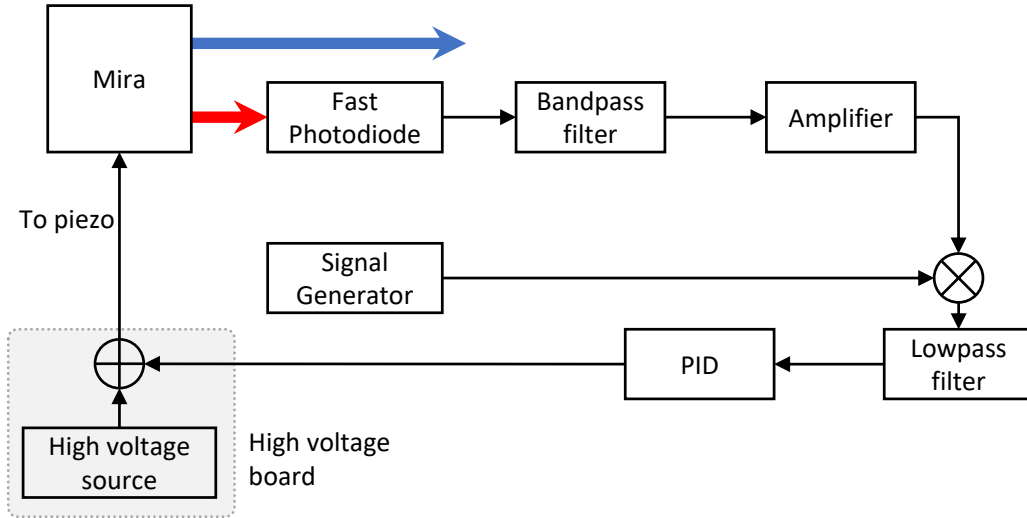


Figure B.1 Active feedback loop for repetition rate stabilization.

To measure the repetition rate, we align the 750 nm laser to a fast photodiode. Here, we simplify the electric field of the pulsed laser as,

$$\vec{E}(t) = \sum_l E_l \vec{e} \exp \left[ i \left( \vec{k}_{750} \cdot \vec{r} - (\omega_{750} + 2\pi l f_{\text{rep}})t + \phi \right) \right], \quad (\text{B-1})$$

where  $\vec{e}$  is the polarization vector and  $f_{\text{rep}} = \omega_{\text{rep}}/(2\pi)$ . We can obtain its intensity signal,

$I(t) = |\vec{E}(t)|^2$ , from the fast photodiode (EOT ET-4000), which can be written as,

$$\begin{aligned}
 I(t) &= |\vec{E}(t)|^2 \\
 &= \sum_{l,l'} E_l E_{l'} e^{i2\pi(l'-l)f_{\text{rep}}t} \\
 &= \sum_l E_l^2 + 2 \sum_{l < l'} E_l E_{l'} \cos [2\pi(l' - l) f_{\text{rep}}t] \\
 &= \sum_l E_l^2 + 2 \sum_l \sum_{n=1} E_l E_{l+n} \cos [2\pi n f_{\text{rep}}t]. \tag{B-2}
 \end{aligned}$$

Note that, the interference part includes all the components in which the frequencies are the integer times of the repetition rate. The signal with a certain frequency is picked up by a tunable bandpass filter. In practice, we choose  $n$  to be 83, corresponding to a frequency of  $n f_{\text{rep}} \approx 6.3$  GHz which is around half of the  $^{171}\text{Yb}^+$  hyperfine splitting. This weak signal, typically around  $-40$  dBm, is amplified by two amplifiers (Mini Circuits ZVA-183-S+ and ZVE-3W-183+), and then mixed (Mini Circuits ZMX-7GR) with a reference signal of  $f_{\text{ref}} = 12.642812118466/2 = 6.321406059233$  GHz (generated by ROHDE&SCHWARZ SMB 100A). The mixed signal pass through a lowpass filter (Mini Circuits SLP-1.9+), and then we obtain the error signal,

$$\text{error} = \sin(2\pi\delta_{\text{rep}}t) \approx 2\pi\delta_{\text{rep}}t, \tag{B-3}$$

where  $\delta_{\text{rep}} = 83f_{\text{rep}} - f_{\text{ref}}$ . This signal is delivered to a conventional servo system (New focus LB1005) and then feed back to the mirror which mounted on a piezo, as shown in Fig. 3.17. The stabilized repetition rate is monitored by a RF counter (Agilent 53210A).

## Trap frequency

The three-dimensional confinements of the trap come from the static harmonic potential (axial direction) and the RF pseudo-potential (transverse directions). The effective trap frequency in the axial direction is pretty stable, while the transverse trap frequencies are fluctuating due to the instability of the RF fields. Therefore, we actively stabilize the amplitude of the RF fields injected to the corresponding electrodes, and the schematic diagram is shown in Fig. B.2. The method described here is based on Ref. [51].

Around 1% of the injected RF field is picked up through a capacitor-circuits shown in Fig. 2.7. After a rectifier, followed by a lowpass filter (Mini Circuits SLP-1.9+), we convert the pick-up RF signal into a DC voltage, which value is proportional to the amplitude of the RF signal. Then this DC signal is compared with a reference level generated from a

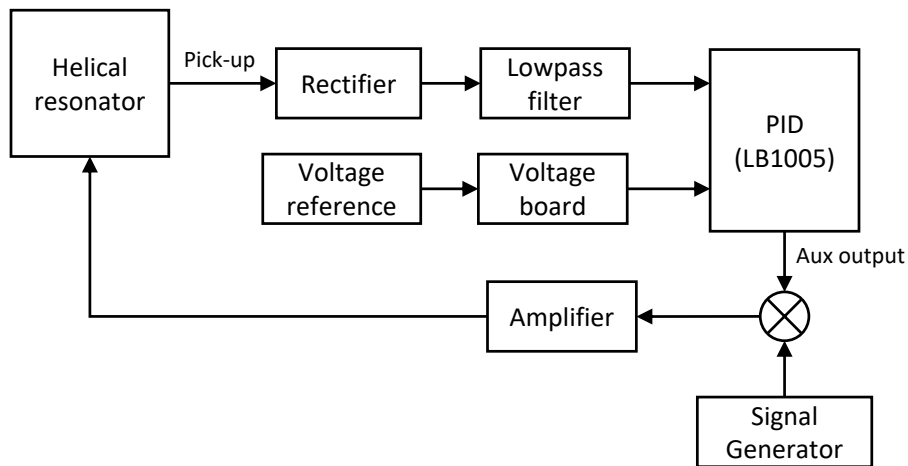


Figure B.2 Active feedback loop for trap frequencies stabilization.

tunable voltage board (DAC8552). Note that this voltage board is referred by a standard voltage reference (Linear Technology LTC6655 5V) to guarantee the stability. To get rid of the DC noise from the servo system (New focus LB1005), we only employ its proportional-integral (PI) filter modular by turning off its input offset and obtaining the output from its aux output port in the back panel. Finally, the output from the servo system is utilized to modulating the amplitude of the RF signal, compensating for the amplitude fluctuations.

### Laser power

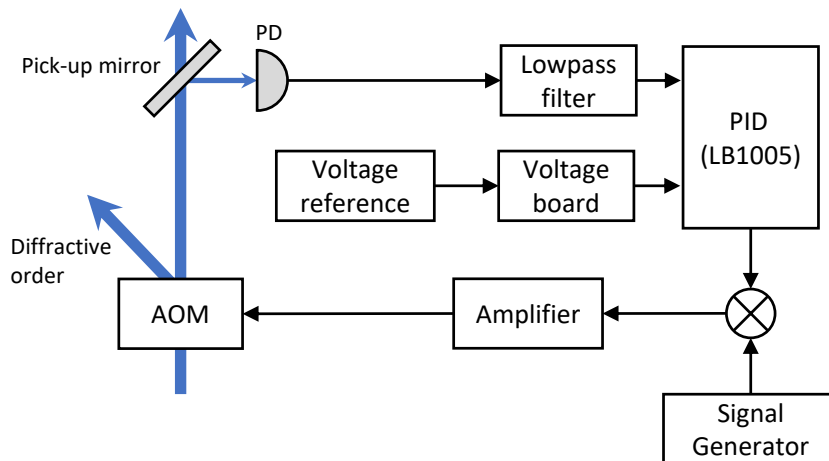


Figure B.3 Active feedback loop for laser power stabilization.

The method of laser power stabilization is similar to that of the trap frequency stabilization, as shown in Fig. B.3. The targeted laser beam first passes an AOM, distributing



a part of power into the diffractive order (either negative or positive one). Then the zero-order goes through a pick-up mirror, where the most of the power ( $> 95\%$ ) transmits, and only a small portion is reflected into a photodiode. Similarly, the signal from the photodiode would be compared with a reference voltage, and then the difference would be processed by the PI filter. The output of the servo system is utilized to modulate the amplitude of the RF signal injected on the AOM. Note that the feedback would fail if the amplitude of the power fluctuation is larger than the power distributed into the diffractive order of the AOM.

## 个人简历、在学期间发表的学术论文与研究成果

### 个人简历

1991年11月22日出生于安徽省淮南市。

2010年9月考入北京大学物理学院，2014年7月本科毕业并获得理学学士学位。

2014年9月免试进入清华大学交叉信息研究院直接攻读理学博士学位至今。

### 发表的学术论文

- [1] **Yao Lu**, Shuaining Zhang, Kuan Zhang, Wentao Chen, Yangchao Shen, Jialiang Zhang, Jing-Ning Zhang and Kihwan Kim. "Global entangling gates on arbitrary ion qubits." *Nature* **572**, 363-367 (2019).
- [2] Andrew Smith, **Yao Lu** (co-author), Shuoming An, Xiang Zhang, Jing-Ning Zhang, Zong-ping Gong, H. T. Quan, Christopher Jarzynski and Kihwan Kim. "Verification of the quantum nonequilibrium work relation in the presence of decoherence". *New Journal of Physics* **20**, 013008 (2018).
- [3] Yangchao Shen, **Yao Lu**, Kuan Zhang, Junhua Zhang, Shuaining Zhang, Joonsuk Huh and Kihwan Kim. "Quantum optical emulation of molecular vibronic spectroscopy using a trapped-ion device." *Chemical Science* **9**, 836-840 (2018).
- [4] Jiyong Park, **Yao Lu**, Jaehak Lee, Yangchao Shen, Kuan Zhang, Shuaining Zhang, Muhammad Suhail Zubairy, Kihwan Kim and Hyunchul Nha. "Revealing nonclassicality beyond Gaussian states via a single marginal distribution." *Proceedings of the National Academy of Sciences of the United States of America* **114**, 891-896 (2017).
- [5] Kuan Zhang, Jayne Thompson, Xiang Zhang, Yaochao Shen, **Yao Lu**, Shuaining Zhang, Jiajun Ma, Vlatko Vedral, Mile Gu and Kihwan Kim. "Modular quantum computation in a trapped ion system." *Nature Communications* **10**, 4692 (2019).
- [6] Mark Um, Junhua Zhang, Dingshun Lv, **Yao Lu**, Shuoming An, Jing-Ning Zhang, Hyunchul Nha, M. S. Kim and Kihwan Kim. "Phonon arithmetic in a trapped ion system." *Nature Communications* **7**, 11410 (2016).
- [7] Shuoming An, Jing-Ning Zhang, Mark Um, Dingshun Lv, **Yao Lu**, Junhua Zhang, Zhang-Qi Yin, H. T. Quan and Kihwan Kim. "Experimental test of quantum Jarzynski equality with a trapped ion." *Nature Physics* **11**, 193-199 (2015).